STUDY AND APPLICATION OF TIME-DELAYED FEEDBACK FOR SEMICONDUCTOR PHOTON SOURCE

A Dissertation
Presented to
The Academic Faculty

By

Chien-Yuan Chang

In Partial Fulfillment
of the Requirements for the Degree
Doctor of Philosophy in the
School of Physics

Georgia Institute of Technology

December 2017

STUDY AND APPLICATION OF TIME-DELAYED FEEDBACK FOR SEMICONDUCTOR PHOTON SOURCE

Approved by:

Prof. David S. Citrin
School of Electrical and Computer Engineering
Georgia Institute of Technology

Prof. Kenneth R. Brown
Department of Chemistry and Biochemistry
Georgia Institute of Technology

Prof. Dragomir Davidovic
School of Physics
Georgia Institute of Technology

Prof. Kurt Wiesenfeld
School of Physics
Georgia Institute of Technology

Prof. Yanne K. Chembo
Georgia Tech-CNRS Joint Laboratory
Centre National de la Recherche Scientifique

Date Approved: November 13, 2017

God runs electromagnetic by wave theory on Monday, Wednesday, and Friday, and the Devil runs them by quantum theory on Tuesday, Thursday, and Saturday.

Sir William Bragg

To family, my parents, Chang, Jui-Meng and Chang, Pei-Chen; my wife, Chou, Hsin-Yi, and sister, Chang, Briana.

ACKNOWLEDGEMENTS

First, I would like to express my sincere gratitude to my advisor Prof. David Citrin for the continuous support of my Ph. D. study and related research, for his patience, motivation, and immense knowledge. He has shown a open-minded attitude towards our wild ideas. His affinity in technologies and science allows various research topics in our group. He demonstrated a great model for myself before starting my own journey.

Besides my advisor, I would like to thank the rest of my thesis committee: Prof. Brown, Prof. Davidovic, Prof. Wiesenfeld, and Dr. Chembo for their insightful comments and encouragement, but also for the hard question which incented me to widen my research from various perspectives.

My sincere thanks also goes to Prof. Ken Brown's guidance when I work in his research group. He has shown me the interesting field of ion-trapping and quantum computing. I have learned many lesson from Ken, including the virtue of perseverance. I would like to appreciate Prof. Senellart and Prof. Lanco, who provided me an opportunity to collaborate with them on project with single photon emitter structures. I would like to thank Dr. Locquet gave access to the laboratory and research facilities. Without they precious support it would not be possible to conduct this research.

I thank my fellow labmates, D. Choi, M. J. Wishon, in for the stimulating discussions, and for all the fun we have had in the last three years in the Lorraine campus. The experimental work in the photonics group is a collective efforts, including valuable devices and suggestions provided by Prof. Abderrahim Ramdane and Prof. Anthony Martinez at *Centre for Nanosciences and Nanotechnology* in *Centre National de la Recherche Scientifique*.

Last but not the least, I would like to thank my family: my parents, my wife, and to my sister for supporting me spiritually throughout this thesis and my life.

TABLE OF CONTENTS

LIST OF TABLES

LIST OF FIGURES

SUMMARY

Time-delayed feedback introduces various dynamical behaviors when coupled with a solid-state photonic structure. The study of these behaviors is a crucial step towards development of novel applications involving measurement and manipulation of various type of solid-state photonic systems. The purpose of this work is to investigate time-delayed feedback in two different types of solid-state structures, the semiconductor lasers diode and single photon emitter. We report our results on two projects: first, we investigate the effect of time-delayed feedback with a semiconductor laser since such a system represents an excellent test bed for the study of nonlinear delay-coupled systems. Here, the feedback is achieved by reflecting the laser's output back into the laser using an external mirror. Under these circumstances, the dynamical behaviors can be described with the Lang-Kobayashi model (LK model) consisting of equations of motion for the optical field, the optical phase, and the carrier density in the active region of the laser. We performed an experiment simultaneously extracting all three dynamical variables in order to obtain a tomographic picture of the dynamics. Secondly, we proposed to explore the time-delayed feedback of a single photon emitter. The effect of time-delayed feedback on a single photon emitter in few-photon limit is considered. Specifically, we focus on the theoretical study of quantum coherent feedback of a single photon emitter that consisted of single quantum dot embedded in a micropillar cavity. Recent theoretical works by us and others have shown highly nontrivial quantum dynamics induced by the external cavity. In this work, we perform a stability analysis of a quantum system in the one-excitation subspace. We also extend the study to the two-excitation subspace to consider the linearity in the excitation number. The aim is to understand the stabilization effect in a coherent quantum feedback system and the dynamical regimes accessible in suitably designed structures.

CHAPTER 1
INTRODUCTION AND BACKGROUND

1.1 Motivation

With the invention of the semiconductor laser and the advancement of fabrication techniques of various photonic structures, we have gained a powerful ability to control and manipulate the optical properties of solid-state photonic devices. The unique characteristics of photonic devices attract much attention, especially for their application in data transmission, communication systems, and signal processing. In this regard, numerous studies have focused on controlling the optical properties of photonic devices in order to meet the demands of achieving optimal signals for these applications.

A fundamental discipline, control theory, has been developed to describe the controlling of a system automatically and continuously. In a dynamical system, it usually provides an effective method necessary to design and reach the desired state.A dynamical system, such as integrated optical devices can be benefit from implementing control theory, where the parameters are optimized for a designated condition. A dynamical system, classical or quantum, of such can be described in the form of autonomous vector field $f[y(t), \lambda_1, \lambda_2, \ldots]$ that does not depend explicitly on time, where $y(t)$ is the dynamical variable and λs are the parameters. Control systems are often based on the principle of feedback (subjected to a finite delayed time), where the output state the reference state are compared in order to correct the initial input state of the system [1, 2]. In a well-designed circumstances, stabilization can be achieved through implementation of various types of time-delayed feedback control schemes [3, 4, 5]. The general concept of time-delayed feedback control starting with the original work by Pyragas [3]. The feedback control schemes focus on control of chaos and stabilization of unstable periodic orbits of

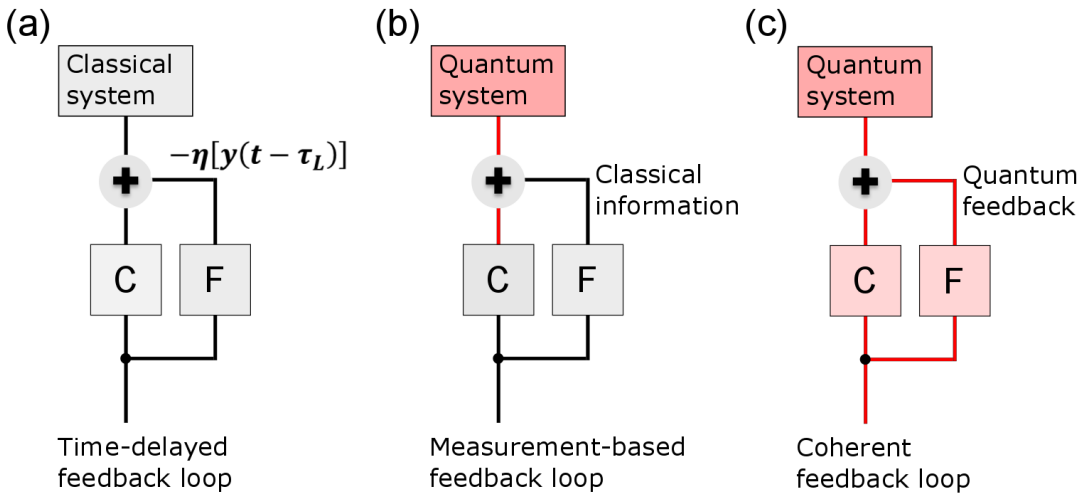

Figure 1.1: Depiction of various feedback loop systems. In (a), the classical feedback loop with a classical system with controller, C, the feedback mechanism, F, with delayed-time, τ; in (b), the output of a quantum system is measured and the classical information is used to affect the quantum evolution; in (c), the output system is coherently manipulated (typically with an unitary operation), and then fed back into the quantum system through coherent coupling.

an oscillator as shown in Fig. 1.1. The time-delayed term arises in the equation of motion of the form $-\eta[y(t-\tau_L)]$ shown in Fig. 1.1 (a), where the feedback strength η, and the delay time τ_L being the control parameters. With the additional feedback term in the Equations of Motions (EOMs), one can drive the system to the desired state. The extension of the Pyragas scheme are the extended time-delayed feedback, where the delay of multiple delayed time can be implemented in the EOMs, which was invented by Socolar et al. [5]. The rthymic control typically achieved through adding a time dependent feedback accounting for a proportionalintegralderivative controller which requires additional circuitry [4].

On the other hand, stabilization effect is not the only outcome for implementing a time-delayed feedback in a nonlinear optical system, it might leads to an unpredictable and chaotic behavior depending on the system conditions. The origin of these complex behaviors come from the nonlinear dependence for the dynamical variables in the optical system. In the classical regime, one example of the nonlinearity emerges from the non-

linear interaction between the electric field and the carriers density in a laser diode. For a one-dimensional time-continuous dynamical system, solutions are monotonic and thus if bounded, they must converge to equilibrium points. In high dimensional autonomous systems, equilibria (fixed points) or limit cycles by the Poincar-Bendixson therorem. In more than 2 D, other things can happen and in particular chaos. So except for bounded 1D continuous time systems, there is no guarantee that equilibria exist [6].

In this study, we specifically focus on the effects of time-delayed feedback which continuously adds self-controlling feedback. In the classical limit, these effects includes both stabilization and destabilization of the dynamical variables. One particular application utilizing both effects are optoelectronic oscillators (OEOs), we demonstrate the performance of the prototype OEOs devices. The second focus of this study focuses on the time-delayed feedback on a single photon emitter. We derive a semiclassical model for single photon emitting devices subjected to a coherent feedback for few-excitations state employing the input-output formalism. This model extends the previous model into few-photon cases and hence increases the complexity by engaging photon-photon interaction and time-delayed feedback. The detailed description for introduction of these topics are discussed in the following sections.

1.2 Optical Feedback in a Semiconductor Laser

With the invention of the semiconductor laser and the advancement of fabrication techniques of various photonic structures, we have gained a powerful ability to control and manipulate the optical properties of solid-state photonic devices. The unique characteristics of photonic devices attract much attention, especially for their application in data transmission, communication systems, and signal processing. Numerous studies have focused on controlling the optical properties of photonic devices in order to meet the demands of achieving optimal signals for these applications. In the case with semiconductor lasers with feedback, the high speed and high dynamical dimensionality has attracted broad interest for

various applications, ranging from radar [7], ultra-fast random bit generation [8, 9], and optoelectronic oscillators [10, 11], to name a few. Moreover, the intrinsic nonlinear dynamics of ECSLs have attracted attention to implement a number of information-processing functionalities in the physical layer, including chaotic encrypted data communications [12, 13, 14], compressive sensing [15], and reservoir computing [16, 17].

In the first part, the feedback is achieved by coupling an output laser with an external mirror and controlling the time-delayed optical field back into the active region of the laser diode. For semiconductor lasers, the extreme sensitivity when subjected to time-delayed feedback has been considered a nuisance for a long time [18]. However, in view of the rich dynamical behaviors as well as the technological importance of these devices, the various complex dynamics have been widely investigated [18, 19, 20, 21, 22]. For the realization of the aforementioned studies, an external cavity semiconductor laser (ECSL) is often built to exploit the rich dynamics. From a more general perspective, ECSLs provide time-delayed feedback systems in which a number of key parameters can be controlled, and combining this with their relative ease of implementation on the tabletop or within photonics integrated circuits, these systems serve as excellent test-beds for the bifurcation analysis for high-dimensional nonlinear systems [23, 24]. The dynamics of ECSLs are commonly described by the Lang-Kobayashi (LK) model [25].

The dynamical behaviors of ECSLs are typically analyzed by the Lang-Kobayashi (LK) model [25, 26]. The LK model provides a coupled delay-differential-equation description of the system variables, *viz.* E, n, and ϕ. The complex electric field is related to the phase with $E(t) = E_0(t)\exp[j(\omega_0 t + \phi(t))]$. The implementation of delay time is incorporated in the LK model in the equations of motion of electric field $E(t)$ as well as the phase $\phi(t)$ for an ECSL.

$$\frac{dE(t)}{dt} = \frac{1}{2}(G(N, E_0^2) - \frac{1}{\tau_p})E_0(t) + \frac{\kappa}{\tau_{in}}E_0(t-\tau_L)\cos(\omega_0\tau_L + \Delta(t)), \quad (1)$$

$$\frac{d\phi(t)}{dt} = \frac{\alpha G_N}{2}(N - N_{sol}) - \frac{\kappa}{\tau_{in}}\frac{E(t-\tau_L)}{E(t)}\sin(\omega_0\tau_L + \Delta(t)), \quad (2)$$

$$\frac{dN(t)}{dt} = J - \frac{N(t)}{\tau_s} - G(N, E_0^2)\ |E_0|^2(t). \quad (3)$$

where, $G(N, E_0^2) = G_N(N - N_0)(1 - \epsilon\Gamma E_0^2)$ is the differential gain with G_N being the modal gain coefficient, N_{th} being the carrier density at transparency, ϵ being the nonlinear gain compression coefficient and Γ being the confinement factor. τ_p is the photon lifetime. κ is the effective feedback rate. τ_{in} is the diode cavity round-trip time. $\Delta(t) = \phi(t) - \phi(t - \tau_L)$ is the phase delay during the external cavity round-trip time τ_L. The α is the linewidth enhancement factor. N_{sol} is the threshold carrier density for the solitary laser. Also, τ_s is the carrier lifetime and J is the pumping term. By adjusting various control parameters (feedback strength η, external-cavity length $L = c/(2\tau)$ with τ the feedback time, injection current J), various dynamical regimes can be accessed [27, 28, 29, 30].

With the experimental ECSL setup and the well defined LK model, we can study the stability of the stationary solutions and their stability dependence on the parameters. Bifurcation analysis is very useful in understanding the dynamical systems. The first step in the analysis is to locate the stationary solutions of Eqn. (1) and (2). Numerically, these solutions at given feedback strength are distributed on an elliptical structure on the plane of $\Delta\phi = \phi(t) - \phi(t - \tau_L)$-vs.-$N$ where $\phi(t)$ is the time-dependent phase of the electric field shown in Fig. 1.2. The solutions residing on the upper part of the ellipse belong to destructive interference condition and are often denoted as antimodes and saddle nodes [31]. The solutions on the lower part of ellipse correspond to constructive interference between the emitting the light and feedback light inside the laser cavity; these are considered external cavity modes (ECMs) with their attractors' nature. Two specific equilibrium solutions are worthy of comment: the minimum linewidth mode (MLM) and the maximum gain mode

(MGM). The MGM is the ECM with the lowest frequency (high-gain end of the ellipse), and is typically stable [19]. The MLM is the ECM most proximate in frequency to the solitary laser mode.

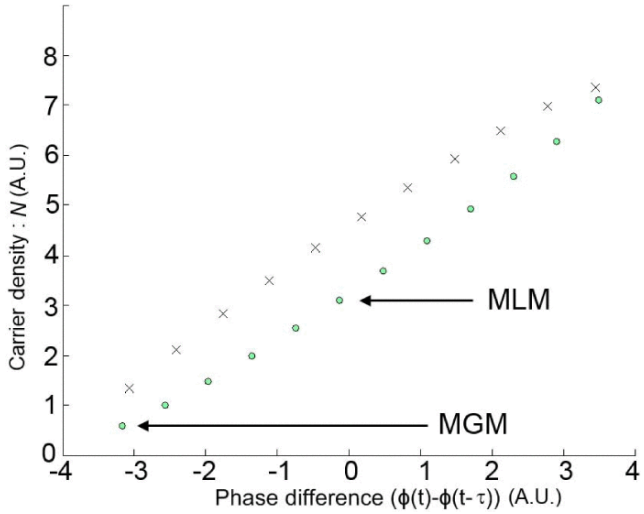

Figure 1.2: Ellipse structure of fixed points in the phase-difference-vs.- N plane for =0.007 and =1 ns. Circles represent ECMs; crosses represent antimodes. [32]

After locating the stationary solutions for the LK model in phase space, we proceed to investigate the stability dependence in the vicinity of ECMs that is determined by the eigenvalues of the Jacobian. If all the eigenvalue is equal to zero, the bifurcation is a steady state bifurcation, but if all eigenvalues is non-zero but purely imaginary, this is a Hopf bifurcation. In many dynamical systems, the bifurcation analysis [33] deal with asymptotic properties of solutions and the trajectories. The quest for analyze a dynamical system deal with the question: will a nearby orbit indefinitely stay close to a given orbit? If this is the case, the orbit is called stable; Or will it converge to the given orbit? In the latter case, it is called asymptotically stable and the given orbit is said to be attracting.

In the general time-dependent case, a trajectory in the space shown in Fig. 1.2 is traced out parametrically in time, indicating the detailed evolution of all dynamical variables of the system. The time-dependent intensity and other variables can be extracted from the phase-space trajectory and used to construct a theoretical bifurcation diagram (BD)

which in turn can be compared with the experimental BD. Thus the connection between dynamical regime as manifested in the BD and the detailed dynamics can be made. A BD can be drawn by changing one of the parameters, λs. A complete understanding of BD is of fundamental importance on analyzing ECM stability which results in distinct dynamical behaviors. Here, we particularly focus our discussion on the feedback strength, η. Among the parameters given in the LK model, the feedback strength provides fine adjustment and direct control for drawing a BD as a function of feedback strength. Various investigations focus on the essential role of feedback strength to plot theoretical BDs [31, 34]. Despite years of interest, the experimental BDs with continuously tuned parameters for the optical intensity have only been obtained recently [35, 36, 37, 27] largely confirming prediction of the LK model. Thus far, the experimental studies have only focused on the optical intensity, i.e., the electric field strength except for a recent publication [38]. The carrier information $N(t)$ is expected to exhibit a similar complexity due to their coexistence in phase space with similar dimensionalities.

The LK model allows one to explore dynamical trends as various parameters are tuned; most studies focus on η [36, 39, 40, 41] and visualize these trends by means of bifurcation diagrams (BD). Recently, we demonstrated experimental BDs for the optical intensity $I(t)$ as η is varied [32, 42, 27]. Both theoretical and experimental BDs provide global perspectives on the evolution of the dynamical regimes as the chosen parameter is varied; in particular, one can test predictions of the sequence of bifurcations based on the LK model. Most studies to date, however, only focus on $I(t) \propto E^2(t)$. To more thoroughly map the dynamics in phase space, it is necessary to probe additional dynamical degrees of freedom. Changes in $n(t)$ in the gain region can be obtained from the LD terminal voltage $V(t)$ at fixed J [43, 44, 45]. We recently reported such measurement, while varying the control parameter η, in Refs. [10, 11]. This allowed us to plot BDs based on $V(t)$. These investigations provide another component of a global perspective of the route to chaos in ECSLs. In Ref. [11], a largest-Lyapunov-exponent analysis was applied to both $I(t)$ and

$V(t)$, this confirms the theoretical prediction of comparable dynamical complexity to that provided by $I(t)$ and verifies that the additional information from voltage measurement, $V(t)$. In order to interpret the information contained in this additional degree of freedom, it is essential to focus on its dynamics compared to the better-known dynamics in $I(t)$. While their relationship has been studied theoretically [46, 23, 19, 38] in various dynamical regimes, to date experimental verification, outside of LFF, is absent.

The complex dynamics experienced by a nonlinear system for given initial conditions correspond to a trajectory in phase space that spans all the system's dynamical variables. Visualizing the phase-space dynamics both provides a heuristic tool as well as opens a quantitative window onto the dynamics that may otherwise be difficult to apprehend. One can verify the complexity of both dynamical variables, $I(t)$ and $V(t)$. This projection is spanned by the optical intensity$I \propto |E|^2$ (with E the slowly-varying amplitude of the optical field), the optical phase ϕ, and the inversion n in the gain medium.

One such theory is predicted based on delay-embedding theory, which provides a reconstructed attractor [47, 48, 49]. The validity, however, of a specific delay embedding in various dynamical regimes is not obvious and must be checked. Based on delay-embedding theory, that the phase portrait in $|E|$ and n migh be reconstructed by plotting $|E(t)|$ versus $|E(t-\tau)|$ parametrically in time. Refs. [48] and [47] investigate the requirements for accessing this information by reconstructing from the signal and delayed signal in other deterministic time-delayed systems. Theoretically, the reconstructed phase portraits and the experimental phase portraits may share some (invariant) properties; however, they are limited to the vicinity of an attractor along with other mathematical conditions discussed in Ref. [49]. Note, however, it is not a foregone conclusion that such reconstructed phase portraits are necessarily correct, even proximate to an attractor. Clearly, the ability to obtain *experimental* phase portraits takes precedence over any reconstructed phase portraits. Our work opens the way for such a detailed comparison, though the aim of the present work is to introduce the technique rather than to provide such a comparison.

ECSLs are also recognized as being simple and inexpensive sources of high dimensional chaos [50], and are of interest for applications such as chaos radar [51] and ultrahigh rate random-bit generation [8, 52, 9]. But to realize the full potential of such applications, a detailed knowledge of the complex dynamics of ECSLs is required [46], and despite 50 years of study, there are basic issues that remain to be elucidated. In Ref. [38], phase plots of the optical intensity, phase, and laser voltage were obtained but only for the complex chaotic regime of low-frequency fluctuations. We also focus on phase portraits revealing accross various dynamical regimes, *i.e.,* from the first instabilities that lead the ECSL into a chaotic regime.

Many dynamical behaviors of the laser with time-delayed feedback have been explored since then and a number of potential applications have been investigated. These range from secured optical communication [53, 12, 14], optoelectronic oscillators (OEOs) [54, 55, 56, 57, 10], high-speed random number generator [18, 8], to reservoir computing [58]. With the ability to extract carrier information directly, many applications of ECSL can be simplified by obtaining the electrical voltage signals $V(t)$ from the laser diode injection terminals under constant-current injection and eliminate the need for optics to electric conversion. Particularly, the OEOs generate high-quality-factor (Q) microwave waveforms by taking advantage of the broad bandwidth and low attenuation of the optical system. The preceding transition from optical extraction to electrical extraction is demonstrated with a periodic OEO and chaotic OEO in the X-band frequency range in our recent publication [10].

The time-delayed feedback effect on a semiconductor laser will be shown with our recent experimental setup of a distributed feedback (DFB) laser for an external cavity semiconductor laser (ECSL) in section 2.1. Two theories, namely, the delay-embedding and the Pyragas feedback, are discussed with the experiemental result in section 2.2. The dynamics of the electric field and carrier in the LK model are compared with experimental parameters, the intensity and voltage of the laser diode in section 2.3; a fundamental application

exploiting the carrier information of an ECSL are the generation of periodic and chaotic waveforms in the microwave range for an optoelectronic oscillator [10] in section 2.4.

1.3 Quantum Coherent Feedback for a single photon emitter

The success of the theoretical model and the experimental confirmation lead to the development of integrated photonic circuit technologies that focus on fabrication and integration of the solid-state device [59]. Recently, with the advancement of manufacturing techniques in solid-state devices such as microcavities and nanolasers, researchers are readily moving to the new field of quantum network, quantum information engaging data processing with few-photon solid-state devices. In a such scenario, a feedback control scheme focusing on stabilizing the quantum system is also desirable for these applications. However, single/few photon emitter such as the quantum dot-microcavity system with feedback exhibits a different behavior from the classical LK model despite the similarity in the setup. In the quantum limit, the conventional LK model breaks down in the few photon quantum limit describing the nonlinearity aspect on quantum optics.

With the recent advance in the fabrication nanophotonic structures, we have gained the ability to control and manipulate the optical properties on the single-photon level [60, 61, 62]. One of the techniques central to such control is the ability to access the strong-coupling regime of cavity quantum electrodynamics (cQED). In solid-state structures, recent developments included coupling quantum emitters such as quantum dots (QDs), to photonic crystals [63, 64, 65] and micropillar cavities [66, 67]. These devices provide unidirectional photons that are of interest, for example, to improve quantum communications over long distances [68]. In addition, the ability to control and coherently manipulate photons coupled to the internal state of the QD is of great importance due to potential applications in quantum memory and quantum information processing [69].

Controlling a quantum system presents a non-trivial problem [70, 71]. Two feedback control schemes have been widely used in quantum optics, *viz.* the measurement-

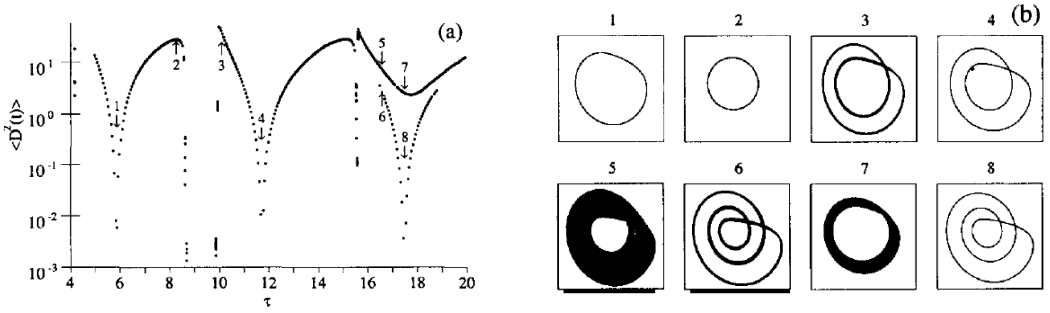

Figure 1.3: (a) Dependence of the dispersion of perturbation on delay time and (b) the x-y phase portraits of the Rossler system in the post-transient regime for some values of the delay time. $K = 0.2$. [3]

based feedback and coherent feedback loops [72, 73], shown in Fig. 1.4 (a) and (b). The measurement-based feedback loop monitors the quantum system, and the outcome of the measurement is used as classical information to manipulate the operations in Fig. 1.4 (a). A measurement-based feedback loop has been implement with cavity QED system with trapped atoms [74]. However, given that measurement process will unavoidably collapse the wavefunction, a measurement-based feedback is not ideal for target state being superposition. On the other hand, in coherent quantum feedback loops, the system interacts coherently with an ancillary subsystem in both the extraction and manipulation processes. For coherent feedback such as Pyragas type feedback, both processes utilize information stored in the reservoir from the external cavity (EC) shown in Fig. 1.4 (b).

For coherent feedback such as Pyragas type feedback, both processes utilize information stored in the reservoir from the external cavity shown in Fig. 1.4 (c). The effects of Pyragas-type feedback is shown in Fig. 1.3, the dependence of the dispersion of the distributed orbits on the delay time, τ is plotted compare to the intrinsic orbit periodicity. The advantages for Pyragas control are the following: the feasibility of applying very fast autonomous feedback control, noninvasive feedback when the delay time approaches the period of the oscillator [3, 75, 76], preserving the coherent state without any measurement of the feedback signal that results in collapsing the state [77], and wide applicability that does not require prior analytical knowledge of the dynamics. Quantum coherent feedback

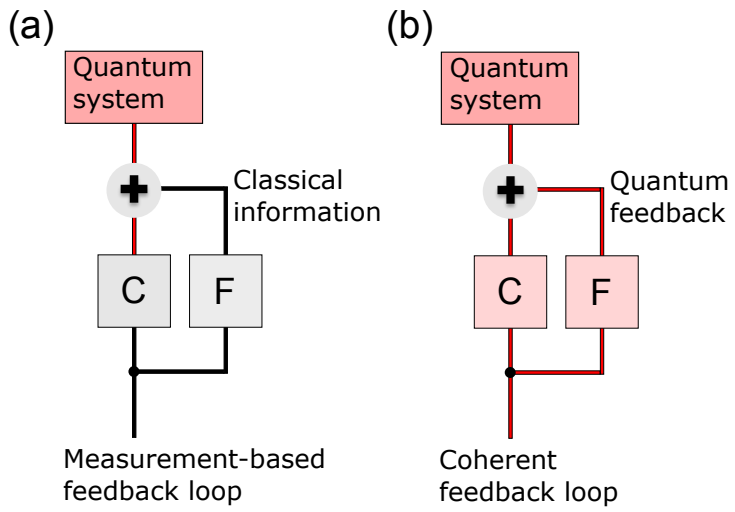

Figure 1.4: Depiction of various feedback loop systems. In (a), the output of a quantum system is measured and the classical information is used to affect the quantum evolution; in (b), the output system is coherently manipulated (typically with an unitary operation), and then fed back into the quantum system through coherent coupling.

has been widely discussed in quantum optics [78, 74] and experimental implementation through coupled waveguides [79, 80, 81] with different types of qubit setup. The addition of delayed-feedback is shown to generate excessive number of solutions, whereas these solutions often display an oscillatory stability [82, 83]. The existence of the excessive solutions is often seen in many nonlinear systems, but not in quantum system due to the linear nature of quantum mechanics. [84]

Turning to quantum systems with coherent feedback, one might expect nonlinear behavior in the number of photons. The nonlinearity involving of states with a small number of photons has been observed experimentally [85, 86]. These effects cannot be described with a classical electromagnetic field, *i.e.*, the scaling of the behavior with photon number cannot be accounted for by the corresponding optical intensity. Hence, a fully quantum mechanical treatment of such time-delayed systems, including the electromagnetic field, is essential to understand the dynamics of single-photon emitters with coherent time-delayed feedback. Recent theoretical studies have focused on quantum coherent feedback in various systems, such as ensembles of atoms [87, 88, 89], a single atom in a cavity [90], one-

dimension waveguides [91, 92], and photonic crystals [93, 94, 95]. These works provide a promising route to rapid convergence of states [96], enhancing entangled photon-pair generation from biexcitons [97], and to drive continuous exchanges for pure states [93]. Among these studies, stability in coherent feedback systems has only been investigated by Grimsmo [90] based on linear delayed differential equations. There has been recent interest in stationary states in chiral quantum optics with atomic mirror [98] and V-level atoms [99]. The evolution of the quantum states in these investigations is described by means of a time-varying Hamiltonian. These works are focused on specific features of the quantum system and not on the stability of the target state, which from the standpoint of experimental realization or practical application is of key importance.

To implement coherent quantum feedback in quantum optics, one typical setup is a half cavity with a mirror, similar to time-delayed feedback setup used in external cavity semiconductor laser (ECSL) system. The dynamics of an ECSL have been intensively by the Lang-Kobayashi (LK) model [25]. The nonlinear behavior of states involving a small number of photons has been observed experimentally [85, 86]. Hence, a fully quantum mechanical treatment of such time-delayed systems, as opposed to the classical LK model, is essential to understand the dynamics of single-photon emitters with time-delayed feedback. Recent theoretical studies have focused on the quantum coherent feedback in many quantum systems, such as ensembles of atoms [87, 88, 89], a single atom in a cavity [90], one-dimension waveguides [91, 92], and photonic crystals [93, 94, 95]. These works provide a promising route to rapid convergence of states [96], enhancing entangled photon pair from biexciton state [97], and drive continuous exchanges for pure states [93].

In view of the relative lack of understanding of how coherent feedback can provide stability in quantum systems, in this letter, we consider a quantum system composed of a single-photon emitter in the form of a QD within a microcavity (MC) formed by a micropillar with coherent quantum feedback provided by a distant mirror. The quantum feedback, therefore, is achieved via the EC, similar to previous studies [93, 94].

In this study, We derive a sets of EOMs for the quantum amplitudes associated with the natural basis describing the QD excitation, the MC photon, and the EC modes. We focus on the one- and two-excitation subspaces. For the one-excitation state, we find the stationary-state solutions. Next, we address the stability of these states. In the vicinity of the stationary state, we derive the Jacobian of the state amplitudes. We then perform a stability analysis by analyzing the eigenvalues of the Jacobian matrix as a function of coupling strength and the damping rate. We determined the stability by the dynamical analysis by numerically perturbing the stationary state which agrees with the results obtained directly from the Jacobian of the state amplitudes. The effects of time delay are also studied for various. Subsequently, we find a stationary two-excitation state.

The coherent quantum feedback configuration offers several possible interesting experiments involving photon statistics and entanglement. The optical instability of single photon emitter with coherent quantum feedback will be investigated with bifurcation analysis and our simulation model. Our future work will specifically focus on theoretical study of the nonlinearity effects, such as optical bistability and quantum chaos in few photon regime. With this theoretical study, future studies of quantum phenomena or nonlinear dynamics in optical bistability are made possible.

The coherent quantum feedback effect on a single photon emitter is shown in chapter 3. The setup for a single photon emitter with semi-classical description model is discussed in section 3.1, the simulation results and the application of coherent feedback and potential control scheme are shown in section 3.2. We perform the stability analysis for a single excitation in section 3.3 and the optical nonlinearity feature for different photon number is demonstrated in section 3.4.

CHAPTER 2

EXTERNAL CAVITY SEMICONDUCTOR LASER (ECSL)

In this chapter, I will discuss the realization of time-delayed feedback in two types of solid-state devices, semiconductor laser and single photon emitter. In Section. 2.1, an external cavity semiconductor laser (ECSL) system is built to provide time-delayed optical feedback with an external mirror. We discuss the verification of two theoretical models, the reconstruct of attractors by delay-embedding and orbit stabilization by Pyragas type feedback in Section 2.2. A detailed discussion of the parameters, intensity and carrier number are extracted simultaneously. The nonlinear dynamics of both bifurcation diagrams and the phase portraits in their projected parameter space is provided in Section. 2.3. A fundamental application for the carrier information from an ECSL is demonstrated with a multi-purpose optoelectronic oscillator (OEO). With the direct extraction of the $V(t)$ signal, we demonstrate a multi-GHz OEO generating periodic oscillation as well as high dimensional chaos [10]. The detailed characterization of our OEO is shown in Section. 2.4.

2.1 Experimental Setup

A schematic of our ECSL setup is shown in Fig. 2.11. For our experiments, we employ a single longitudinal-mode edge-emitting InGaAsP distributed feedback (DFB) LD containing seven quantum wells in the active region [10]. The grating is designed and fabricated to achieve a k product of 50 cm^{-1} and the length l of the LD cavity is 600 μm, achieving a kl value of 3. The LD is that of Ref. [100]. The LD emits at 1550 nm with a free-running threshold current $J_{th} = 29.8$ mA. We simultaneously measure $I(t)$ and $V(t)$ where we synchronize the two via cross-correlation of two signals as the optical path length is varied; the signals are synchronized to within 1 ps, which is much shorter than any relevant dynamical timescale.

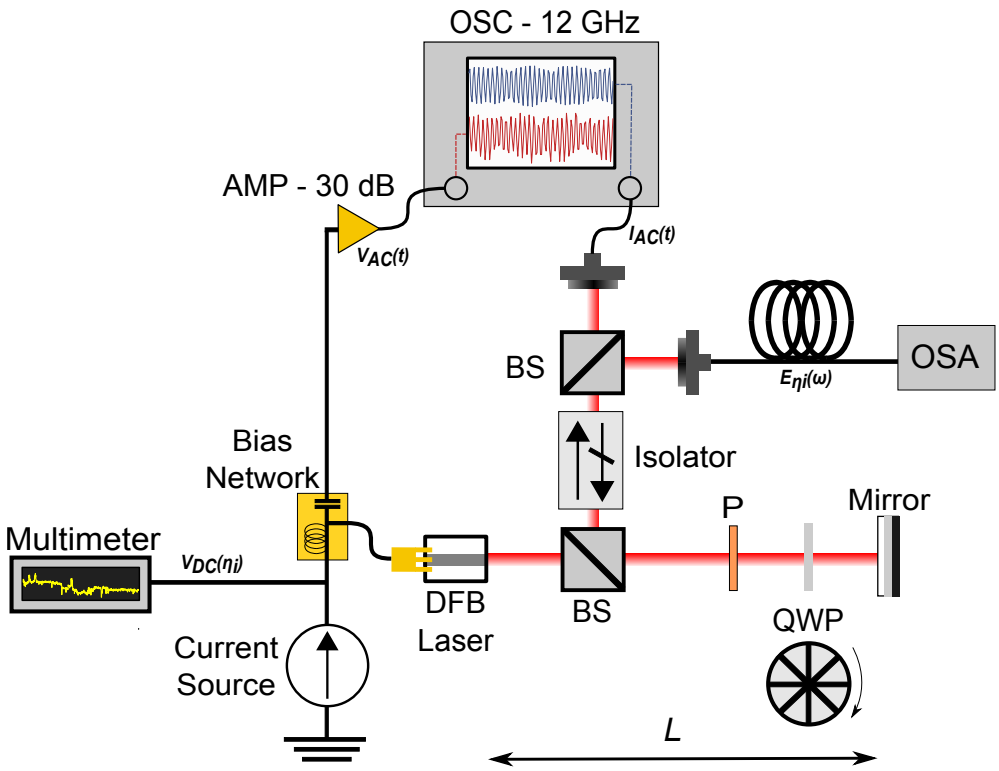

Figure 2.1: Experimental setup. OSC: oscilloscope, AMP: radio-frequency (RF) amplifier, OSA: optical spectrum analyzer, BS: beam splitter, P: polarizer, QWP: quarter-wave plate.

During the experiment, the OSA continuously measures the optical spectrum for each η. $V(t)$ is measured across the LD injection terminals utilizing a radio-frequency (RF) probe with 40-GHz bandwidth. The DC and AC components of $V(t) = V_{DC} + V_{AC}(t)$ are separated with a bias tee. The AC component, $V_{AC}(t)$, is amplified (AMP) with an 30-dB amplifier with 30 GHz bandwidth in real-time. In addition, the AC components $I_{AC}(t)$ [of $I(t) = I_{DC} + I_{AC}(t)$] and $V_{AC}(t)$ are simultaneously recorded on a real-time oscilloscope (OSC) with 12 GHz cut-off frequency. The AC signals are small compared with the DC signals leading to the approximate proportionality of these signals to the dynamical relevant degrees of freedom $E(t)$ and $n(t)$ [43].

To tune η, the relative angle between the polarizer (P) and quarter-wave plate (QWP) in Fig. 1 is adjusted in 0.05° increments ($\eta = 1$ corresponds to $\sim$15 % of the optical power coupled back onto the collimating lens). This is done by reducing the overlap of the optical

mode of the feedback field into the active region of the LD in order to extract a clear BD.

The synchronization of two extracted signals is obtained by measuring the time differences in each measurement path, *i.e.*, the distance in free space and the electrical delay in the circuits. This results is compared to the autocorrelation function of two signal to extract the absolute delay ~ 6.775 nanosecond. Additionally, we considered the optimal condition two signals are fully synchronized when the intensity signal leads the voltage signal by $\pi/2$ [101] without feedback.

2.2 Delay-Embedding and Pyragas Feedback

We investigated the phase portraits by directly extracting two parameters, voltage vs. intensity, of an ECSL and compared them with theoretical prediction of reconstructed phase portraits based on optical intensity vs. delayed intensity. This comparison of experimental phase portraits and reconstructed phase portraits reveals good qualitative agreement, thus validating the dynamics extracted from the voltage measurements. Indeed, a delayed phase space may share some invariant properties with the actual one (e.g. dimension of attractor, Lyapunov exponents); however, we have no *a priori* reason to expect the details should be identical. Moreover, as our results rely on two degrees of freedom, they show promise to more thoroughly test the LK model than can be provided by a single dynamical variable [46, 102]. In the work presented here, we observe a QP route to chaos interrupted by two types of LCs, *viz.* a SH regime and a coexisting PD before entering the edge of CC.

The theoretical phase portraits can be reconstructed using a fundamental theory, namely, delay-embedding [49, 47, 48]. In the theoretical model, a phase portrait can be plotted using the signal, in the case of ECSL, the intensity, and the delayed signal. The phase portraits near a reconstructed attractor that shares some (invariant) properties with the real attractor. However, the validity of the embedding approach is not obvious across the various parameter ranges applying to our very real ECSL

The reconstructed phase portrait is only (possibly) valid near an attractor (i.e., the on-

set of chaos and within a chaotic regime [47]). Moreover, the embedding theorems are only valid under mathematical conditions that may be arduous to verify in a specific experimental system, On the other hand, these theorems are valid for purely deterministic systems while a real ECSL is inevitably subject to noise (intrinsic in the form of spontaneous-emission noise as well as extrinsic noise) that contributes directly to its dynamics Lastly, the embedding theorems require that the number of additional delayed variables should be larger than the number of "real" system variables; thus a single delayed variable (the delayed electric-field strength or intensity) is not guaranteed to convey the same info as an additional independent variable.

Thus, by providing both reconstructed and directly measured phase portraits, we show the qualitative differences in the trajectories near the reconstructed and the real attractors. The reconstructed phase portraits in this paper are based on the optical intensity and delayed intensity. We observe that some of the characteristics of these trajectories depend on the dynamical regimes of the ECSL.

Thus, it is unclear if such conditions obtain to an extent to which embedding provides an adequate description for our system with any system parameters. In the previous section, we have shown such experimental phase portraits can be obtained over a large range of parameters (here feedback strength η, though we have also results not presented here for various values of external-cavity feedback time τ and injection current J. Obtaining the experimental phase portraits over a range of feedback strengths, and corresponding dynamical regimes, is in our view interesting in its own right.

On the other hand, Pyragas *et. al.,* has investigate the stabilization effects of unstable periodic orbits of a chaotic system. It can be achieved either by combined feedback with the use of a specially designed external oscillator, or by delayed self-controlling feedback without using of any external force. In section 2.4, we have demonstrated an order of magnitude reduction in phase jitter for both stabilization techniques by applying the Pyragas-type feedback in an optical system. The modulation leads to an increase in coherence, and

therefore a reduction in jitter is observed. As we have discussed in the previous chapter, this methods do not require an a priori analytical knowledge of the system dynamics and are applicable to experiment. The delayed feedback control does not require any computer analyses of the system and can be particularly convenient for an experimental application.

2.3 Bifurcation Diagram and Projected Phase Portrait

In this section, we present *simultaneous measurements of the time series (TS)* $I(t)$ *and* $V(t)$ *on the route to chaos, from continuous-wave (CW) to coherence collapse (CC)*. The TSs, when plotted parametrically in time t in the I-V plane (V serving as a surrogate for n) provide a *phase portrait* of the dynamics, *i.e.*, the resulting plot is a projection in the ϕ direction of the phase-space trajectory onto the I-V plane, where ϕ is the phase difference between the input and output electric fields. While numerous *theoretical* studies of phase portraits in ECSLs based on the LK model have been presented in the literature, *e.g.*, [102, 46], to our knowledge, the *experimental* phase portraits presented here are the first publishedmapping out the route to chaos in an ECSL. Together with the global view provided by the BDs [10, 36, 32, 42, 9], the phase portraits provide unprecedented detailed insight into the phase-space dynamics in various regimes and open the way to more thorough testing of theoretical predictions.

Before embarking on our more detailed discussion, it is helpful to orient ourselves by means of simple examples. To start, consider an ECSL under CW operation, for which $I(t)$ and $V(t)$ are constant. In this case, a parametric plot of $I(t)$ and $V(t)$ in t will be a point in the I-V plane. Now consider relaxation oscillations (RO), a small-signals model accounting for the dynamics of $I(t)$ and $n(t)$ given a small temporal perturbation shows that $I(t)$ and $n(t)$ both exhibit damped sinusoidal oscillations near the LD RO frequency f_{RO} with $n(t)$ lagging $I(t)$ by $\pi/2$ [101]. In an ECSL, for certain ranges of η, these ROs may become undamped and shifted in frequency [103, 104, 105, 106, 107, 108]. Consequently, a parametric plot of $I(t)$ and $V(t)$ in t, again the corresponding phase portrait, will be

Table 2.1: Dynamical regimes and the ranges of η shown in Fig. 2.2(b).

Dynamical regime	η Range
Continuous-wave (CW)	$[0, 0.07]$
Quasi-periodic (QP)	$(0.07, 0.29]$
Limit-cycle (LC)	$(0.29, 0.4]$
Subharmonic (SH)	$(0.4, 0.52]$
Period-doubled (PD)	$(0.52, 0.64]$
Coherence-collapse (CC)	$(0.64, 0.9]$

an ellipse with semi-major axis with negative slope in the I-V plane. Of course, in other dynamical regimes, the phase portrait will reflect the more complex combined dynamics of $I(t)$ and $V(t)$, as we see below.

As we increase η, $E(t)$ and $E(t-\tau)$ interact within the nonlinear active region of the LD, giving rise to the various types of dynamics discussed below. These dynamics are manifested in both $n(t)$ [measured through $V(t)$] and $E(t)$ [measured through $I(t)$]. The TSs at the various values of η can be used to plot the BDs shown in this section. We start with a global picture of the route to chaos presented in terms of BDs for $I(t)$ and $V(t)$ as η is increased. In the subsections below, we consider phase portraits within various dynamical regimes along the route to chaos.

Figure 2.2 shows the BD obtained from (a) $V(t)$ and (b) $I(t)$ as a function of η. Each BD is obtained by plotting the density of local extrema of the corresponding TS as a function of η. The density is high in white, intermediate in shades of orange, but low in black. The value reflects the turning point of the trajectories (maxima and minima in both V and I), and thus for a given η, regions showing small ranges of pronounced high- and low-density contrast tend to represent dynamical regimes exhibiting repetitive (more stable) trajectories. The region for $\eta > 0.64$ in Fig. 2.2(b), however, does not correspond to a small number of maximum/minimum values of $I(t)$, but to chaotic behavior. [Note that the BD for $V(t)$ in Fig. 2.2(a) shows less clear features due to additional noise and filtering in the voltage measurement; nonetheless, as noted above we have confirmed that

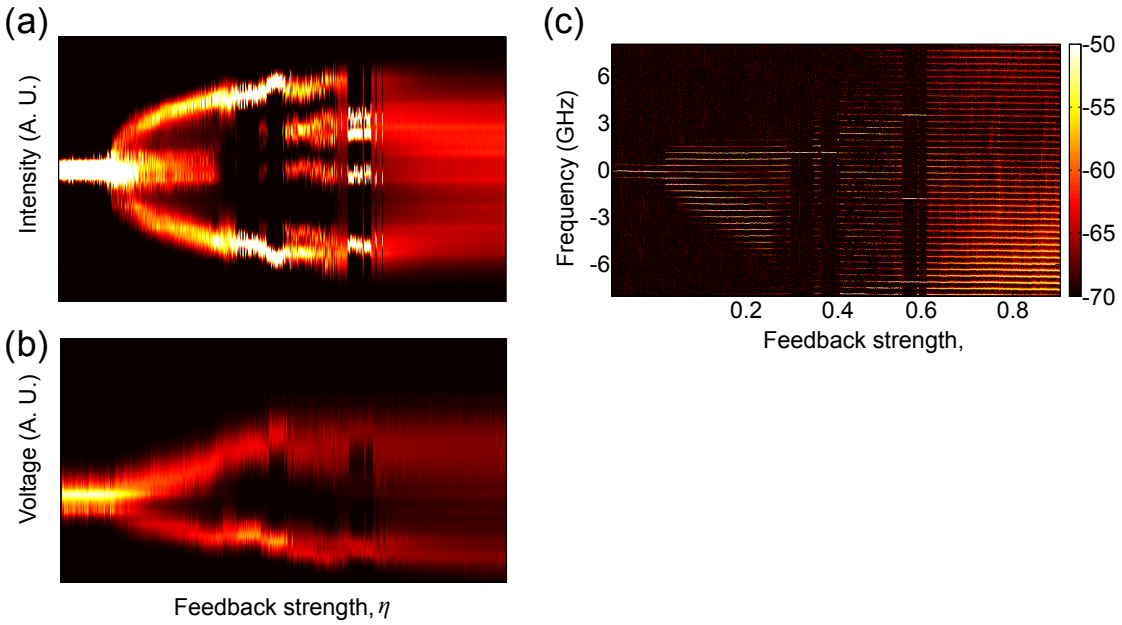

Figure 2.2: BDs illustrating the various dynamical regimes as η is varied: (a) for $V(t)$ and (b) for $I(t)$. In (b), various dynamical regimes, listed in Table I, are labelled. (c) The optical spectrum is taken simultaneously showing the active ECMs as η is varied; the zero of the frequency scale corresponds to the LD free-running frequency ($\eta = 0$) for the value of J used. All data are taken for $J = 90$ mA and $L = 42$ cm. Color scales provide relative values of the density but are in arbitrary units.

$V(t)$ contains dynamical complexity comparable to that of $I(t)$ indicating that any filtering of $V(t)$ retains information on crucial information-theroretic timescales.] In Fig. 2.2(b) the dynamical regime is labelled with the abbreviation of each regime [42]; see Table I for the ranges of η and their correspondence to dynamical regime.

The system evolution can be interpreted as trajectories in phase space in the vicinity of external-cavity modes (ECMs) that are the stable steady-state solutions of the LK equations; the unstable solutions are known as antimodes [25]. Each ECM is associated with a different standing-wave solution in the external cavity, and thus the various ECMs are separated in frequency approximately by the external-cavity free-spectral range $f_\tau = \tau^{-1} = c/(2L) = 0.36$ GHz for $L = 42$ cm. We can track the ECMs that participate in the dynamics for a given η from the optical spectrum as in Fig. 2.2(c). The bright features in Fig. 2.2(c) at each η show the active ECMs. For example, we can identify the dominant

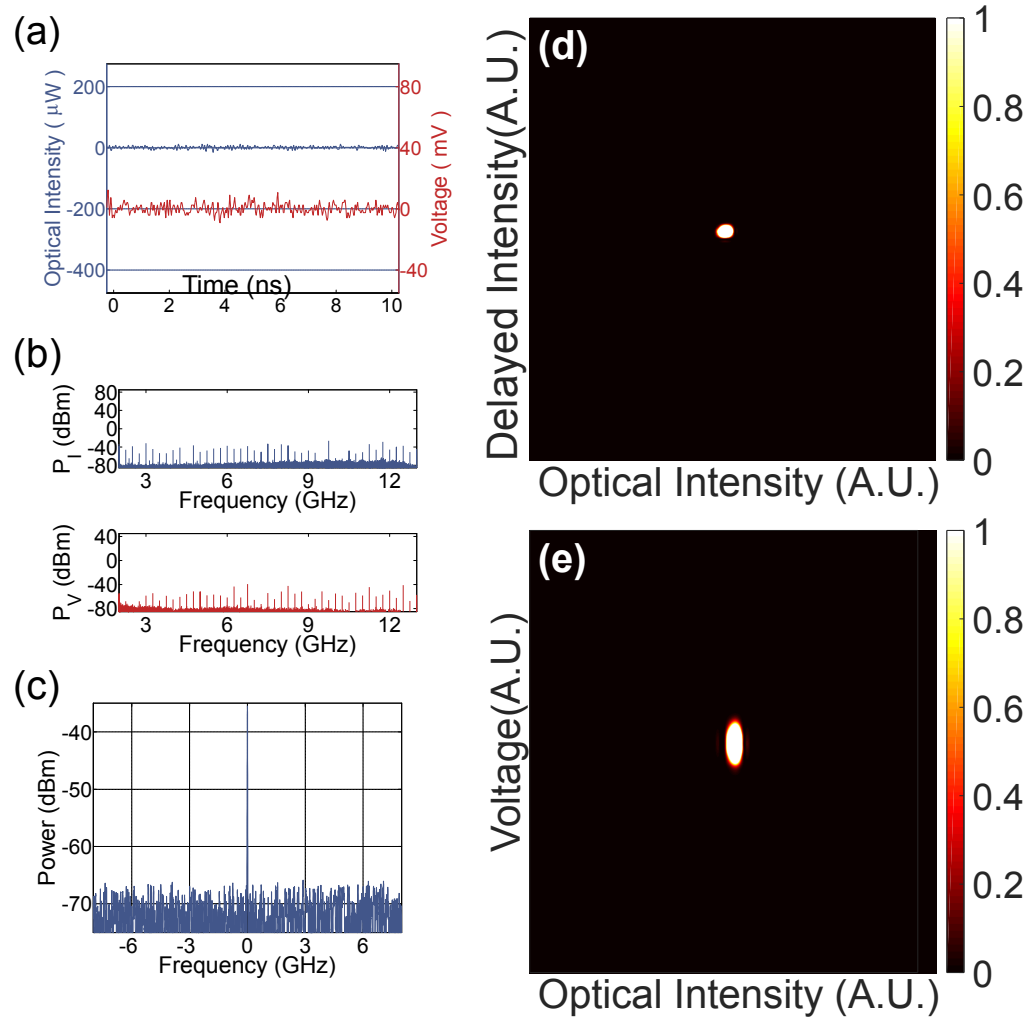

Figure 2.3: The dynamics in the CW regime with $\eta = 0$. (a) $I_{AC}(t)$ and $V_{AC}(t)$ and (b) corresponding RF spectra. (c) The optical spectrum and phase portrait based on (d) intensity vs. delayed intensity (e) and intensity vs. voltage.

ECM in the periodic regime ($0.29 \leq \eta \leq 0.4$); it is the third ECM (*i.e.*, ECM 3) above the minimum-linewidth mode (MLM), labeled ECM 0, as shown in Fig. 2.2(c). The optical spectrum in this regime shows, in addition, many active ECMs $\lesssim 3$. In the subsections below, we explore the phase portraits as η increases taking the ECSL from CW to CC.

Continuous-wave and quasi-periodic

We begin with no feedback $\eta = 0$ with the ECSL operating in CW. CW behavior persists as η is increased up to 0.07 as can be seen in Fig. 2.2(b). (See also Table I.) Figure 2.3(a)

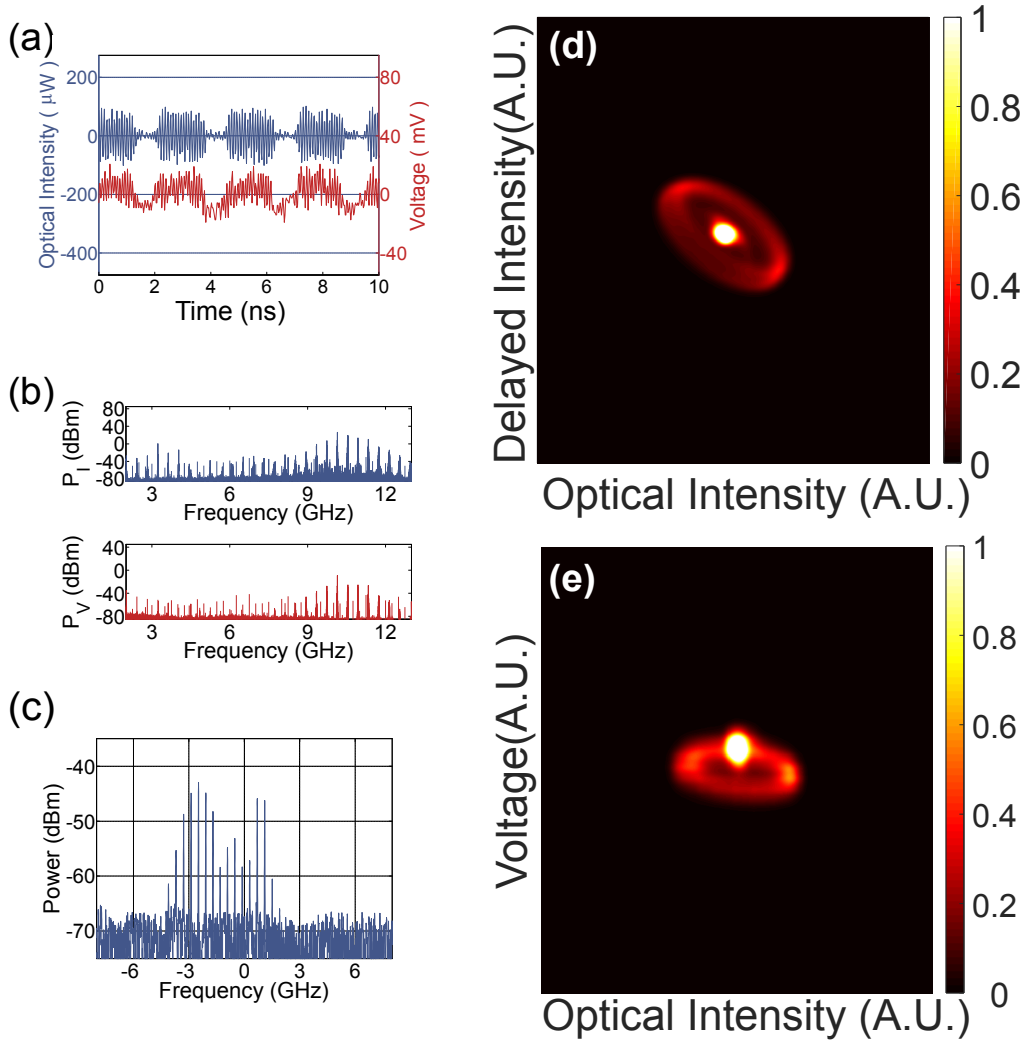

Figure 2.4: The dynamics in the QP regime with $\eta = 0$. (a) $I_{AC}(t)$ and $V_{AC}(t)$ and (b) corresponding RF spectra. (c) The optical spectrum and phase portrait based on (d) intensity vs. delayed intensity (e) and intensity vs. voltage.

shows both $I(t)$ and $V(t)$ for $\eta = 0$; $V(t)$ and $I(t)$ are constant with superimposed noise. The phase portraits, in Fig. 2.3(d) and (e), consequently, are a dot that is broadened by noise. Under these conditions, the ECSL operates purely on the the free-running LD frequency, *i.e.*, ECM 0, the minimum-linewidth mode (MLM) at wavelength 1550 nm. [We reference all optical frequencies to the frequency f_{MLM} of the MLM in the plots below. In other words, the MLM frequency f_{MLM} in the figures corresponds to the zero of the optical-frequency scale.]

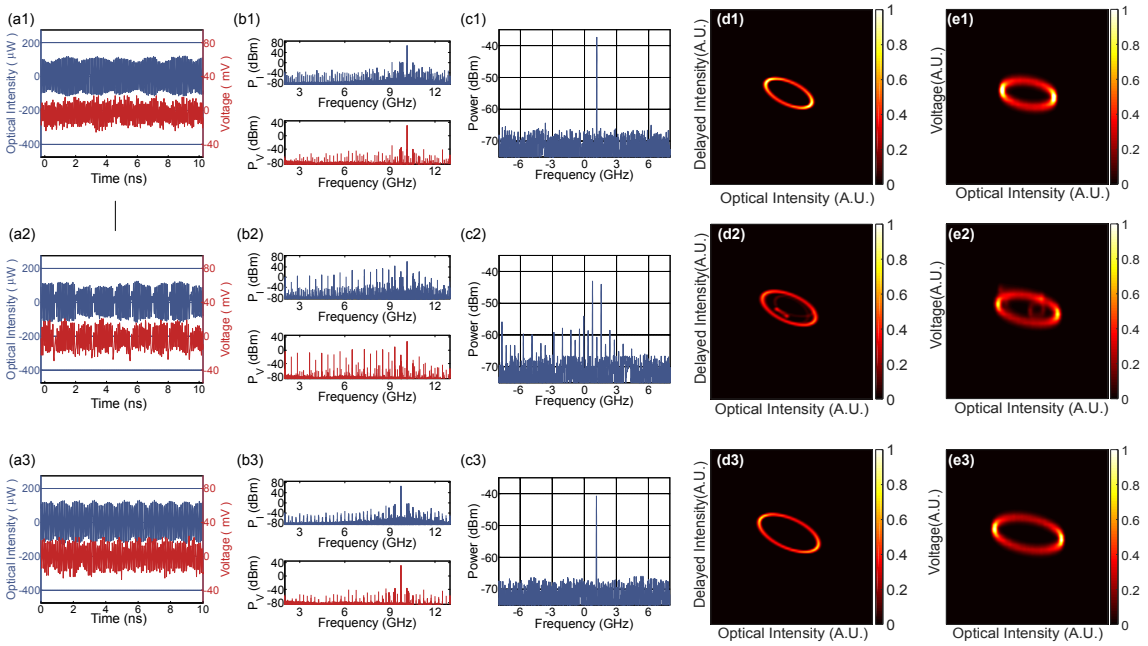

Figure 2.5: The dynamics in the LC regime with (a1), (b1), (c1), (d1), (e1) $\eta = 0.303$, (a2), (b2), (c2), (d2), (e2) $\eta = 0.365$, and (a3), (b3), (c3), (d3), (e3) $\eta = 0.383$. The phase portraits based on intensity vs. delayed intensity (intensity vs. voltage) are shown in the forth column (fifth column).

The Fourier transform of the TS is commonly referred to as the radio-frequency (RF) spectrum to distinguish it from the optic spectrum, *i.e.*, the Fourier transform of the optical field. The RF spectra of $I(t)$ and $V(t)$ are shown in Fig. 2.3(b). Note that they are broad and featureless, reflecting the near-constant state of $I(t)$ and $V(t)$ with broadband noise under CW operation. Figure 2.3(c) shows the optical spectrum obtained at the same time as the TSs. Note the single dominant peak at the MLM, ECM 0. We show the reconstructed and the real phase portraits in Fig. 2.3 (d) and (e), respectively. The two phase portraits show similar CW behavior; however, for Fig. 2.3(e), the phase portrait exhibits more anisotropy in $I(t)$ and $V(t)$ due to the different noise sources that contribute directly to $I(t)$ and $V(t)$.

As η is increased above 0.07, but remaining less than 0.29, the dynamical behavior undergoes a qualitative change, known as a Hopf bifurcation, to quasi-periodic (QP). QP denotes dynamics having features that appear periodically, though strictly speaking, the TS is not periodic, as seen in Fig. 2.4(a). The RF frequencies contributing to the TSs

are concentrated above $\sim$8 GHz, shown in Fig. 2.4(b). Many active ECMs (~ -10 to 4) participate, as seen in Fig. 2.4(c).

The observed QP dynamics can be described as a periodic switching between CW (constant) and limit-cycle (LC) (oscillatory) behaviors (a LC is a closed trajectory in phase space); the LC-like behavior which originates from ROs, becomes more dominant as η increases across this range with the intervals of CW-like behavior becoming relatively shorter. We see the corresponding phase portraits in Fig. 2.4(d) and (e). There are central broadened bright spots corresponding to the CW-like behavior and a ring-shaped feature corresponding to the LC-like behavior in both phase portraits. Note, however, that the low-amplitude portions of $V(t)$ are less frequent than the time-averaged value of $V(t)$ [see red curve in Fig. 2.4(a)], resulting in the bright spot appearing on the edge of the ring in the phase portrait involving $I(t)$ and $V(t)$. In addition, while both phase portraits show a semimajor axis of negative slope, the absolute value of the slope in Fig. 2.4(e) is less than that in Fig. 2.4(d).

Multiple limit cycles

At $\eta = 0.29$, the ECSL undergoes a bifurcation into a LC regime [107]; at this point, CW-like behavior no longer appears. Several LCs are observed for various η in this regime, as seen in the region labelled LC in Fig. 2.2(b) where, apart from narrow ranges of η, the BD exhibits two high-density features for a given η consistent with the approximately sinusoidal behavior of the corresponding TSs as discussed below. Two such LCs are shown in Fig. 2.5(a1) (TSs), (b1) (RF spectra), (c1) (optical spectrum), and (d1) (phase portrait) and in Fig. 2.5(a3), (b3), (c3), and (d3). [Figure 2.5(a2), (b2), (c2), and (d2), however, show the corresponding plots in a narrow QP region between the two distinct LCs, as discussed shortly.] These closed trajectories correspond to RO-like oscillations that become undamped in the ECSL [104] in the coupled dynamics of $I(t)$ and $V(t)$.

We begin with the LC behavior shown in Fig. 2.5(a1), (b1), (c1), and (d1) and

in Fig. 2.5(a3), (b3), (c3), and (d3). The TSs in Fig. 2.5(a1) and (a3) show a strong sinusoidal modulation near the RO frequency with a more slowly modulated envelope. The corresponding RF spectra in Fig. 2.5(b1) for $\eta = 0.303$ is f_{RO}, while that in Fig. 2.5(b3) for $\eta = 0.383$ is $f_{RO} - f_\tau$. The optical spectra Fig. 2.5(c1) and (c3) show a single dominant ECM 3 for these two LCs. Lastly, the phase portraits Fig. 2.5(d1) and (d3) exhibit an elliptical structure with a slope indicating a $\pi/2$ phase, consistent with undamped ROs in the ECSL [103, 104, 105, 106, 107, 108].

Between these two LCs for a narrow range of $\eta \sim 0.365$ is a QP region shown in Fig. 2.5(a2), (b2), (c2), and (d2). Here, the TSs show a roughly periodic modulation between the two LC-like behaviors as seen in Fig. 2.5(b2). The RF spectra, however, are quite broad as the TSs involve quite abrupt modulation between the two LCs and involve the participation of ECMs other than the most dominant ones. This is shown in Fig. 2.5(c2); here, two optical frequencies close to f_{RO} dominate, while a broad but significant pedestal of other frequencies also plays a role. The phase portrait is shown in Fig. 2.5(d2). The gross features can be reproduced by overlaying the phase portraits Fig. 2.5(d1) and (d3) of the flanking LCs; however, one notes additional less-pronounced features as well that arise in part from transients during switching between the two LC-like behaviors. Both types of phase portraits in the LC regimes exhibit similar features the slopes of the major axes are slightly steeper for the reconstructed ones. For the phase portraits between two periodic windows, we observe small qualitative difference in the structure within the outer ellipse.

Subharmonic

As η is increased into the range 0.4-0.52, the ECSL is characterized by SH dynamics [30, 28, 29]. By SH we mean that the TSs are dominated by two (or more) frequencies that sum to $f_{RO} \pm m f_\tau$ with m an integer. In selected cases, we shall find it useful to plot phase portraits obtained from relatively short-duration TSs to differentiate qualitatively different behaviors that contribute to the SH dynamics at a given η. This will enable us to gain

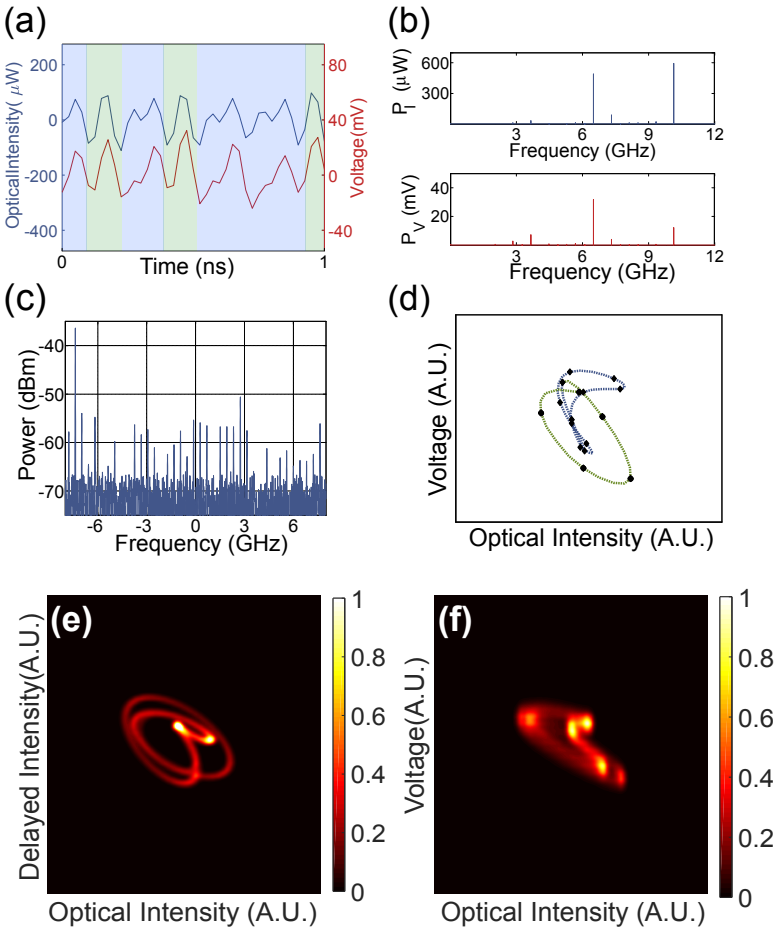

Figure 2.6: A 1 ns zoom-in on the dynamics in the SH regime with $\eta = 0.497$. (a) shows the $I_{AC}(t)$ and $V_{AC}(t)$ TSs and (b) the corresponding RF spectra and (c) the optical spectrum. The phase portrait is shown in (d) with short-duration TSs [0.4 ns] and (e) phase portraits based on delayed intensity and (f) voltage for long-duration [25 μs] TSs.

insight into what portions of the trajectory are associate with which RF frequencies.

Figure 2.6 shows (a) the TSs, (b) the RF spectra, (c) the optical spectra, and the phase portrait (d) with short-duration TSs [0.4 ns] and the reconstructed phase portrait (e) and intensity vs. voltage with long-duration [25 μ second] TSs. The TSs, shown in Fig. 2.6(a) exhibit oscillations near f_{RO}, that are themselves modulated at roughly $f_{RO}/2$ indicating a beating between two frequencies close to f_{RO}. This is supported by the appearance in Fig. 2.6 (b) of two dominant peaks in the RF spectra with frequencies $f_1 = 3.66$ GHz and $f_2 = 6.5$ GHz (other weaker peaks also appear); note that $f_1 + f_2 = f_{RO} = 10.16$

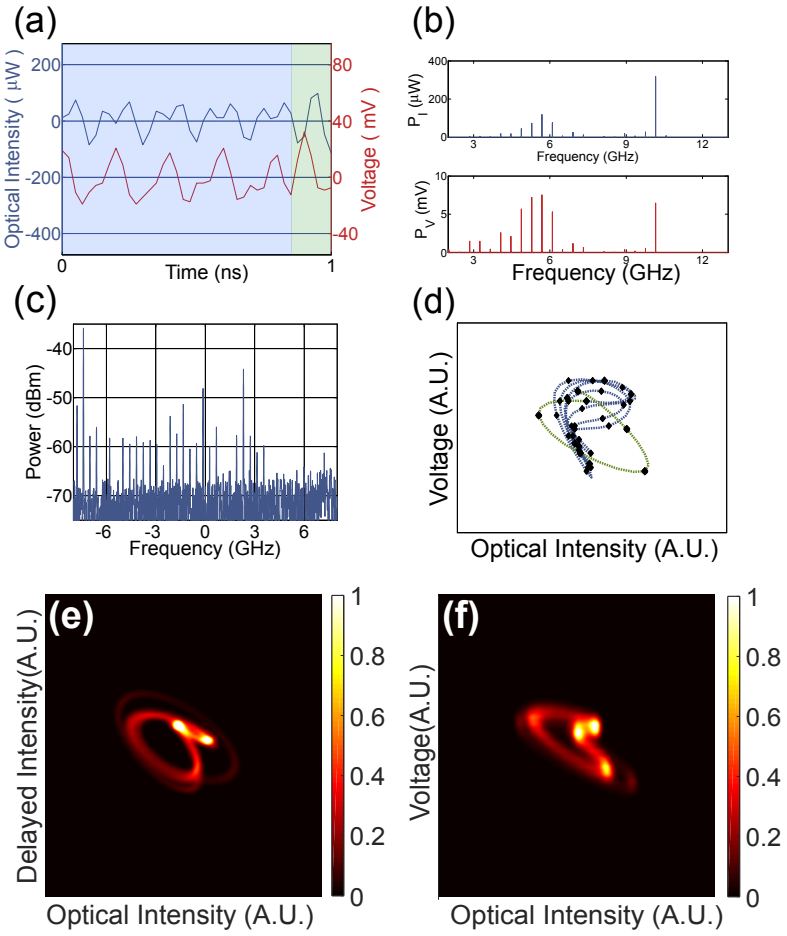

Figure 2.7: A 1 ns zoom-in on the dynamics in the different SH regime with $\eta = 0.517$. (a) shows the $I_{AC}(t)$ and $V_{AC}(t)$ TSs and (b) the corresponding RF spectra. (c) The optical spectrum. The phase portrait is shown in (d) with short-duration TSs [1.5 ns] and (e) phase portraits based on delayed intensity and (f) voltage for long-duration [25 μs] TSs.

GHz. The phase portrait using relatively short-duration TSs in Fig. 2.6 (d) emphasizes the nature of the dynamics. The RF frequency [Fig. 2.6(b)], $f_1 = 3.66$ GHz corresponds to the green structure and $f_2 = 6.5$ GHz corresponds to the blue structure. In Fig. 2.6(e), the reconstructed phase portrait shows two clear open structures that repeat in succession similarly to what is observed in the phase portrait obtained from $I(t)$ and $V(t)$ shown in Fig. 2.6(f). [The two structures can be distinguished as the green and blue portions of the phase portrait in Fig. 2.6 (d) and corresponding shaded regions of Fig. 2.6(a).] Nonetheless, there are distinct differences between the two types of phase portraits.

Figure 2.7 shows an example restricting our view to a different SH behavior for $\eta = 0.517$. In Fig. 2.7 (a) a shorter timescale is shown (1 ns) compared with that used in previous figures. The TSs appear roughly as sinusoidal modulated by an envelope at half the dominant frequency of the sinusoid [more apparent in the TS for $I(t)$]. This is the signature of the PD regime. What is evident from the TSs is born out in the RF spectra in Fig. 2.7(b). Here we see a dominant peak at f_{RO} and a cluster of peaks near $f_{RO}/2$. Figures 2.7(d) and (e) show the corresponding phase portraits, for (d) short-duration TSs [0.4 ns] and (e) long-duration [25 μs] TSs. Compared with what was seen in the SH regime at somewhat smaller η, far more time is spent on the blue trace and shaded region with (irregularly shaped) features reminiscent of PD dynamics than on the green trace and shaded region with features resembling behavior in the LC regime discussed above, in Fig. 7 (a) and (d). The RF spectrum corresponding to Fig. 2.7(b) shows a dominant peak at $f_{RO} = 10.16$ GHz while the TSs in stable PD have dominant peak at $f_{RO} + f_\tau = 10.56$. A smoothed curve connecting both regimes where the green (blue) curve is determined to be LC (PD). The two trajectories are mapped on the phase portrait in Fig. 2.7(d) where the PD regime is plotted in blue; and the LC trajectory is plotted in green. The diamonds (circles) are the raw data from the TSs. Lastly, the corresponding phase portrait based on intensity vs. delayed intensity is shown in Fig. 2.7(e) and intensity vs. voltage is shown in Fig. 2.7(f). The two types of phase portraits show overall similarity with differences in detail.

Period-doubled and intermittency

The PD regime for $\eta = 0.52$ to 0.64 is characterized by RF frequencies $f_{RO} = 10.16$ GHz and $f_{RO}/2$. We show here an example for $\eta = 0.55$, where we observe a PD regime as plotted in Fig. 2.8, with the TSs in (a), the RF spectra in (b), the optical spectrum in (c), and the phase portrait in (d). The main features are similar to those in Fig. 2.7. The dominant RF frequencies in Fig. 2.8(b) are $f_{RO} + f_\tau = 10.56$ GHz and $(f_{RO} + f_\tau)/2 = 5.28$ GHz compared with $f_{RO} = 10.16$ GHz and $f_{RO}/2 = 5.08$ GHz in Fig. 2.7. Note that even

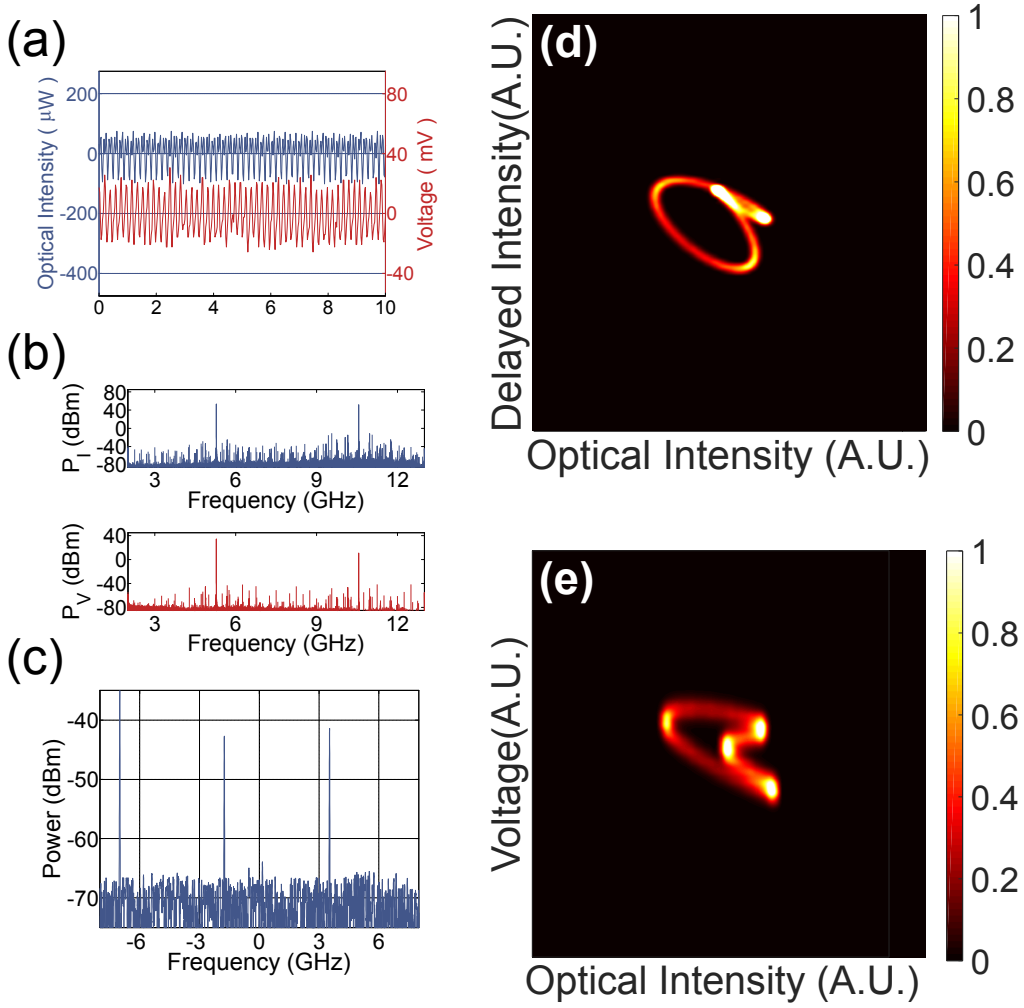

Figure 2.8: The dynamics in the PD regime with $\eta = 0.55$. (a) $I_{AC}(t)$ and $V_{AC}(t)$ and (b) corresponding RF spectra. (c) The optical spectrum and phase portrait based on (d) intensity vs. delayed intensity (e) and intensity vs. voltage.

though the reconstructed [Fig. 2.8(d)] and the directly obtained phase portraits [Fig. 2.8(e)] have similar overall shape as the phase portrait (green) in Fig. 2.7(d), the two TSs do not have the same dominant RF frequencies. The transition of the dynamical behavior varies from SH to PD involves the formation of a stable solution. The RF peak in SH is found to be $f_\tau + f_{RO}$ and the trajectories are comprised of an LC and a PD, as the feedback strength increases. As feedback is increased, we find the duration of PD increases, and the trajectories become more dominant until PD takes over and the new solution is found to be PD with RF peak at f_{RO}.

We illustrate intermittency at $\eta = 0.545$ which is evident within a single TS shown

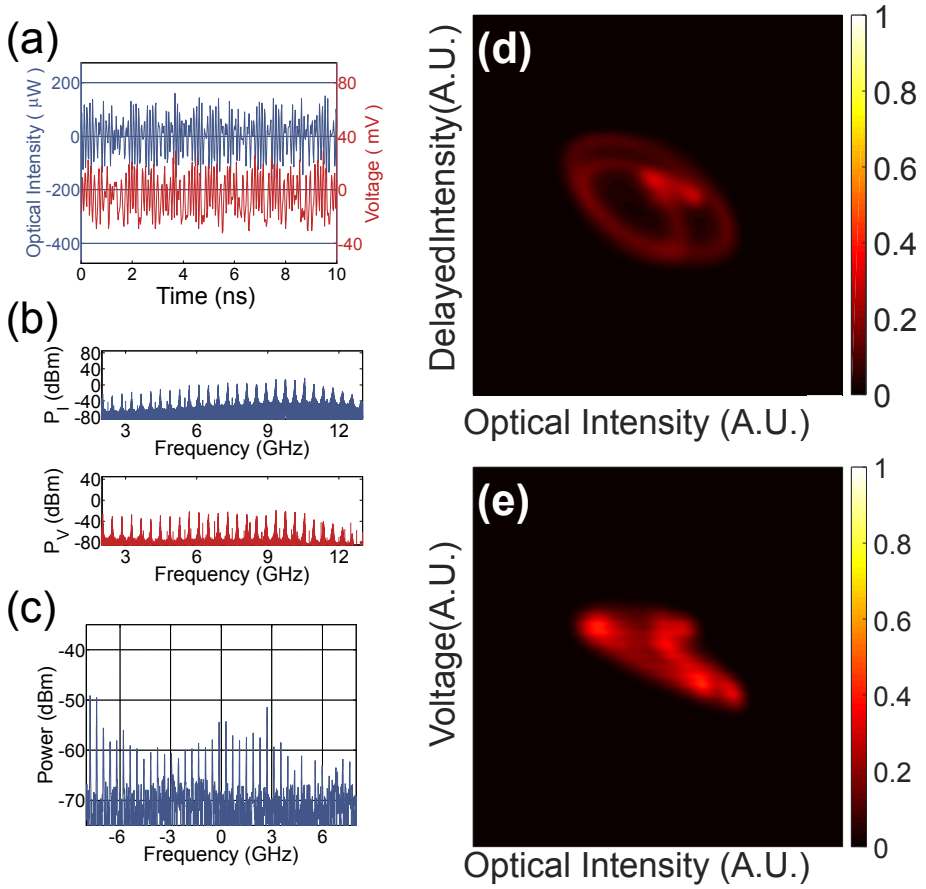

Figure 2.9: The dynamics in the intermittent regime with $\eta = 0.55$. (a) $I_{AC}(t)$ and $V_{AC}(t)$ and (b) corresponding RF spectra. (c) The optical spectrum and phase portrait based on (d) intensity vs. delayed intensity (e) and intensity vs. voltage.

in Fig. 2.9 and the animation in the supplement material. This type of intermittency has been investigated in Ref. [109], we can identify chaotic and PD along with other complex dynamics shown in Figs. 2.9(a)-(e). The sequential order of the dynamics in this TS appear to be random which can be found in the animation in the supplement material. We see considerable broadening of the features compared with the PD phase portrait in Fig. 2.7. The phase portrait exhibits an overall elliptical structure (LC-like behavior) together with enhanced density in the upper right of the phase portrait associated with PD-like behavior, with considerably more time spent on the PD-like phase ($\sim 35:1$). A more detailed examination of the phase portrait over many shorter duration TSs bears out this interpretation. The PD-like dynamics here differ somewhat from those shown in Fig. 2.8.

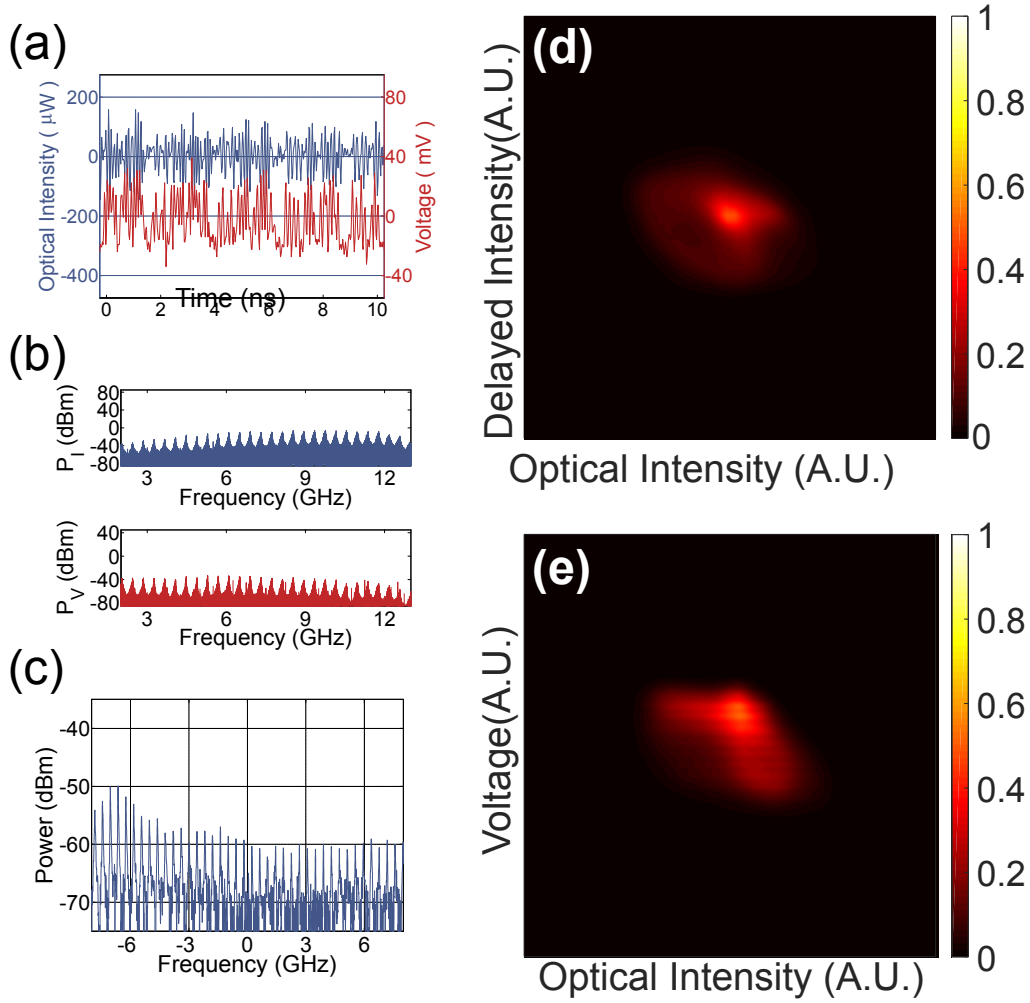

Figure 2.10: The dynamics in the CC regime with $\eta = 0.75$. (a) $I_{AC}(t)$ and $V_{AC}(t)$ and (b) corresponding RF spectra. (c) The optical spectrum and phase portrait based on (d) intensity vs. delayed intensity (e) and intensity vs. voltage.

As η is further increased above 0.64 the onset of chaos is reached. An example for $\eta = 0.75$ is shown in Fig. 2.10. In this regime, the BDs of Fig. 2.2(a) and (b) are quite broadened in the vertical direction indicating many maxima and minima in the respective TSs as well as the participation of numerous ECMs [Fig. 2.2(c)]. The TSs [Fig. 2.10(a)] become quite complex and involve a very broad range of RF frequencies [Fig. 2.10(b)]. Likewise, many ECMs participate in the dynamics [Fig. 2.10(c)]. Both phase portrait

(The reconstructed phase portrait, [Fig. 2.10(d)], and the real phase portrait [Fig. 2.10(e)]), consequently, has an undifferentiated broadened feature with a hint of elliptical structure (reflecting the continues role of RO oscillations). Both voltage and intensity signals share similar degree of complexity [10], however, the real phase portraits appears to be less symmetric along the vertical direction (voltage signal).

The complex dynamics of ECSLs correspond to trajectories in phase space whose qualitative nature undergoes pronounced changes as a control parameter (here η) is varied. Until now, the overwhelming majority of experimental results have been obtained on just one dynamical degree of freedom, *viz.* $I(t)$. By simultaneously measuring $I(t)$ and $V(t)$, however, we obtain new insight into the nonlinear dynamics of ECSLs based on two degrees of freedom; in our case projecting phase space in the ϕ direction. The resulting phase portraits can be used to track the trajectory's motion between the various ECMs of the ECSL. The importance of the ability to visualize the dynamics itself should not be underestimated. As shown here, that ability enables us to attain insight into rather complex dynamical regimes that would be otherwise difficult to understand.

2.4 Optoelectronic oscillator based on an ECSL setup

Microwave optoelectronic oscillators (OEO) have attracted attention due to the tunability and stability of low-power laser diodes (LD) [110, 54]. OEOs enable tremendous flexibility; the optical signal can be converted immediately to a microwave electrical signal via a fast photodiode (PD) or can be transmitted over low-loss optical fiber to be converted downstream to a microwave electrical signal, again by a PD.

There are several approaches to achieving OEOs. One common approach is to beat two phase-locked optical waves [56, 57]; others are based on optical injection of a master laser into a slave laser [111] or electro-optic modulators [55, 112].

While in some implementations, the optical signal is used to convey the microwave information for later optical-to-electrical (O/E) conversion, for a number of applications,

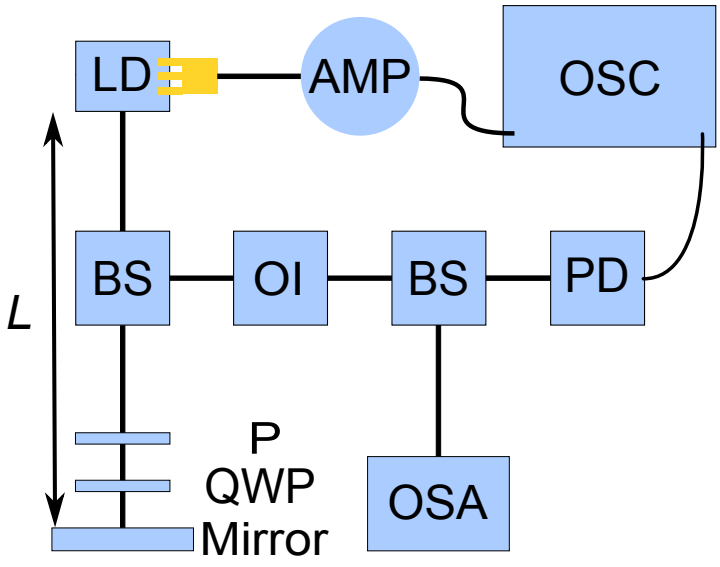

Figure 2.11: Experimental setup. LD: laser diode, AMP: RF amplifier, OSC: oscilloscope, BS: beam splitter, OI: optical isolator, PD: photodiode, P: polarizer, QWP: quarter-wave plate, and OSA: optical spectrum analyzer.

the optical signal [time-dependent optical intensity $I(t)$] itself is of no intrinsic interest. Instead, O/E conversion is carried out proximate to the optical generation by one or more PDs. Nonetheless, in all cases of which we are aware, a PD separate from the LD is required to generate the electrical signal. Eliminating the O/E conversion, therefore, would be a simplification in a large class of OEO-based systems. Here, we demonstrate two types of OEOs, the tunable X-band OEO and the chaotic OEO based on an external-cavity semiconductor laser (ECSL) in which the microwave electrical signal is generated directly by monitoring the voltage $V(t)$ across the injection terminals of the LD under constant-current J conditions

2.4.1 Chaotic Multi-GHz OEO

In this subsection, we demonstrate a chaotic multi-GHz OEO based on an ECSL with *direct* chaotic microwave electrical generation. In other words, our approach entirely obviates the use of a PD by directly monitoring the time-dependent voltage $V(t)$ across the injection terminals of the laser diode under constant-current J injection. We verify that the

dynamics exhibited by $V(t)$ is indeed chaotic and of comparable dynamical complexity as that of $I(t)$ by means of a largest-Lyapunov-exponent (LLE) analysis. The basis for our observation is that for small signals, $V(t)$ is proportional to the inversion $N(t)$ in the gain medium, as was pointed out in Refs. [43, 45, 113]. The dynamics of $N(t)$ and $I(t)$, in turn, are closely linked, as is understood, for example, on the basis of the Lang-Kobayashi equations [25]. Recently, an investigation of the voltage $V(t)$ across the LD but focused uniquely on its use, in conjunction with a phase measurement, to describe and understand the regime of low-frequency fluctuations [27].

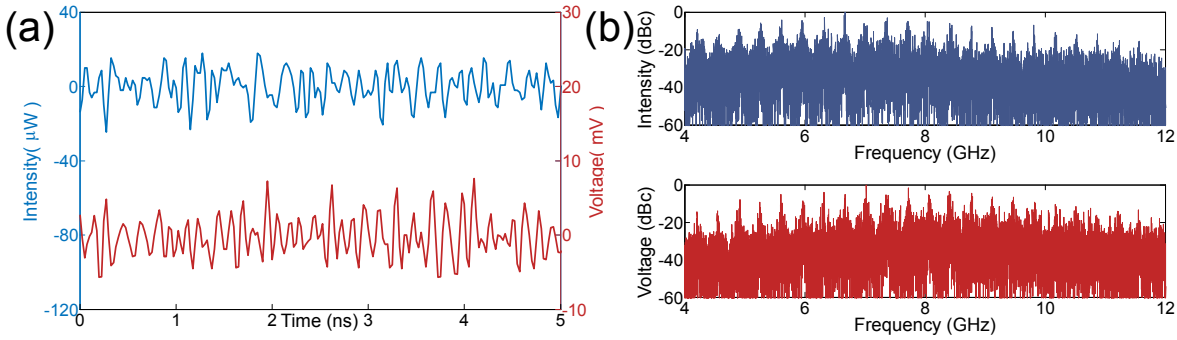

Figure 2.12: (a) The optical (blue) and voltage time series (red) of a chaotic time series are shown in the left panel with calibrated time delay. (b) The power spectrum of each time series is shown on the right, the peaks are separated by $f_\tau = 0.35$ GHz.

As we further increase the feedback strength above $\eta > 0.23$, we enter region δ of the BDs (Fig. 2.2), $V(t)$ and $I(t)$ reveal an apparently erratic behavior [Fig. 2.10] and the corresponding spectra show considerable broadening [Fig. 2.17 (b)], as the 6 dB bandwidth is approximately 4.56 GHz. The suspected chaotic behavior in region δ is confirmed by evaluating the (LLE) from the time series of both I and V. The LLE in this section is computed by

$$LLE = \lim_{t\to\infty} \frac{1}{t} \ln[\frac{|\delta x(t)|}{|\delta x(t_0)|}]$$

The LLE has been computed using the standard tools provided by Kantz. *et. al* [114, 115, 116]. In Fig. 2.13, the value of LLE is plotted as a function of feedback strength for both optical intensity and voltage. We obtain consistently a (strictly) positive and similar

value of the LLE from the analysis of I or V in region CC, confirming the chaotic nature of the dynamical behavior. Although further work must be carried out, these results indicate that both $I(t)$ and $V(t)$ exhibit comparable chaotic characteristics. Moreover, we observe an increase of the LLE with η, indicating tunability of chaos complexity in the proposed OEO. Although not shown here, we have further confirmed the robustness of these observations by resolving BDs for various values of L (30, 42, and 70 cm) and J (50, 60, and 70 mA) which enables further tunability of the RF spectrum and chaos complexity. In region δ, the bandwidth of $V(t)$ where the ECSL is in coherence collapse (well developed chaos) extends up to 8GHz.

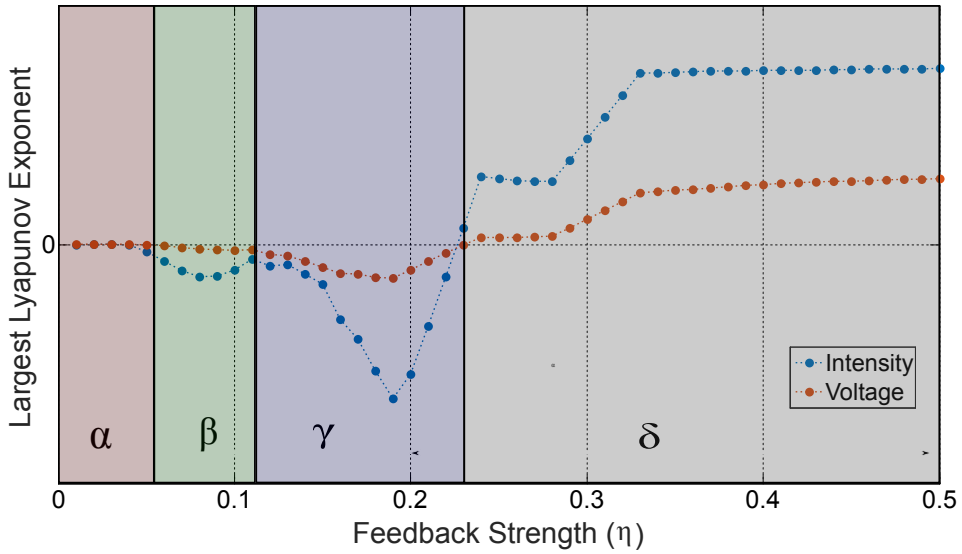

Figure 2.13: The largest Lyapunov exponent is plotted as a function of increasing feedback strength for both the optical intensity and voltage across the laser diode. The value is negative or zero when we are in the CW (α), quasi-periodicity (β), and periodic (γ) regimes. As we enter the coherence collapse regime (δ) the exponent becomes positive indicating chaos.

2.4.2 Tunable X-band optoelectronic oscillators

Microwave signals are commonly used in communications, radar, and medical imaging. High-frequency microwave waveforms are conventionally generated in the electrical

domain using digital electronics and typically involve several stages of multipliers and amplifiers. This approach, however, may be inefficient at frequency ranges higher than a few GHz. Another possibility is to generate microwave waveforms in the optical domain, to take advantage of the broad bandwidth and low attenuation in the optical system.

Optoelectronic oscillators (OEO) have attracted attention due to the tunability and stability of low-power LD [54, 110]. One common approach is to beat two phase-locked optical waves [56, 57]; another is based on the optical injection of a master laser into a slave laser [117] or electro-optic modulators [55, 118]. Optical generation of microwave signals enables tremendous flexibility; the optical signal can be converted immediately to a microwave electrical signal via a fast photodiode (PD) or it can be transmitted over low-loss optical fiber systems to be converted downstream to an electrical microwave signal. In the future, on-chip OEO miniaturization and integration may be pursued [54], leading to compact and robust OEOs.

In this section, we demonstrate an OEO based on an external-cavity semiconductor laser (ECSL) configuration. The OEO extracts the electrical microwave signal directly by monitoring the voltage $V(t)$ across the injection terminals of the LD under constant-current J conditions. The periodic optical intensity $I(t)$ may also be used for microwave generation if so desired. Tunability across the entire X-band is achieved by varying J. In broad terms, in a periodic regime in an ECSL, oscillations in $I(t)$ and $V(t)$ occur that are $\sim \pi$ out of phase, *i.e.*, one observes relaxation oscillations. As is well known, a small-signals analysis shows that $V(t)$ is proportional to the inversion $N(t)$ in the LD active region [43, 45, 119].

In a periodic dynamical regime in an ECSL, oscillations in $I(t)$ and $V(t)$ occur that are $\sim \pi/2$ out of phase (though the true dynamics as predicted by the Lang-Kobayashi equations [25] are somewhat different), *i.e.*, one observes undamped relaxation oscillations at frequency f_{RO}. With the monotonic dependency of f_{RO} on the injection current, the tunability across the entire X-band is achieved by varying the injection current J. As is well known, $V(t)$ is directly related to the inversion $N(t)$ in the LD active region [43, 45,

113]. We find, for our LD, that the amplitude of the oscillations in $V(t)$ is around 278 μV, the oscillation frequency is tunable from 6.79 to 11.48 GHz (the upper limit here is due to the frequency cutoff of our oscilloscope). The oscillation frequency is created by a Hopf bifurcation of an external-cavity mode. It has been shown that its frequency close to the relaxation-oscillation frequency depends on the pumping current, J and the feedback strength [101, 104, 120]. Typical values of the timing jitter are $\lesssim 10$ ps, and the quality factor Q is $\gtrsim 2 \times 10^5$. The combination of wide tunability and low noise figures of merit may make this device competitive with state-of-the art OEOs.

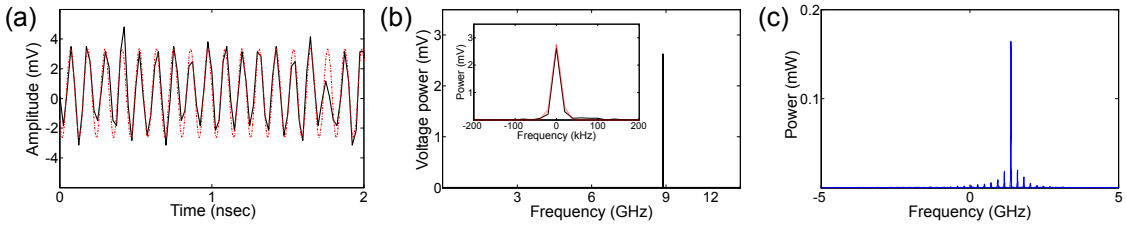

Figure 2.14: (a) $V(t)$ (black) and the fitted sinusoid (red dotted line). (b) RF spectrum of $V(t)$ while the inset shows the spectrum on an expanded frequency scale (adjusted so that 0 kHz lies at line center ($Q \approx 3.5 \times 10^5$). A Gaussian fit of the spectrum is represented with a red dotted line. (c) Corresponding optical spectrum, where the frequency of the solitary laser is set to zero. All data are acquired simultaneously with $J = 70$ mA, $L = 68$ cm, and $\eta = 0.19$.

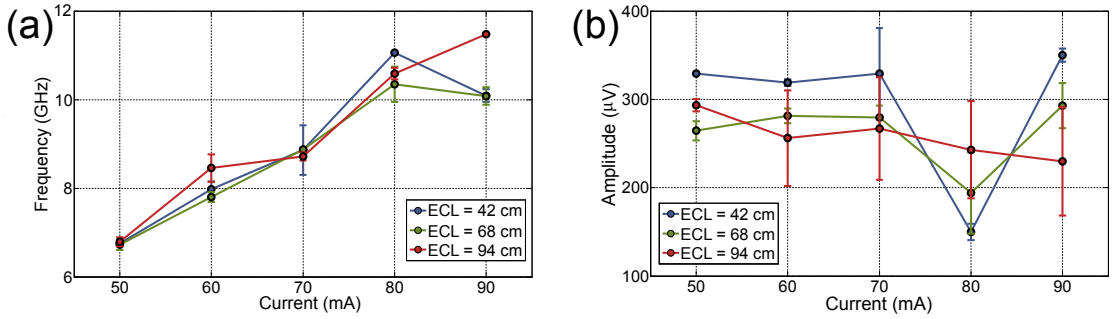

Figure 2.15: The measured frequencies (a) and amplitudes (b) of the periodic OEO as functions of current at different external cavity lengths (L = 42 cm, 66 cm and 82 cm).

We now focus on the case when $J = 70$ mA, $L = 66$ cm ($f_\tau = 0.22$ GHz), where relaxation-oscillation frequency $f_{RO} = 8.87$ GHz, $\eta = 0.13$, and $L = 68$ cm. In addition,

we heretofore concentrate on $V(t)$. The time series for $V(t)$ is shown in Fig. 2.14 (a). The signal is seen to be highly periodic, though contains amplitude fluctuations and timing jitter (see below for quantitative characterization). Fig. 2.14 (b) shows that the periodicity is characterized by $f_{RO} = 8.87$ GHz with weak sidebands separated by f_τ. In Fig. 2.14(c), we present the optical spectrum of $I(t)$ and observe that one external cavity mode (ECM) dominates. This is the 6th ECM mode to the right of the minimum linewidth mode [36, 37]. Its frequency is of 1.39 GHz on the optical-frequency scale of Fig. 3(c) corresponding to an ECM at 1552.07 nm (193.33 THz).

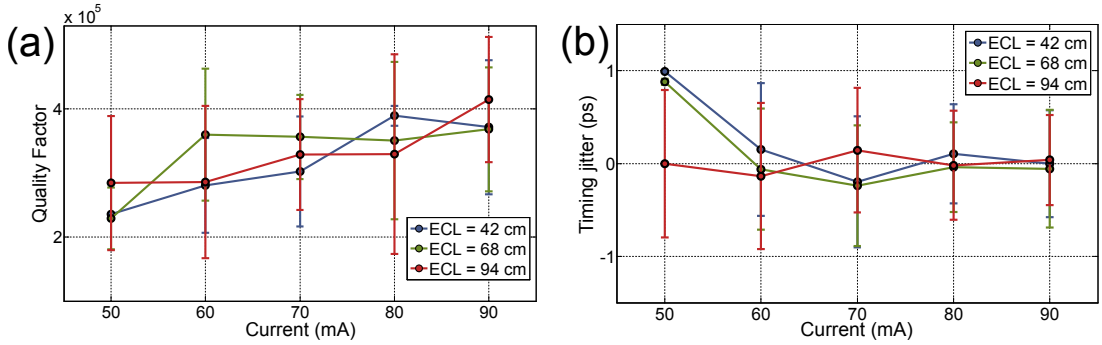

Figure 2.16: The quality factor (a) and the timing jitter (b) of the periodic OEO as a function of current at different external cavity lengths, L.

We have carried out similar measurements for $J = 50$, 60, 70, 80, and 90 mA and $L = 42$, 68, and 94 cm. Fig. 2.15 (a) shows the periodic frequency as a function of current for the various parameters. We see that with ECSLs based on this single LD, tunability between 6.79 to 11.48 GHz is accessible. As seen in Fig. 2.15 (b), we attain sub-millivolt electrical signals. The power consumption is 0.23 W with $J = 70$ mA. We find that the amplitude of the oscillations in $V(t)$ are around 278 μV for our LD, the oscillation frequency is tunable from 6.79 to 11.48 GHz (the upper limit due to the frequency cutoff of our oscilloscope). Typical values of the timing jitter are ~ 0.13 ps, and the quality factor Q is $\sim 3.4 \times 10^5$. Note that this signal has been amplified, which may increase jitter.

To evaluate the performance of an optical system, it is very important to correctly estimate the Q-factor and the timing jitter, σ_{tj}. The Q-factor is plotted in Fig. 2.16 (a) for

System	Fabry-Perot	Bragg Grating	Optical Filter	Our System
Phase Noise (dBc/Hz)	-92.8	-102	-120	-80 (estimated)
Tunability (GHz)	$6.41 - 10.85$	$3 - 28$	$4.74 - 38.38$	$6.79 - 11.48$

Table 2.2: A comparison of state of the art OEOs. All phase noise values are at 10 kHz offset.

various parameters. On the other hand, timing jitter can characterize the spectral purity of the microwave oscillations. Fig. 2.16 (b) shows the dependence of the timing jitter as function of current for various external cavity lengths. We can determine the typical timing jitter is at the order of 0.13 ps, which corresponds to $\sigma_{tj}/T_c = 1.1 \times 10^{-3}$ of the periodic.

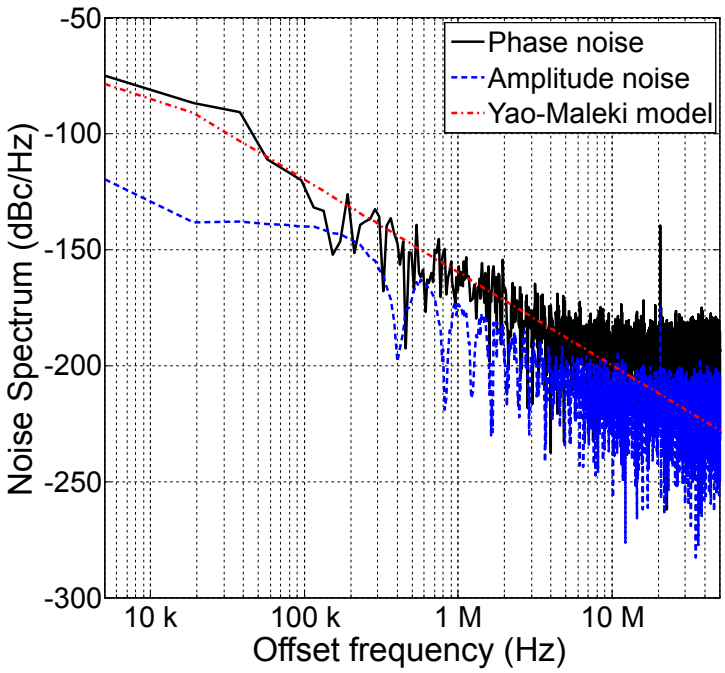

Figure 2.17: The noise spectrum for amplitude (blue) and phase noises (black) with $J = 90$mA, $L = 94$ cm, and $\eta = 0.19$. The phase noise is determined to be -79.3 dBc/Hz at 10 kHz offset frequency by fitting with a Yao-Maleki model[55].

In Fig. 2.17, we plot the noise density spectrum for both amplitude and phase for $J = 90$ mA, $L = 94$ cm, and $\eta = 0.19$. We determined the phase noise to be -86.3 dBc/Hz at 20 kHz offset frequency. Due to resolution limitations, we are unable to obtain a direct measurement of the phase-noise spectral density at 10 kHz offset; however, we

have fit our phase-noise spectrum to a Yao-Maleki model [55] and extrapolated the phase noise to be -79.3 dBc/Hz at 10 kHz offset frequency. In addition, we confirmed that the value is smaller than -80 dBc/Hz for all values of current and delay tested in this paper. An estimated value of the phase noise spectral density at 10 kHz offset is found to be -80 dBc/Hz. The phase-noise performance of our OEO setup may be improved by choosing the feedback time to be a multiple of the relaxation-oscillation time; in this way, one may average out phase fluctuations [121, 122].

2.4.3 Improvement of X-band optoelectronic oscillators

We have demonstrated a multi-GHz OEO in the previous section; we attain periodic electrical signals with a bandwidth extending from hundreds of MHz to at least 12 GHz (the frequency cutoff of our measurement capability). The possibility of controlling chaos in an external-cavity laser diode with impulsive delayed feedback through optoelectronic conversion has been demonstrated [123, 124]. A electrical feedback configuration will improve the performance of the periodic OEO waveform generation. It is noteworthy that the well-tested Lang-Kobayashi model suggests significant spectral content may extend up to a few tens of GHz.

The first stabilization technique was based on self-modulation of the system. A diagram of the self-modulation system can be seen in the dashed box Fig. 1. Essentially, a beam splitter was placed in the external cavity such that half the optical power could be extracted and converted to electrical energy by a photodiode. The resulting electrical signal was directly modulated across the terminal of the laser diode. A major advantage of the OEO is the fact that, the only items needed are a laser, reflective surface, and a way to set feedback strength. Thus a method to decrease phase jitter but, keep the system relatively simple is desirable. Therefore, the second method attempted was achieved by setting the f_{ROF} to be an integer multiple of f_τ. This can be achieved by adjusting the delay time of the external cavity, τ in Fig. 2.19. By setting the frequencies to be a multiple of each

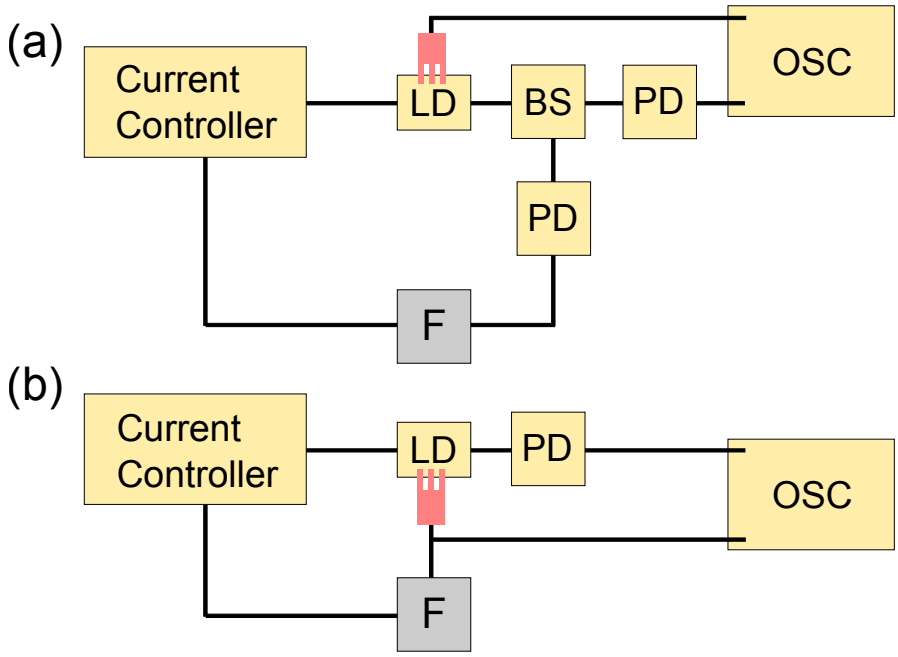

Figure 2.18: Illustration of two potential feedback schemes to optimize periodic OEO. (a) Feedback control utilizes optoelectronic conversion with optoelectronic has demonstrated chaos control. (b) A feedback control scheme using voltage signal provides electronic feedback.

Un-stabilized	Resonance	Feedback
16.08 ps	1.38 ps	1.24 ps

Table 2.3: Timing jitter for the unstabilized OEO, the resonance locking based OEO, and using self-feedback

other, we could achieve resonance locking in the system and lower phase jitter while not increasing the number of components in the system.

A summary of the results can be seen in Table 2.4.3, there is an order of magnitude reduction in phase jitter for both stabilization techniques. The self-modulation system, gives a reduction in phase jitter to 1.24 ps. The modulation leads to an increase in coherence, and therefore a reduction in jitter is observed, but it requires extraneous equipment, including, a photodiode. Meanwhile, by tuning the length of the external cavity we see a decrease to 1.38 ps, and the difference in phase jitter is evident from the comparison in Fig. 2, where the OEO is un-stabilized (a) and (b) and stabilized using frequency locking (c) and

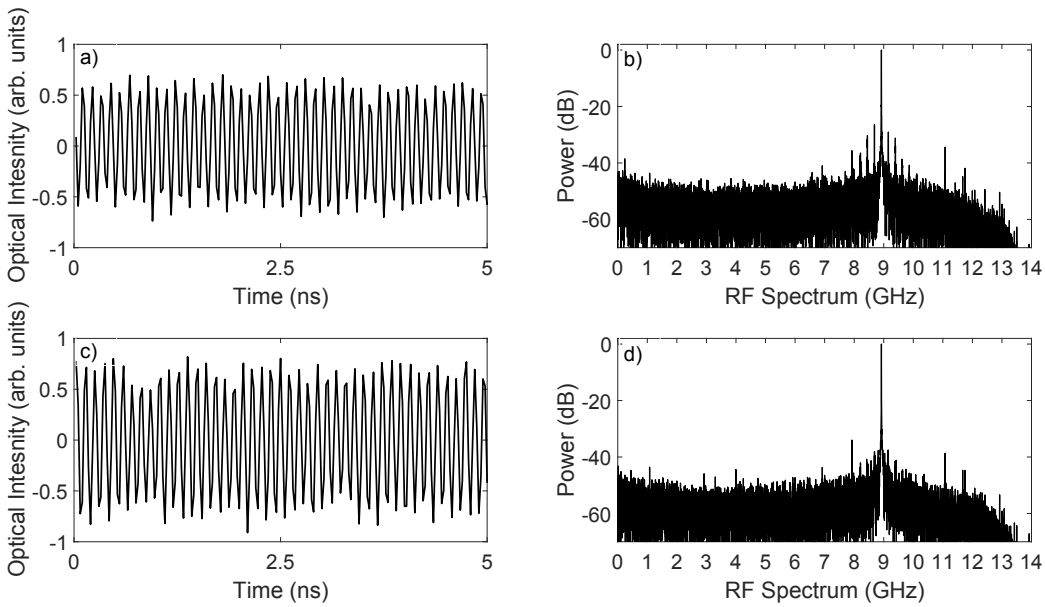

Figure 2.19: The time-series and RF spectrum of the OEO without stabilization, (a) and (b). The time-series and RF spectrum of the OEO with resonance locking, (c) and (d). We see a reduction in side-band noise in the RF spectrum which indicates a reduction in phase jitter.

(d). We suspect the reduction in phase jitter for resonance locking is caused by averaging out the phase jitter.

In conclusion, We have shown that the voltage $V(t)$ across the LD allows for the robust generation of periodic, quasi-periodic, and chaotic oscillations, of various complexity, that have similar characteristics to those obtained from the optical intensity. We demonstrate a ECSL-based OEO that entirely circumvents the need for O/E conversion. The use of an ECSL as a **periodic** OEO is tunable across the entire X-band, from 6.79 to 11.48 GHz. Both the optical $I(t)$ and electrical $V(t)$ signal can be employed for microwave applications. The typical values of Q is 3.4×10^5. In addition, we have characterized the spectral purity via the time jitter and have found timing jitter is 0.13 ps (in the range $\sigma \approx -0.79$ to 0.88) and the $\sigma_{tj}/T_{per}(J) = 1.1 \times 10^{-3}$. Thus, the use of an ECSL as a **chaotic** OEO for straightforward and inexpensive sources of high-dimensional chaos [50], is of interest for applications such as chaos radar [51] and ultrahigh rate random-bit generation [8, 52, 9].

Moreover, we demonstrated that by applying the Pyragas type feedback [3] can be reduced unstable orbits. To be more specific, self-modulation of the system by setting the f_{ROF} to be an integer multiple of f_τ in the periodic OEO, we have demonstrated a magnitude improvement of the timing jitter.

CHAPTER 3

TIME-DELAYED FEEDBACK FOR A SINGLE PHOTON

In this chapter, we investigate the effect of the coherent quantum feedback loop shown in Fig. 3.1. Detailed description of such system is presented in section 3.1, and the application of coherent feedback, specifically, the effects of Pyragas type feedback is investigated in section 3.2. We demonstrate the optical nonlinearity feature for different photon number for state population in section 3.3. We discuss the stationary superposition states based on the parity exchange of the QD and the MC photon state for one- and two- excitation states in section 3.4. Lastly, we analyze the stability of the coherent quantum feedback in the vicinity of the stationary states in section 3.5.

3.1 Model and Simulation

We describe the dynamics of a single photon emitter couples to an ideal mirror, *i.e.,* the derivation of the interaction Hamiltonian in Eq. (1) in the main text. The detailed process of the interaction Hamiltonian is also given in derivation of quantum stochastic Schrödinger equation N.L. Naumann *et. al.,* [125], and by H. Pichler *et. al.,* [95] recently.

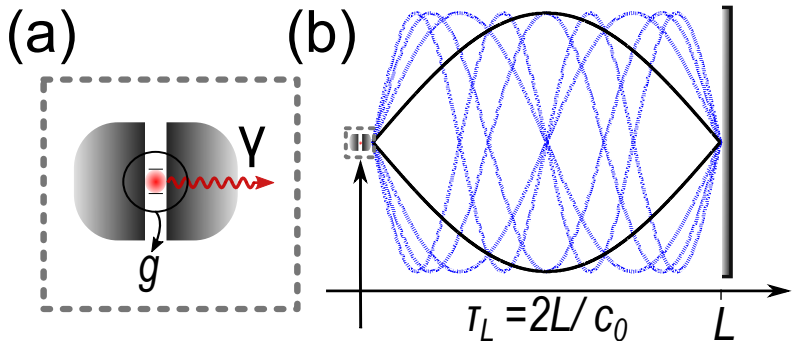

Figure 3.1: (a) Schematic of a QD in a MC. (b) The QD-MC system coupled to a long EC of length L in which a quasi-continuum of photon modes exist. τ_L is the delay time of the coherent feedback.

We consider an intrinsic QD coupled to a single mode of a high-Q micropillar cavity [Fig. 3.1 (a)] and coupled to the EC modes shown in Fig. 3.1 (b). The QD is characterized by interband-transition frequency, ω_0. The QD interband transition is dipole coupled to a single mode of the micropillar cavity with coupling strength, g, as in [67]. This approach can yield strong coupling between the QD and the MC [97] and can generate high-purity, indistinguishable single photons [67]. We place an ideal mirror with amplitude reflection coefficient $r = 1$ a distance $L = c_0\tau_L/2$ from the micropillar, with c_0 the speed of light in vacuum and τ_L the feedback time. The conditions we choose are similar to the single QD in a MC subjected to an external mirror in a recent paper [94]. For a mirror with $|r|^2 < 1$, the coherent feedback can be treated using an open quantum-system formalism, discussed in a recent publication by Whalem [126].

The system Hamiltonian for the two-level system with quantum feedback is $H_{sys} = H_e + H_{field} + H_{int}$. We briefly discuss each term below:

The Hamiltonian dealing with the internal state for the electronic two-level system being

$$H_e = \frac{\hbar(\omega_c + \omega_v)}{2}\hat{I} + \frac{\hbar\omega_{cv}}{2}(\sigma^+\sigma^- - \sigma^-\sigma^+) \tag{3.1}$$

Here, $\omega_{c/v}$ being the angular frequency in the excited state (conduction band) and ground state (single vanence band), respectively. $\sigma^{+(-)}$ being the raising (lowering) operator of the two-level QD system. A microcavity can be manufactured such that the single cavity mode is match to the transition frequency, $\omega_c - \omega_v = \omega_{cv}$. We chose the *zero*th energy to be $(\omega_c + \omega_v)/2$ and obtained the $H_e = \frac{\hbar\omega_{cv}}{2}(\sigma^+\sigma^- - \sigma^-\sigma^+)$.

The field Hamiltonian describes two optical fields in the system, $H_{field} = H_{field,\,\mu} + H_{field,\,EC}$. The single optical mode within the micropillar cavity is described by

$$H_{field,\,\mu} = \hbar\omega_\mu a^\dagger a \tag{3.2}$$

with $a^{\dagger}(a)$ being the creation (annihilation) operator for the photon in the micropillar cavity, ω_{μ} being angular frequency for the single cavity mode and is designed to match the transition frequency of electronic state $\omega_{\mu} = \omega_{cv}$. The external photon in the external cavity is described by

$$H_{field,\ EC} = \hbar \int \mathrm{d}\omega_k\ \omega_k b_k^{\dagger} b_k \tag{3.3}$$

Here, the bosonic operators $b_k(\omega)$ destroy a photon of frequency ω_k in the external cavity. We used the free space dispersion relationship, $\omega_k = c|k|$, for the photons populate in the external cavity. Among these states, we assume that only the states of optical modes with angular frequencies near the transition frequency interact strongly with the microcavity photon ($\omega_k \approx \omega_{cv}$). As a result, we extend the integration limits to negative values up to minus infinity.

We obtain following interaction Hamiltonian of single photon emitter with photon population in the external cavity modes. The H_{int} is the interaction Hamiltonian describing both interaction of the QD and the microcavity photon and the dissipative interaction between the micropillar cavity photon and external cavity photon [127, 93, 94]. For systems with symmetric coupling strength with unity feedback, the dynamics is govern by the interaction Hamiltonian

$$\frac{H_{int}}{\hbar} = -g(\sigma^{-}a^{\dagger} + \sigma^{+}a) - \int_{-\infty}^{\infty} dk[c^{\dagger}\bar{G}(k)b_k + \bar{G}^{*}(k)b_k^{\dagger}c] \tag{3.4}$$

where the $\bar{G}(k) = \sqrt{\frac{2c_0\kappa}{\pi}}\sin(kL)$ [128, 93] denotes the coupling element between the microcavity photon and external cavity photon. The interaction between the microcavity and the external cavity is described The propagating wave can be substitute by a standing wave expression of the electric field at $x = 0$. For external cavity mode of wavenumber, k, the sinusoidal term ($\sin(kL)$) describes the wave-vector dependence due to the interference

of the input-output electric field [89, 129, 128].

We discuss interaction Hamiltonian and state vector in the interaction picture, *i.e.*, where and $\left|\Psi^{(I)}\right\rangle = U_0^\dagger(t)\left|\Psi\right\rangle$ where $U_0(t) = \exp\left(-\frac{iH_0t}{\hbar}\right)$ where $H_0 = H_e + H_{field}$. In order to investigate the (slower) dynamics of the internal states, we change into a rotating frame with transition frequency $\frac{(\omega_c+\omega_v)}{2}$. The new Hamiltonian in the rotating-wave frame can be derived from $H_{sys,RWA} = U_0(t)H_{sys}U_0^\dagger(t) - i\hbar U_0^\dagger(t)\frac{\partial}{\partial t}U_0(t)$. We derived the following Hamiltonian as Eq. (1) in the main text,

$$\frac{H_{int}^{(RWA)}}{\hbar} = -g(\sigma^- a^\dagger + \sigma^+ a) - \int d\omega_k (G(k,t)a^\dagger b_k + h.c.) \tag{3.5}$$

Where $G(k,t) = \sqrt{\frac{2c_0\kappa}{\pi}}\sin(kL)\exp[i(\omega_0 - \omega_k)t]$, this term accounts for the coupling element in the rotating-wave approximation. We extend the integral limit of k to negative. This expression describes the tunneling coupling element dependency for photon from the micropillar cavity to the external cavity.

The dynamics of the system is described in the Schrödinger's picture with time dependent wavefunction. In the case of single excitation, the wavefunction is the superposition of $2 + N_k$ states, where N_k is the number of the external cavity photon states.

$$\left|\Psi_I(t)\right\rangle = c_e(t)\left|e,0,0\right\rangle + c_c(t)\left|g,1,0\right\rangle + \int c_k(t)\left|g,0,k\right\rangle \mathrm{d}k \tag{3.6}$$

Here, in the first position in the kets, e (c) denotes QD in the excited (ground) state, in the second position, 0 (1) denotes zero (one) microcavity photon, and in the third position, k denotes one photon in external-cavity state with wave vector k. The state coefficients c_e, c_c, and c_k are the amplitudes for the QD excited state and no microcavity or external cavity photons, the QD ground state and one microcavity photon and no external-cavity photon, and the QD ground state and one external-cavity photon with wave vector k and no

microcavity photons, respectively.

The EOMs of the state vector are obtained by using the Schrödinger's Equation. The interaction Hamiltonian, $H_{int}^{(RWA)}$, in Eq. (3.5) is applied to the wavefunction, $|\Psi_I(t)\rangle$, in Eq. (3.6). The EOMs describing the dynamics for each state vector are shown in Equ. (3.7) $\sim$ (3.9).

$$\frac{\partial c_e}{\partial t} = i\omega_g \, c_c, \tag{3.7}$$

$$\frac{\partial c_c}{\partial t} = i\omega_g \, c_e + i \int_{-\infty}^{\infty} c_k \, G(k,t) \, \mathrm{d}k, \tag{3.8}$$

$$\frac{\partial c_k}{\partial t} = iG^*(k,t) \, c_c. \tag{3.9}$$

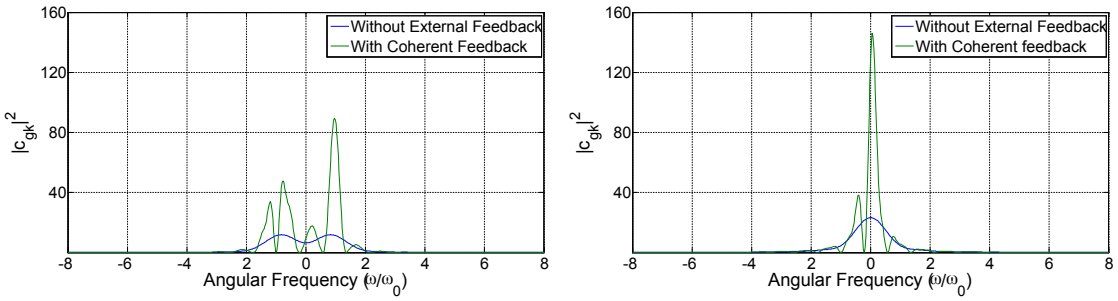

Figure 3.2: Probability of $|c_{gk}|^2$ to find the QD in the ground state and a photon in external-cavity mode k for two cases in (a) strong coupling $4g/\kappa = 20$ and (b) $4g/\kappa = 0.5$.

In Fig. 3.2, we show the power spectrum of the EC photons and compare with the case with no feedback. The peaks in the spectrum shows separation of $\Delta\omega = \frac{2\pi}{\tau_L}$, similar to the separation between stationary solutions, ECMs in a ECSL system.

The coupling to the external cavity (EC) modes can be reduced by integrating Eq. 3.9 formally and inserted into Eq. 3.8 (the above derivation can be found in appendix B). The integration allows non-Markovian process in the following expression:

$$\frac{\partial c_c}{\partial t} = i\omega_g \, c_e(t) - \kappa c_g(t) + \kappa c_g(t-\tau_L)\Theta(t-\tau_L)e^{i\omega_0\tau_L} \tag{3.10}$$

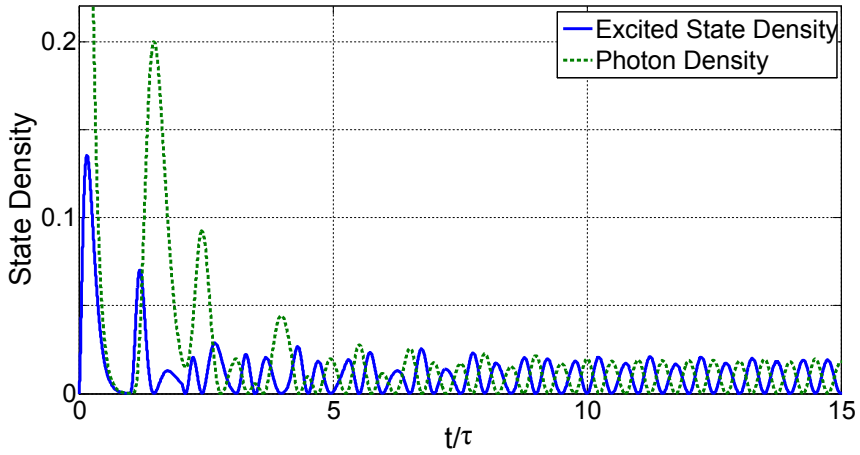

Figure 3.3: Excited state density $|c_e(t)|^2$ (blue) of the two-level system and the photon density $|c_g(t)|^2$ in the microcavity.

The decay and the subsequent oscillation after delayed time, τ_L indicate the physical processes of the delayed feedback contributes at multiple delay time. With the model constructed from Eq. (3.7) $\sim$ (3.9), we are ready to study the coherent quantum feedback mechanism. In the strong-coupling regime (g = 50 μeV, κ = 100 μeV, $4g/\kappa = 2$), the mirror is placed at $L_{\omega_0} = \pi\hbar c_0/g$. The state densities of the excited state $|c_e(t)|^2$ and the state photon $|c_g(t)|^2$ in the microcavity are shown in Fig. 3.3. Coherent quantum feedback induces oscillation patterns and is of agreement with [94].

3.2 Pyragas type feedback in single photon regime

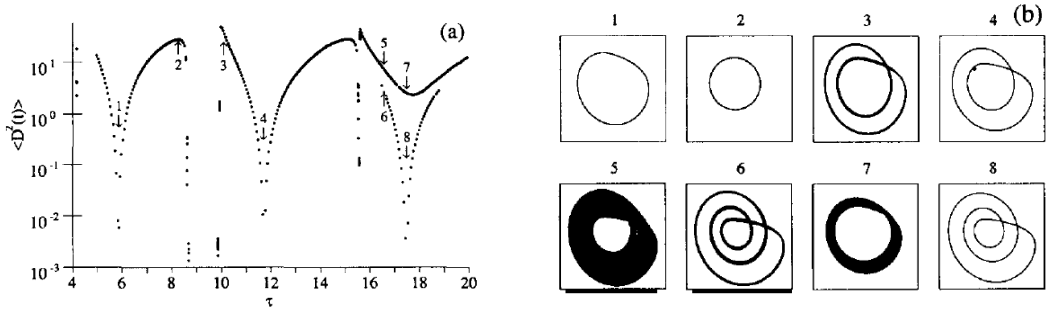

Figure 3.4: (a) Dependence of the dispersion of perturbation on delay time and (b) the x-y phase portraits of the Rossler system in the post-transient regime for some values of the delay time. $K = 0.2$. [3]

Pyragas time-delayed feedback is a control scheme designed to stabilize unstable periodic orbits, which occur naturally in many nonlinear dynamical systems. It has been successfully implemented in a number of applications, including lasers and chemical systems [3]. The classical effect is shown in Fig. 3.4. With coherent feedback, the dynamic variable of the quantum system is the microcavity photon state $c_g(t)$, and the Pyragas type feedback appears in the tunneling Hamiltonian element $G(k,t)$ with the factor $\sin(kL)$ and introduces a delayed-time $\tau_L = 2L/c_0$. We observe the non-intrusive nature of Pyragas type feedback when τ_L is close to the periodic of oscillator, *i.e.*, the Rabi cycle of two level system, $\tau_{Rabi} = 2\pi\hbar/g$. The effect of changing the delay time ($\tau_L = 0.6 \times \tau_{Rabi}, 0.8 \times \tau_{Rabi}, \tau_{Rabi}$) is shown in Fig. 3.5. Here, We define $D_g(t) = c_g(t) - c_g(t-\tau)$ and $D_e(t) = c_e(t) - c_e(t-\tau)$ to characterize the difference of the trajectories at time t and $t-\tau$ in the phase space. The deviation of the value $< D_g^2(t) >$ and $< D_e^2(t) >$ is plotted in Fig. 3.5 (a) as a function of delay time, τ_L/τ_{Rabi}. The trajectories of $c_e(t)$ and $c_g(t)$ corresponding to different external cavity lengths L are compared in Fig. 3.5 (b) and shown in color maps in (c). Each trajectory starts with an excited QD state $c_e(0) = 1$ and is plotted between 0 and $100 \times \tau_{Rabi}$. With the delay time varying from the period (Rabi cycle) of the two level system, the orbit of the oscillator varies with time evolution $L = 0.6 \times \tau_{Rabi}$; and we can observe highly repeated orbits on the phase portraits on the right column when the delay time from the external cavity match the Rabi cycle of the system in Fig. 3.5 (c).

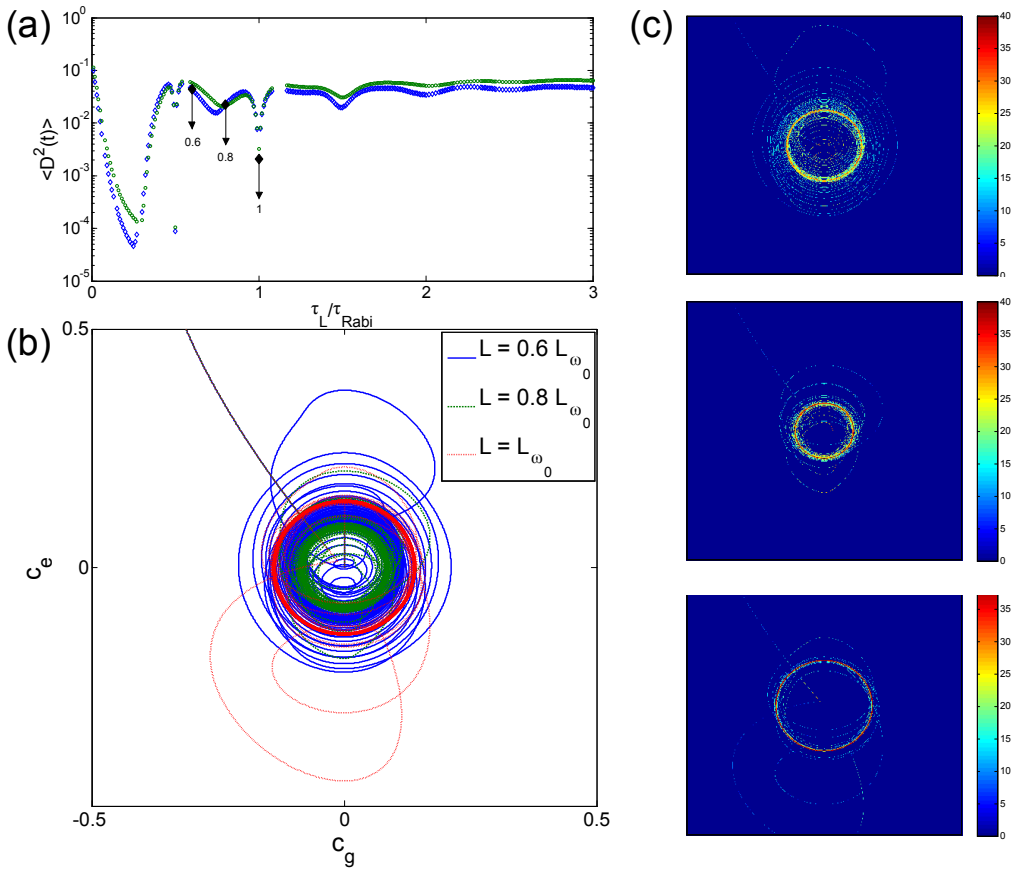

Figure 3.5: (a) Dependence of the dispersion of the state variable, $c_g(t)$ (blue) and $c_e(t)$ (green) on the delay time, τ_L. (b) The phase diagram of two state parameters, c_e versus c_g with different delay time ($\tau_L = 0.6\ \tau_{Rabi}, 0.8\ \tau_{Rabi}, \tau_{Rabi}$). (c) Three diagrams on the right column represent the colormaps of the phase diagram at different delay time. (From top to bottom delay time, $\tau_L = 0.6\ \tau_{Rabi}, 0.8\ \tau_{Rabi}, \tau_{Rabi}$).

3.3 Two-Excitation State with External Cavity

The QD is considered as a two-level system while the electromagnetic field is treated with cQED [93]. The aim of this work is to characterize the complete quantum dynamics of this system in the one and two-excitation subspace. We move on to two-excitation state with the interaction Hamiltonian as in Eqn. (3.5). The two-excitation wavefunction is given as a superposition of five possible states (excluding biexcitonic effects), For two-excitation case:

$$|\Psi\rangle = c_{ec}\,|e,1,0\rangle + \int c_{ek}\,|e,0,k\rangle\,\mathrm{d}k + c_{cc}\,|g,2,0\rangle + \int c_{ck}\,|g,1,k\rangle\,\mathrm{d}k + \int\int c_{kk'}\,|g,0,\{k,k'\}\rangle\,\mathrm{d}k\mathrm{d}k'. \tag{3.11}$$

With the superposition of five possible states, the state coefficients are: c_{ec} stands for QD in excited state and one microcavity photon and no external cavity photon; c_{cc} stands for two photons in the microcavity and the external cavity being in vacuum and the two-level system as well as the radiation field in the waveguide being in the ground state; c_{ck}: one microcavity photon and one external cavity photon with wave vector k; c_{ek} stands for the excited state of the QD and one photon in the external cavity of mode k; $c_{kk'}$: two EC-photon state with wavevectors, k and k', with the QD as well as microcavity being in the ground state.

The two-excitation wavefunction is given as a superposition of five possible states (excluding biexcitonic effects) in Eq. (7). Using the Schrödinger equation with the Hamiltonian in Eq. (4), $i\hbar\frac{\partial}{\partial t}\,|\Psi\rangle = \hat{H}\,|\Psi\rangle$, we obtain the amplitude equations of motion:

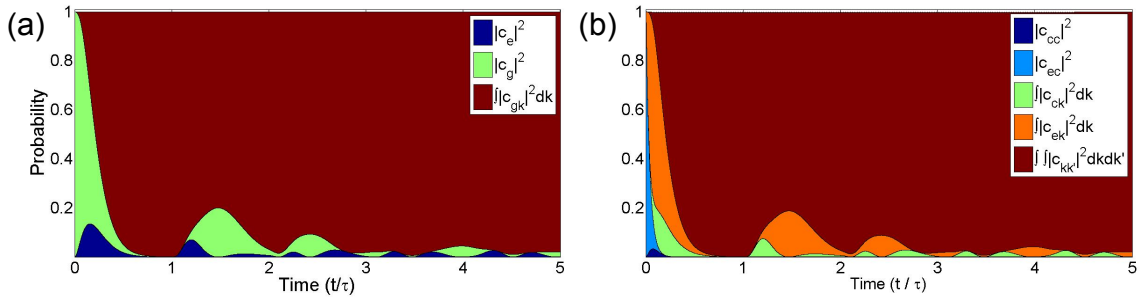

Figure 3.6: Time evolution of the composition of each state probability in the total probability. c_{cc}: the two microcavity-photon state; c_{ec}: QD in excited state; one microcavity photon state; $\int |c_{ck}|^2 \mathrm{d}k$: integral of all one microcavity photon and one EC-photon; $\int |c_{ek}|^2 \mathrm{d}k$: integral of all QD in excited state and one EC-photon; $\int \int |c_{kk'}|^2 \mathrm{d}k\mathrm{d}k'$: integral of all two EC-photon state

$$\frac{\partial c_{ec}}{\partial t} = i\omega_g c_{cc} + i \int c_{ek} G(k,t) \mathrm{d}k \tag{3.12}$$

$$\frac{\partial c_{ek}}{\partial t} = i\omega_g c_{ck} + i c_{ec} G^*(k,t) \tag{3.13}$$

$$\frac{\partial c_{cc}}{\partial t} = i\omega_g c_{ec} + i \int c_{ck} G(k,t) \mathrm{d}k \tag{3.14}$$

$$\frac{\partial c_{ck}}{\partial t} = i\omega_g c_{ek} + i \int c_{kk'} G(k',t) \mathrm{d}k' + i c_{cc} G^*(k,t) \tag{3.15}$$

$$\frac{\partial c_{kk'}}{\partial t} = i c_{ck'} G^*(k,t). \tag{3.16}$$

This set of equations of motion are solved numerically given the initial condition in which the QD is initially excited and there is one photon in the microcavity, i.e., $c_{ec}(0) = 1$ with all other coefficients initially 0.

Fig. 3.6 shows the composition of the squared amplitudes of each state in Eqn. (8) for the initial conditions above. It shows that the state probabilities for one exciton, and one microcavity state c_{ec} (light blue) exchanges most rapidly with one exciton and one external cavity state c_{ek} two external cavity photon between 0 and 0.1τ, due to the other exchange route, two microcavity state (c_{cc}), shows less exchange due to coupling condition. After reaching the peak at $t = 0.07\tau$ at 3.2 %, the two microcavity state, c_{cc} decrease to zero following the general exponential decay as described by Wigner-Weisskopf model in the weak coupling limit. The state probabilities for single microcavity and EC photon,c_{ck}, is

fed by exchanging excitation from the QD to photons, c_{ek} and photon tunneling of a single photon from $c_{kk'}$ (as c_{cc} remains negligible probability).

3.4 Stationary States

For the one-excitation state, we find the stationary-state solutions. Next, we address the stability of these states. In the vicinity of the stationary state, we derive the Jacobian of the state amplitudes. We then perform a stability analysis by analyzing the eigenvalues of the Jacobian matrix as a function of coupling strength and the damping rate. We determined the stability by the dynamical analysis by numerically perturbing the stationary state which agrees with the results obtained directly from the Jacobian of the state amplitudes. The effects of time delay are also studied for various EC lengths L. Subsequently, we find a stationary two-excitation state. We study the dynamics of the state amplitudes in the system for states of various excitation numbers.

We find both one- and two-excitation states are of antisymmetric under exchange parity, representing the MC/emitter and its mirrored-self being in a Dicke's subradiant state [130] aspointed out in Ref. [98, 99] in system with chiral feedback from a single V-level atom. To be more specific, through the parity exchange, the singlet state would appear effectively decoupled from the waveguide, being in a dark state which is subradiant, whereas the triplet state is superradiant as it decay at a twice the cavity damping rate from the microcavity, [98, 99]. The EOMs of each state vector are obtained with the input-output formalism in the Schrödinger picture instead of in the Heisenberg picture as in Ref. [95]. Our choice of performing the simulation in the state-vector based picture is to attain higher time-step resolution of stable/unstable state evolution compare to typical simulation method in Matrix Product State [131].

$$\bar{\Psi}_I(t) = \bar{c}_e(t)\,|e,0,0\rangle + \bar{c}_c(t)\,|g,1,0\rangle + \int_{-\infty}^{\infty} \bar{c}_k(t)\,|g,0,k\rangle\,dk \tag{3.17}$$

where each stationary state parameter being

$$\bar{c}_e(t) = -\alpha_I e^{-i\omega_g t} \tag{3.18}$$

$$\bar{c}_c(t) = \alpha_I e^{-i\omega_g t} \tag{3.19}$$

$$\bar{c}_k(k,t) = \frac{\alpha_I G_0 \sin(kL)}{\omega_k - \omega_g} e^{i(\omega_k - \omega_g)t} \tag{3.20}$$

The amplitudes are the stationary state is can be characterized by a single parameter

$$\alpha_I = |c_c(t)| = |c_e(t)| = \left(2 + \frac{\pi G_0^2 L}{c_0^2}\right)^{-1/2} = (2 + \tau_L \gamma)^{-1/2} \tag{3.21}$$

The stationary state is indicated in Fig. 3.7. The blue arrow shows the state of the QD at a snapshot in time with the time evolution in the RWA shown by the orange arrows where we choosing initial conditions $\bar{c}_e(0) = \alpha_I$, $\bar{c}_c(0) = -\alpha_I$, and $\bar{c}_k(k,0) = \frac{\alpha_I G_0 \sin(kL)}{\omega_k - \omega_g}$. In this case, the EC photons are in a standing wave.

To give a heuristic view of the stationary state, the initial state amplitudes of EC photons of wavenumber, $\bar{c}_k(k,0)$, is an *even* function with respect to the $\omega_k = \omega_0 - \omega_g$ axis in Fig. (3.7) (c) and the coupling element, $G(k,t) = \sqrt{\frac{2c_0\gamma}{\pi}} \sin(kL) \exp[i(\omega_0 - \omega_k)t]$ is an *odd* function. Thus, while L satisfies the commensurability condition, *i.e.,* $\frac{2\pi}{\omega_g} = \frac{2L}{c_0}$, the EC is decoupled from the MC photon and the QD. As this occurs, the QD and the MC photon experience cavity-assisted interaction at the rate of ω_g. When both states have the equal state amplitudes, they preserve the state population over time. Note that this evolution also satisfies the EOMs. In most situations, such as $c_e(0) = 1$, $c_c(0) = 0$, and $c_k(0) = 0$ for all k, the states evolve following the EOMs and they shows periodic oscillations similar to a Rabi oscillations after few τ_L, shown in [97]. In the different initial condition, the wavefunction is no longer stationary since does not the amplitudes of each state varies, the probability of QD in the excited state is plotted the green curve in Fig. 3.8 (a). The evolution of

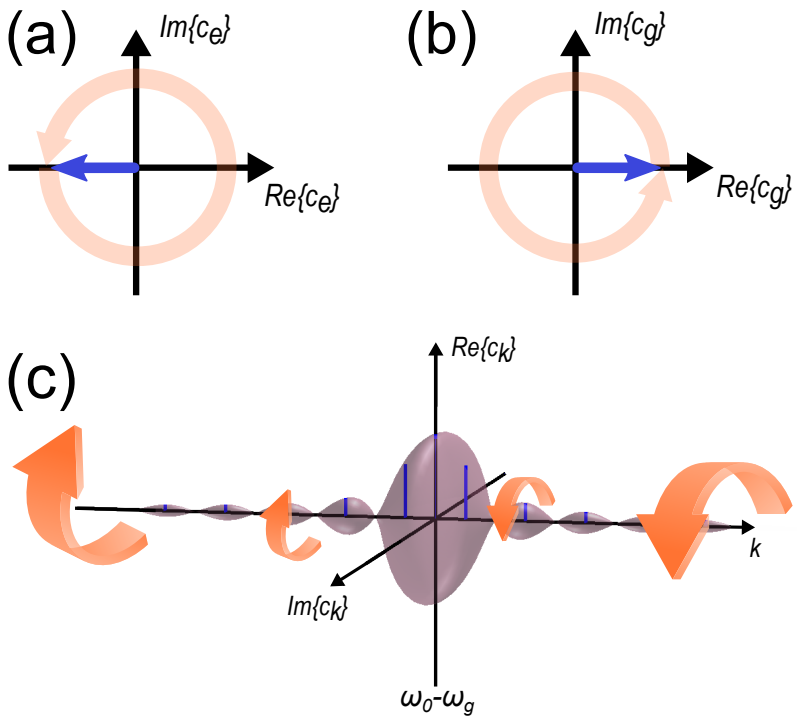

Figure 3.7: Representation of the one-excitation stationary state (a) $\bar{c}_e(t)$, (b) $\bar{c}_c(t)$, and (c) $\bar{c}_k(k,t)$. The blue arrows indicate the initial condition and the orange arrows indicates the time evolution.

the populations are plotted in Fig. 3.8 (a), where evolution of $|c_c|^2$ for two initial states $c_e(0) = 1$, $c_c(0) = 0$, and $c_k(0) = 0$ and $c_{\alpha_I}^-$ is plotted in green while the theoretical and numerical results of the stationary state are plotted in the black and yellow dotted curves, respectively.

The population of the EC photon can be analyzed by the power spectrum of the EC field, it provides useful information given by the following expression as in the input-output formalism [132]. The power spectrum of the EC photon can be derived in wavefunction expression,

$$\begin{aligned} S_0[\omega_k, t] &= \int_0^t e^{i\omega_k t} \langle \Psi_I | d_k^\dagger(t') d_k^\dagger(0) | \Psi_I \rangle \mathrm{d}t' \\ &= \int_0^t e^{i\omega t} c_k^\dagger(t') c_k(0) dt' \end{aligned} \tag{3.28}$$

In addition, we find the stationary solution for two-excitation state in the system, *i.e.*,

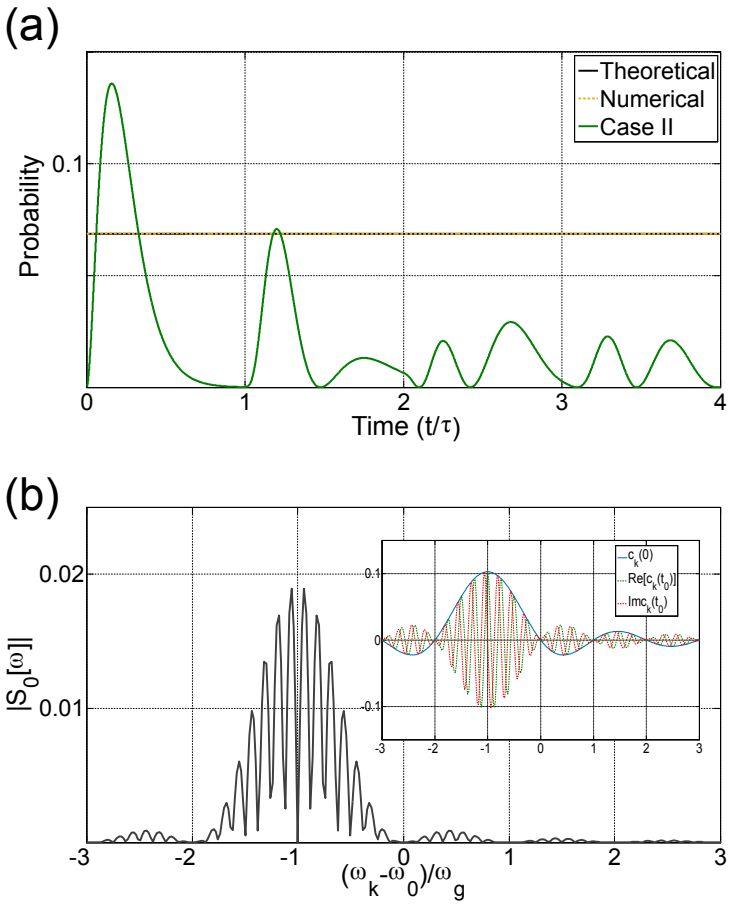

Figure 3.8: Time evolution of the various populations for various initial conditions. (a) The evolution of QD initiate in the excited state (green); and by choosing different initial condition, the expected stationary state of amplitude α_I^2 (black) and the simulated stationary state (yellow dotted curve). (b) The power spectrum of the EC photon in Eq. (9) while the inset shows the amplitude c_k associated with the EC photon at $t = 0$ (blue) with $c_k(t_0)$ for its real (green) and imaginary (red) part when $t_0 = 4\tau_g$ as a function of k.

the stationary solution for two-excitation state is written

$$\bar{\Psi}_{II} = \tilde{c}_{ec}\,|e,1,0\rangle + \int \tilde{c}_{ek}\,|e,0,k\rangle\,\mathrm{d}k + \tilde{c}_{cc}\,|g,2,0\rangle + \int \tilde{c}_{ck}\,|g,1,k\rangle\,\mathrm{d}k + \int\int \tilde{c}_{kk'}\,|g,0,\{k,k'\}\rangle\,\mathrm{d}k\mathrm{d}k'. \tag{3.22}$$

where each stationary state parameter being

$$\bar{c}_{ec}(t) = -\alpha_{II} e^{-i\omega_g t} \tag{3.23}$$

$$\bar{c}_{cc}(t) = \alpha_{II} e^{-i\omega_g t} \tag{3.24}$$

$$\bar{c}_{ck}(k,t) = \frac{\alpha_{II} G_0 \sin(kL)}{\omega_k - \omega_g} e^{i(\omega_k - \omega_g)t} \tag{3.25}$$

$$\bar{c}_{ek}(k,t) = -\frac{\alpha_{II} G_0 \sin(kL)}{\omega_k - \omega_g} e^{i(\omega_k - \omega_g)t} \tag{3.25}$$

$$\bar{c}_{kk'}(k,k',t) = \alpha_{II}\ G_0^2 \frac{\sin(kL)}{\omega_k - \omega_0} \frac{\sin(k'L)}{\omega_k + \omega_{k'} + \omega_g} e^{i(\omega_k + \omega_{k'} + \omega_g)t} \tag{3.27}$$

The state amplitudes are determined by a different parameter

$$\alpha_{II} = |c_{ec}| = (2 + \frac{2\pi G_0^2 L}{c_0^2} + \frac{G_0^4 L^2 \pi^2}{c_0^4})^{-1/2} = (2 + 2\tau_L \kappa + \tau_L^2 \kappa^2)^{-1/2} \tag{3.28}$$

From the solution of the stationary state for one excitation case (Eq. (6) $\sim$ (8)) and two-excitation case (Eq. (13) $\sim$ (17)), we expect there should be a stationary state solution in higher excitation number state in a system consisted of QD, MC and couple to an EC, while the biexciton and higher-exciton electric state are decoupled to the MC mode. That is, in the case with l excitation state, the wavefunction is a superposition of $2l+1$ states. These $2l+1$ states are: for integer, m ($l < m \leq 0$), m EC photon and two states (one with excited QD and $l-m-1$ MC photon and one with QD being in ground state and $l-m$ MC photons); and one state with m EC photons when $m = l$. One can apply the Schrödinger's equation and obtain $2l+1$ EOMs (where it requires N_k EOMs to describe the interaction of a MC photon with a EC photon). Without being able to give a rigorous proof, we can apply the stationary constraint and normalization condition in order (expected) to obtain stationary state in such condition. **Predictively**, in the expected l-excitation stationary state, the amplitude parameter is $\alpha_l = [2 + 2\tau_L\kappa + \ldots 2(\tau_L\kappa)^{l-1} + (\tau_L\kappa)^l]^{-1/2}$. One also **anticipate** the energy eigenvalue of the interaction Hamiltonian, H_{int}, being

Stat. State	H_e	$H_{field,\mu}$	$H_{field,EC}$	H_{int}	E_{tot}
$\bar{\Psi}_I$	$-\frac{\hbar\omega_0}{2}\frac{\tau_L\kappa}{2+\tau_L\kappa}$	$\frac{\hbar\omega_0}{2+\tau_L\kappa}$	$\frac{\hbar(\omega_0-\omega_g)\tau_L\kappa}{2+\tau_L\kappa}$	$-\frac{2\hbar\omega_g}{2+\tau_L\kappa}$	$\frac{\hbar\omega_0}{2}-\hbar\omega_g$
$\bar{\Psi}_{II}$	$-\frac{\hbar\omega_0}{2}\frac{\tau_L^2\kappa^2}{2+2\tau_L\kappa+\tau_L^2\kappa^2}$	$\frac{\hbar\omega_0(3+\tau_L\kappa)}{2+2\tau_L\kappa+\tau_L^2\kappa^2}$	$\frac{\hbar\omega_0(2\tau_L\kappa+2\tau_L^2\kappa^2)-\hbar\omega_g\tau_L^2\kappa^2}{2+2\tau_L\kappa+\tau_L^2\kappa^2}$	$-\frac{\hbar\omega_g(2+2\tau_L\kappa)}{2+2\tau_L\kappa+\tau_L^2\kappa^2}$	$\frac{3\hbar\omega_0}{2}-\hbar\omega_g$
$\bar{\Psi}_l$	$-\frac{\hbar\omega_0\alpha_l^2}{2}(\tau_L\kappa)^l$	$\hbar\omega_0\alpha_l^2[l+(l-2)\sum_{i=1}^{l-1}(\tau_L\kappa)^i]$	$\hbar\alpha_l^2\{\omega_0[2\sum_{i=1}^{l}(\tau_L\kappa)^i]-\omega_g(\tau_L\kappa)^l\}$	$-2\hbar\omega_g\alpha_l^2\sum_{i=0}^{l-1}(\tau_L\kappa)^i$	$\frac{(2l-1)\hbar\omega_0}{2}-\hbar\omega_g$

Table 3.1: Energy eigenvalues of stationary wavefunctions calculated in one- and two-excitation state. We anticipate (without rigorous proof) the energy eigenvalue of the stationary state with l excitation number.

$$E_{int} = \frac{\hbar\omega_g[2+2\tau_L\kappa+\ldots 2(\tau_L\kappa)^{l-1}]}{2+2\tau_L\kappa+\ldots 2(\tau_L\kappa)^{l-1}+(\tau_L\kappa)^l} \tag{3.29}$$

In addition, the energy eigenvalues are also calculated for different Hamiltonian in the system listed in Table I.

3.5 Stability analysis

We study the dynamics in the vicinity of the stationary state. Classically, one typically analyzes the stability of a laser system by studying the properties of its Jacobian matrix [33]. The Jacobian is defined as the matrix of all first-order partial derivatives with respect to the each variable (in this case, the perturbed state amplitudes) evaluated at the equilibrium point.

$$\frac{\partial}{\partial t}\delta c_i(t) = \boldsymbol{J_\delta}\delta c_i(t) \tag{3.30}$$

The eigenvalues of the Jacobian matrix determine linear stability properties of the equilibrium. The perturbed states along the i vector from the stationary state will evolve according to $\delta c_i(t) = \delta c_i(0)e^{\lambda_i t}$ where $\delta c_i(t)$ is the small perturbation along the i vector from the stationary state, $\bar{c}_{\alpha_I}$ at $t = 0$. Given the eigenvalues, possible cases for the steady state are are attractors, repellors, or saddle points corresponding to all negative, all positive, or some positive and some negative eigenvalue, respectively. The dynamics can be analyzed by the nature of the equilibrium state, in this case, the stationary state, $\bar{\Psi}(t)$.

The interaction of the perturbed state amplitudes can be derived using linearized EOMs near the stationary state, and the Jacobian matrix of rank $(2+N)$ is derived following the small-signal model, where N being the number of EC photon states, c_k, used in the simulation.

Next, we discuss the stability regarding applying a small perturbation onto the magnitude of the stationary state. We start with small perturbation $\delta c_i(t)$ similar to the procedure well known as small-signal model in electronics and search for the Jacobian such that $\frac{\partial}{\partial t}\delta c_i(t) = \boldsymbol{J_\delta}\delta c_i(t)$. Hence, we start with the stationary state $\bar{c}$ with an additional linear term

$$\tilde{c}_e(t) = \bar{c}_e(t) + \delta c_e(t)\exp\Big[i\tilde{\theta}_e(t)\Big] \tag{3.31}$$

$$\tilde{c}_c(t) = \bar{c}_c(t) + \delta c_c(t)\exp\Big[i\tilde{\theta}_c(t)\Big] \tag{3.32}$$

$$\tilde{c}_k(t) = \bar{c}_k(t) + \delta c_k(t)\exp\Big[i\tilde{\theta}_k(t)\Big] \tag{3.33}$$

To perform stability analysis with bifurcation theory, one can determine the *Jacobian* $\boldsymbol{J}$ ($\frac{\partial x}{\partial t} = \boldsymbol{J}\boldsymbol{x}$) and calculate the eigenvalues correspond to the small variation along each axis. With the stationary condition given above ($\frac{\partial}{\partial t}\boldsymbol{c}^{-}_{\boldsymbol{\alpha_I}} = \frac{\left|c^{-}_{\boldsymbol{\alpha_I}}\right|}{\partial t}\cdot e^{i\theta_i(t)} + i\frac{\theta_i(t)}{\partial t}\cdot|\boldsymbol{c}^{-}_{\boldsymbol{\alpha_I}}|e^{i\theta_i(t)} = i\frac{\theta_i(t)}{\partial t}\cdot\boldsymbol{c}^{-}_{\boldsymbol{\alpha_I}}$, $i = e,\ c$, and k), we have the *Jacobian* of the stationary state,

$$\begin{aligned}\boldsymbol{J_\delta} &= \begin{bmatrix} -i\omega_0 & i\omega_g & 0 & 0 & ... & 0 \\ i\omega_g & -i\omega_0 & iG_0\sin(k_1L) & iG_0\sin(k_2L) & ... & iG_0\sin(k_NL) \\ 0 & iG_0\sin(k_1L) & -i\omega_{k_1} & 0 & ... & 0 \\ \vdots & iG_0\sin(k_2L) & 0 & -i\omega_{k_2} & \ddots & \vdots \\ \vdots & \vdots & \vdots & \ddots & \ddots & 0 \\ 0 & iG_0\sin(k_NL) & 0 & ... & 0 & -i\omega_{k_N} \end{bmatrix} \\ &= i\frac{c}{L}\begin{bmatrix} -\tilde{k}_0 & \tilde{k}_g & 0 & 0 & ... & 0 \\ \tilde{k}_g & -\tilde{k}_0 & \alpha\sin\big(\tilde{k}_1\big) & \alpha\sin\big(\tilde{k}_2\big) & ... & \alpha\sin\big(\tilde{k}_N\big) \\ 0 & \alpha\sin\big(\tilde{k}_1\big) & -\tilde{k}_1 & 0 & ... & 0 \\ \vdots & \alpha\sin\big(\tilde{k}_2\big) & 0 & -\tilde{k}_2 & \ddots & \vdots \\ \vdots & \vdots & \vdots & \ddots & \ddots & 0 \\ 0 & \alpha\sin\big(\tilde{k}_N\big) & 0 & ... & 0 & -\tilde{k}_N \end{bmatrix} = i\frac{c}{L}\tilde{\boldsymbol{J}}_{\boldsymbol{\delta}}\end{aligned} \tag{3.34}$$

where $\alpha = \frac{G_0L}{c_0}$, and $\tilde{k}_i = \frac{\omega_{k_i}L}{c_0}$.

The eigenvalues of the Jacobian matrix determine linear stability properties of the

equilibrium. The perturbed states along the i vector from the stationary state will evolve according to $\delta c_i(t) = \delta c_i(0)e^{\lambda_i t}$ where $\delta c_i(t)$ is the small perturbation along the i vector from the stationary state, $\bar{c}_{\alpha_I}$ at $t = 0$. Given the eigenvalues, possible cases for the steady state are are attractors, repellors, or saddle points corresponding to all negative, all positive, or some positive and some negative eigenvalue, respectively. The dynamics can be analyzed by the nature of the equilibrium state, in this case, the stationary state, $\bar{\Psi}(t)$.

We proceed to find the eigenvalues, λ, of $\boldsymbol{J_\delta}$ and discuss the properties of these eigenvalues. One simple step is finding the set of equivalent eigenvalues $\tilde{\lambda}$ of $\tilde{\boldsymbol{J_\delta}}$ ($\lambda = i\frac{c_0}{L}\tilde{\lambda}$), and proceed to stability analysis of the station state. To find the eigenvalues for such large matrix, $\tilde{\boldsymbol{J_\delta}} - \tilde{\lambda} \times \mathrm{I}_{(2+\mathrm{N})}$ where $\mathrm{I}_{(2+\mathrm{N})}$ is the identity matrix of $N + 2 \times N + 2$, and $N = \frac{R_f}{\Delta_f}$ is the total number of the sampled frequencies. The interaction of the perturbed state amplitudes can be derived using linearized EOMs near the stationary state, and the Jacobian matrix of rank $(2 + N)$ is derived following the small-signal model, where N being the number of EC photon states, c_k, used in the simulation.

$$\det(\tilde{\boldsymbol{J}}_{\boldsymbol{\delta}} - \tilde{\lambda} \times \mathrm{I}_{(2+\mathrm{N})}) = \begin{bmatrix} -\tilde{k}_0-\tilde{\lambda} & \tilde{k}_g & 0 & 0 & ... & 0 \\ \tilde{k}_g & -\tilde{k}_0-\tilde{\lambda} & \alpha\sin(\tilde{k}_1) & \alpha\sin(\tilde{k}_2) & ... & \alpha\sin(\tilde{k}_N) \\ 0 & \alpha\sin(\tilde{k}_1) & -\tilde{k}_1-\tilde{\lambda} & 0 & ... & 0 \\ \vdots & \alpha\sin(\tilde{k}_2) & 0 & -\tilde{k}_2-\tilde{\lambda} & \ddots & \vdots \\ \vdots & \vdots & \vdots & \ddots & \ddots & 0 \\ 0 & \alpha\sin(\tilde{k}_N) & 0 & ... & 0 & -\tilde{k}_N-\tilde{\lambda} \end{bmatrix}$$

$$= (-\tilde{k}_0 - \tilde{\lambda})\det(\begin{bmatrix} -\tilde{k}_0-\tilde{\lambda} & \alpha\sin(\tilde{k}_1) & \alpha\sin(\tilde{k}_2) & ... & \alpha\sin(\tilde{k}_N) \\ \alpha\sin(\tilde{k}_1) & -\tilde{k}_1-\tilde{\lambda} & 0 & ... & 0 \\ \alpha\sin(\tilde{k}_2) & 0 & -\tilde{k}_2-\tilde{\lambda} & \ddots & \vdots \\ \vdots & \vdots & \ddots & \ddots & 0 \\ \alpha\sin(\tilde{k}_N) & 0 & ... & 0 & -\tilde{k}_N-\tilde{\lambda} \end{bmatrix}) - \tilde{k}_g \times \det(\begin{bmatrix} \tilde{k}_g & \alpha\sin(\tilde{k}_1) & \alpha\sin(\tilde{k}_2) & ... & \alpha\sin(\tilde{k}_N) \\ 0 & -\tilde{k}_1-\tilde{\lambda} & 0 & ... & 0 \\ 0 & 0 & -\tilde{k}_2-\tilde{\lambda} & \ddots & \vdots \\ \vdots & \vdots & \ddots & \ddots & 0 \\ 0 & 0 & ... & 0 & -\tilde{k}_N-\tilde{\lambda} \end{bmatrix})$$

$$= (-\tilde{k}_0 - \tilde{\lambda})^2\det(\begin{bmatrix} -\tilde{k}_1-\tilde{\lambda} & 0 & ... & 0 \\ 0 & -\tilde{k}_2-\tilde{\lambda} & \ddots & \vdots \\ \vdots & \ddots & \ddots & 0 \\ 0 & ... & 0 & -\tilde{k}_N-\tilde{\lambda} \end{bmatrix}) - (-\tilde{k}_0 - \tilde{\lambda})\{\alpha\sin\Big(\tilde{k}_1\Big)\det(\begin{bmatrix} \alpha\sin(\tilde{k}_1) & 0 & ... & 0 \\ \alpha\sin(\tilde{k}_2) & -\tilde{k}_2-\tilde{\lambda} & \ddots & \vdots \\ \vdots & \ddots & \ddots & 0 \\ \alpha\sin(\tilde{k}_N) & ... & 0 & -\tilde{k}_N-\tilde{\lambda} \end{bmatrix})$$

$$-\alpha\sin\Big(\tilde{k}_2\Big)\det(\begin{bmatrix} \alpha\sin(\tilde{k}_1) & -\tilde{k}_1-\tilde{\lambda} & 0 & ... & 0 \\ \alpha\sin(\tilde{k}_2) & 0 & 0 & \ddots & \vdots \\ \vdots & 0 & -\tilde{k}_3-\tilde{\lambda} & \ddots & 0 \\ \vdots & \vdots & \ddots & \ddots & 0 \\ \alpha\sin(\tilde{k}_N) & 0 & ... & 0 & -\tilde{k}_N-\tilde{\lambda} \end{bmatrix}) + \ldots + \alpha\sin\Big(\tilde{k}_N\Big)\left[\ddots\right]\}$$

$$-\tilde{k}_g^2\ \det(\begin{bmatrix} -\tilde{k}_1-\tilde{\lambda} & 0 & ... & 0 \\ 0 & -\tilde{k}_2-\tilde{\lambda} & \ddots & \vdots \\ \vdots & \ddots & \ddots & 0 \\ 0 & ... & 0 & -\tilde{k}_N-\tilde{\lambda} \end{bmatrix})$$

(3.35)

By applying the triangular property and swapping property of the matrix, we found the *function of determinant* on the basis of the matrix minor. it is easy to verify that the *function of determinant* of $\tilde{\boldsymbol{J}}_{\boldsymbol{\delta}} - \tilde{\lambda} \times \mathrm{I}_{(2+\mathrm{N})}$ in Eq. (3.35) can be written as

$$\det(\bar{\boldsymbol{J}}_{\boldsymbol{\delta}} - \tilde{\lambda} \times \mathrm{I}_{(2+N)}) = \{(\tilde{k}_0 + \tilde{\lambda})^2 - \alpha^2(\tilde{k}_0 + \tilde{\lambda})[\sum_{i=1}^{N} \frac{\sin^2(\tilde{k}_i)}{\tilde{k}_i + \tilde{\lambda}}] - \tilde{k}_g^2\}[\prod_{i=1}^{N}(-\tilde{k}_i - \tilde{\lambda})]$$

(3.36)

From Eq. (3.36), we expect to find the $N+2$ solutions satisfying $\tilde{\boldsymbol{J}}_{\boldsymbol{\delta}} - \tilde{\lambda} \times \mathrm{I}_{(2+\mathrm{N})} = 0$,

where these solutions being the eigenvalues of the *Jacobian*, $\tilde{\boldsymbol{J}}_{\boldsymbol{\delta}}$. Among the solutions of $\tilde{\lambda}_i$, we have N real eigenvalues for $\tilde{\lambda}_i = -\tilde{k}_i$ ($\lambda_i = i\frac{c}{L}\tilde{\lambda}_i$ being purely imaginary). The last two *complex* solutions, $\tilde{\lambda} = p + iq$ (p, $q \in R$), come from solving the equation in the first bracket in Eq. (3.36) being zero.

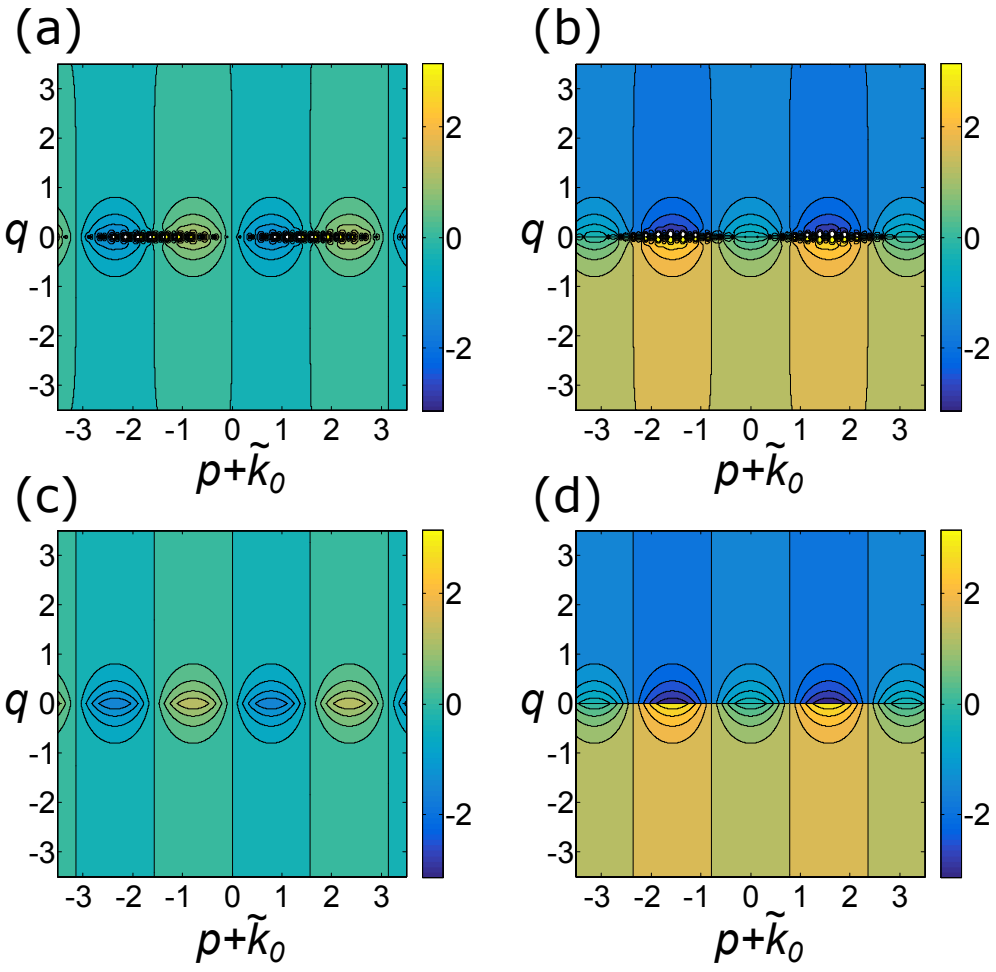

Figure 3.9: The comparison of the numerical summand in Eq. (3.36) and the analytical expression in Eq. (3.30) as a function of p and q. The real part (a) and the imaginary part (b) of the summand is used to compare with the real part (c) and the imaginary part (d) of analytical result in Eq. (3.37).

We proceed to evaluate this function. The summand in Eq. (3.36) can be evaluated under two conditions: $|p| > |q|$.

$$\sum_{i=1}^{N} \frac{\sin^2(\tilde{k}_i)}{\tilde{k}_i + \tilde{\lambda}} = \frac{\pi}{2L}\{-\sin(2p)e^{-2|q|} + i[e^{-2|q|}\cos(2p) - 1]\ \mathrm{sgn}(q)\} \tag{3.37}$$

where sgn is the *sign function*: $\mathrm{sgn}(q) = \frac{q}{|q|}$. The summand is a complex function of p and q, the real part and the imaginary part are evaluated numerically as a function of p and q shown in Fig. 3.9 (a) and (b), respectively. The analytical expression in Eq. (3.37) is plotted in Fig. 3.9 to verify Eq. (3.37), we show the real part and the imaginary part of in Fig. 3.9 (c) and (d), respectively.

We insert Eq. (3.37) into Eq. (3.36) and solve for both real and imaginary part of *function of determinant* being zeros, and $\frac{\alpha^2\pi}{2L} = (\frac{G_0 L}{c_0})^2(\frac{\pi}{2L}) = \frac{\kappa\tau_L}{2}$. We obtain the following relationships.

Real :

$$(\tilde{k}_0 + p)^2 - q^2 - \tilde{k}_g^2 + \frac{\kappa\tau_L}{2}\{(\tilde{k}_0 + p)\sin(2p)e^{-2|q|} + q\ [e^{-2|q|}\cos(2p) - 1]\mathrm{sgn}(q)\} = 0 \tag{3.38}$$

Imaginary :

$$2(\tilde{k}_0 + p)\ q - \frac{\kappa\tau_L}{2}\{(\tilde{k}_0 + p)[e^{-2|q|}\cos(2p) - 1]\mathrm{sgn}(q) - q\sin(2p)e^{-2|q|}\} = 0 \tag{3.39}$$

We plot the solutions of the above equation on a $p - q$ place shown in Fig. 3.10, where the solution of the real part (Eq. 3.38) are shown in the first column and the solutions of the imaginary part (Eq. 3.39) in the second column. From top to bottom, the solution for Eq. 3.38 and 3.39 are plotted for different feedback phase (from top to bottom, $\Delta\phi = 0, \pi, \frac{\pi}{2}, and \frac{3\pi}{2}$). The solutions of the intersection, are the eigenvalues of the perturbed system, are shown in Fig. 3.11.

In the above-mentioned scenarios, we find the eigenvalues being purely imaginary. Imaginary eigenvalues indicate oscillatory dynamics upon perturbation about the stationary state, i.e., this indicates stability of periodic trajectories. Notably, since the perturbation on

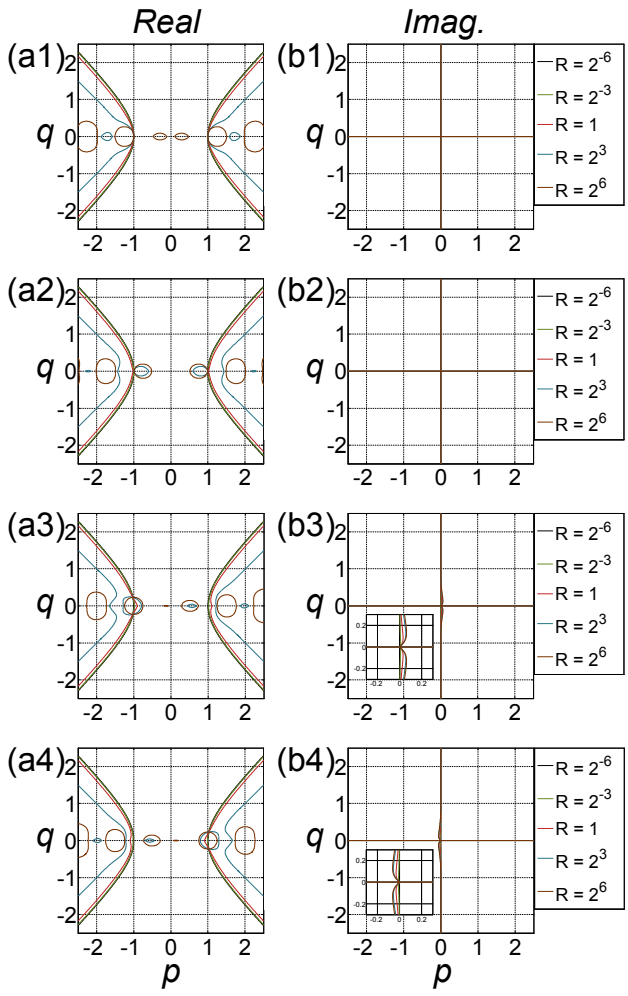

Figure 3.10: The eigenvalues $\tilde{\lambda} = p + iq$ are plotted on the p-q plane for different ratio of $R = \frac{4\kappa}{g}$, where κ and g are the cavity damping rate, and the coupling strength, respectively. The horizontal p axis is offset by $-\tilde{k_0}$

the stationary state evolves following the relationship $\delta c_c(t) = \delta c_c(0) \exp(\lambda)t$, we expect to observe oscillation in both probability (the MC photon state and the excited QD state) oscillates $|c_c(t)|^2 = \alpha_I^2 + \alpha_I \delta c_c(0) \cos \omega_{\text{osc}} t + |\delta c_c(0)|^2$, where the only oscillating frequency appear in the second term as $\omega_{\text{osc}} = \omega_g + \omega_0 + \lambda$. By solving the analytical expression of eigenvalues, we find the frequency ω_{osc} is a function of experimental parameters, κ, ω_g, and time delay τ_L (or the feedback phase of the reflected photon $\Delta\phi$). We start with the analysis of eigenvalues with different feedback phase.

Constructive interference: $\Delta\phi = 0$. The external-cavity round-trip distance is a half-multiple of the photon wavelength, $2L = (m + 1/2)\Lambda_0$. The reflected photon is assumed to undergo π phase change from an ideal mirror ($rr^* = 1$, where r being the complex reflection coefficient). As a result, we find the excessive solutions for eigenvalues appears. In the following discussion, we introduce a value, $\bar{R}(n, \Delta\phi)$, indicates the ratio of R where excessive solutions appears, where n being the ratio of EC round-trip time τ_L and τ_g, and $\Delta\phi$ being the feedback phase. The $\bar{R}(n, \Delta\phi)$ value is indicated by the red-dotted line in Fig. 3.11 and Fig. 3.14. In the case of constructive interference, we find six (four excessive) solutions at $\bar{R}(1, 0) = 0.156$, indicating a possible bifurcating point in the strong-coupling regime. In addition, the frequency separation between the excessive solutions at weak coupling regime e.g. $R = 64$, are $\delta f_{\text{osc}} = 1/(2\tau_L)$. The expected oscillation frequency as a function of R is shown in Fig. 3.11 (a).

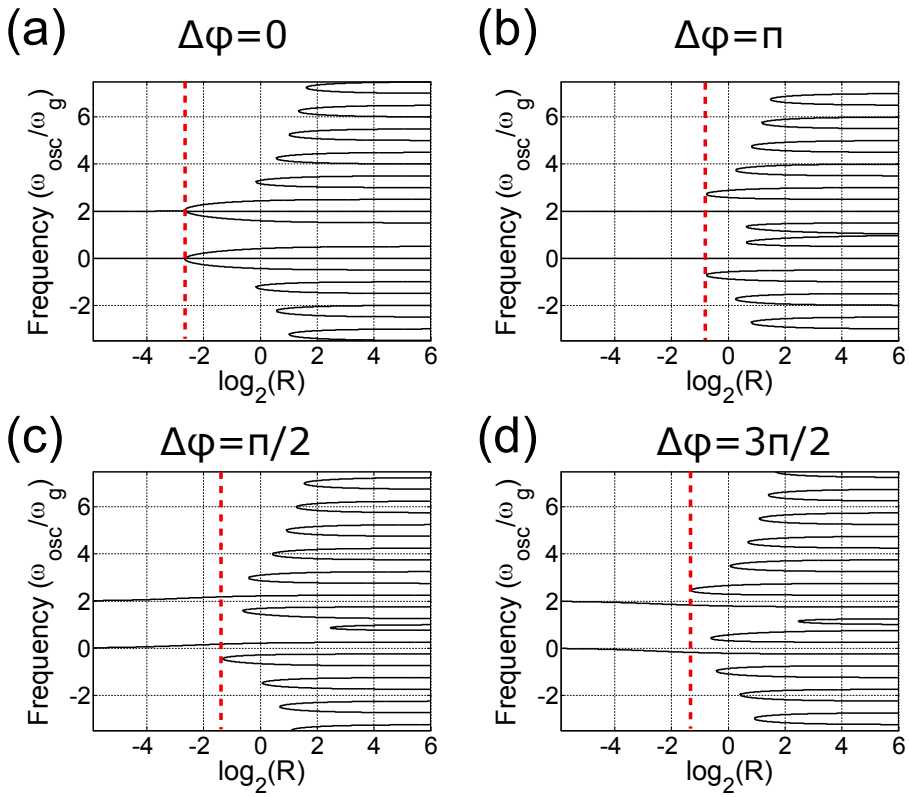

Figure 3.11: The oscillating frequency ω_{osc} of the probability $|c_c(t)|^2$ as function of the R for different feedback phase.

Destructive interference: $\Delta\phi = \pi$. The external-cavity round-trip distance is multiple integer of the photon wavelength, $2L = m\Lambda_0$. The reflected photon interferes destructively with the emitting photon. We plot the expected oscillating frequency as a function of value R in Fig. 3.11(b). The excessive solutions appear at $\bar{R}(1,\pi) = 0.62$. The excessive solution indicate the probability $|c_c|^2$ will oscillate at higher frequencies $2.7 \times \omega_g$. Note that the excessive solutions appear pairwise and the difference approaches $\delta f_{osc} = 1/(2\tau_L)$.

Partial interference: $\Delta\phi \neq 0 \neq \pi$. in this case, the reflected photon partially interferes with the emitted photon. The oscillation frequency of the MC photon state probability, ω_{osc} depends also on the phase difference of the reflected photon. We plot the MC oscillation frequencies ω_{osc} $\Delta\phi = \pi/2$ and $3\pi/2$ in Fig. 3.14 (c) and (d), respectively. Notice the slight decrease of ω_{osc} for $\Delta\phi = \pi/2$ and the opposite effect for $\Delta\phi = 3\pi/2$.

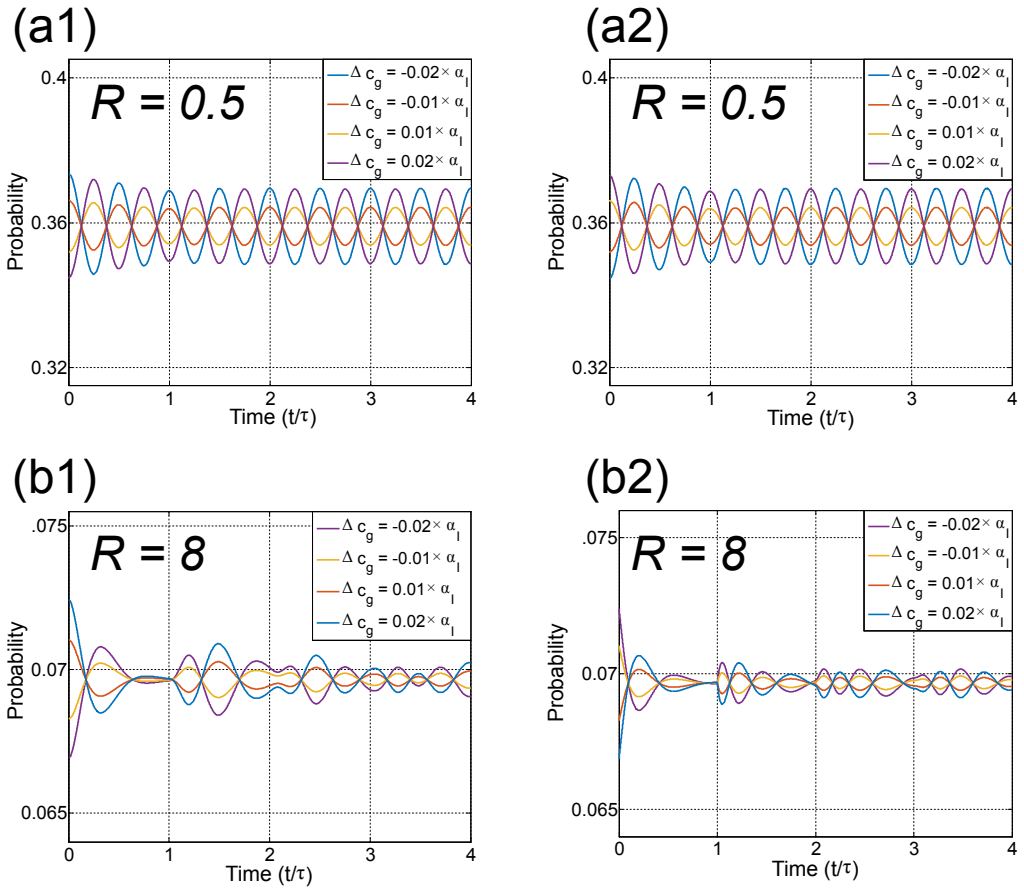

Figure 3.12: The evolution of probability, $|c_e(t)|^2$ and $|c_c(t)|^2$, of perturbed states with various values of R.

We present numerical simulations of the dynamics in the vicinity of the candidate stable state to confirm the foregoing stability analysis. Here, we perturb the stationary state with small signals and track the dynamics of the probabilities. The dynamics are tracked upon adding perturbations $\delta_{c,i}$ to c_e and c_c with respect to the stationary state $\bar{\Psi}(t)$ in Eq. (3.18) $\sim$ (3.20). We perturb the MC photon state *amplitudes* at $t=0$ $\bar{c}_c(0)$ in the vicinity of our candidate stable state.

The amplitude differences are $\delta c_c = [\pm\ 0.01, \pm\ 0.02]\alpha_I$ while the amplitude of QD state $c_e(0)$ is perturbed such that $|\bar{c}_e + \delta c_e|^2 + |\bar{c}_c + \delta c_c|^2 = |\bar{c}_e|^2 + |\bar{c}_c|^2$. The effect on the stability is demonstrated by plotting the probability at two values of R ($R=0.5$ and $R=8$). The probabilities of the excited QD state, $|c_e(t)|^2$ are plotted in Fig. 3.12(a1) and (b1) and MC photon state $|c_c(t)|^2$ in Fig. 3.12(a2) and (b2) for $R = 0.5$, and 8, respectively. The phase difference for both cases in Fig. 3.12 is $\Delta\phi=0$.

In Fig. 3.12, the perturbed portion of the probability (from the stationary state probability) evolve in a damped oscillation between $t = 0$ to τ_L with damping rate 2κ. After the time delay, both probabilities, $|c_e|^2$ and $|c_g|$ start to oscillate. The probabilities of both c_e and c_c states at lower $R = 0.5$ oscillate periodically at frequency $2\omega_g$ as shown in Fig. 3.12(a1) and (a2). By comparison, the dynamics of both probabilities at $R = 8$ show less consistent oscillation, indicating richer dynamics involving multiple frequencies.

We next explore the stability dependence on the EC length L. We find the stationary states only exists when time delay is an integer multiple of $\tau_g = 2\pi/\omega_g$. Here, we study the oscillating frequency of the probabilities ω_{osc} with $\tau_L = n2\pi/\omega_g$ ($n = 1, 2, 3$, and 4) where $\Delta\phi=0$. We plot the solutions of the above equation on a $p - q$ place shown in Fig. 3.15, where the solution of the real part (Eq. 3.38) are shown in the first column and the solutions of the imaginary part (Eq. 3.39) in the second column. From top to bottom, the solution for Eq. 3.38 and 3.39 are plotted for delayed time (from top to bottom, $n = 1, 2, 3$, and 4). The solutions of the intersection, are the eigenvalues of the perturbed system, are shown in Fig. 3.14.

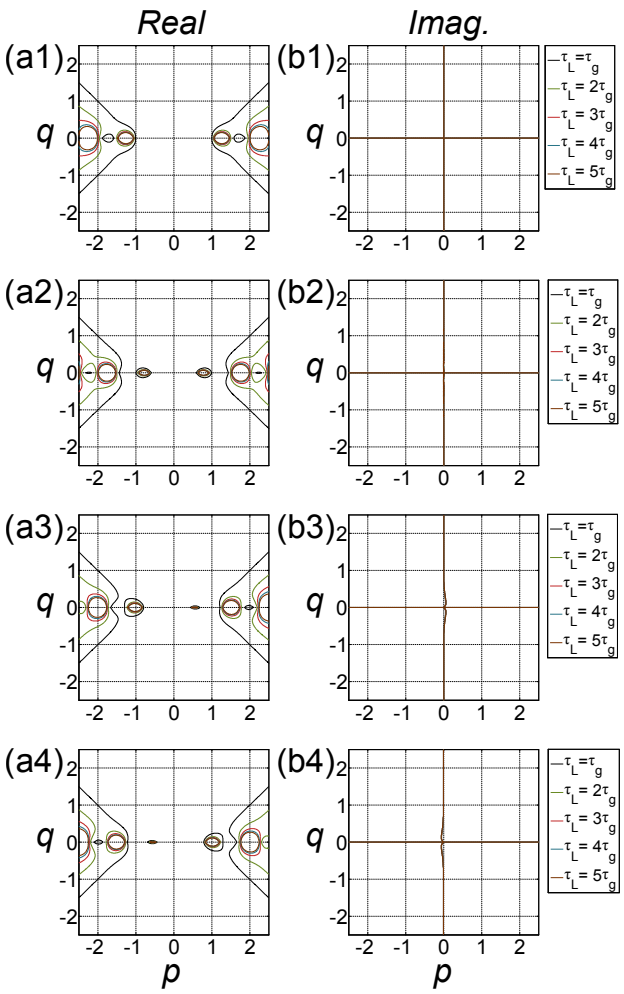

Figure 3.13: The solution satisfying Eq. (C6) and (C7) where the solution are eigenvalues $\tilde{\lambda} = p + iq$ are plotted on the p-q plane for different delayed time, τ_L for fixed ratio of $R = \frac{4\kappa}{g} = 8$. The horizontal p axis is offset by $-\tilde{k_0}$

We find the ratio $\bar{R}$, where the excessive solutions occurs decreases as EC increases shown by various dotted red line in Fig. 3.14. That is, $\bar{R}(1,0) = 0.15$, $\bar{R}(2,0) = 0.08$, $\bar{R}(3,0) = 0.053$, and $\bar{R}(4,0) = 0.039$. The frequency difference between the excessive solution of ω_{osc} scales linearly with n as one expected from the LK model.

We present numerical simulations of the dynamics in the vicinity of the candidate stable state to confirm the foregoing stability analysis on the delayed time. Here, we perturb the stationary state with small signals and track the dynamics of the probabilities. The dynamics are tracked upon adding perturbations $\delta_{c,i}$ to c_e and c_c with respect to the stationary

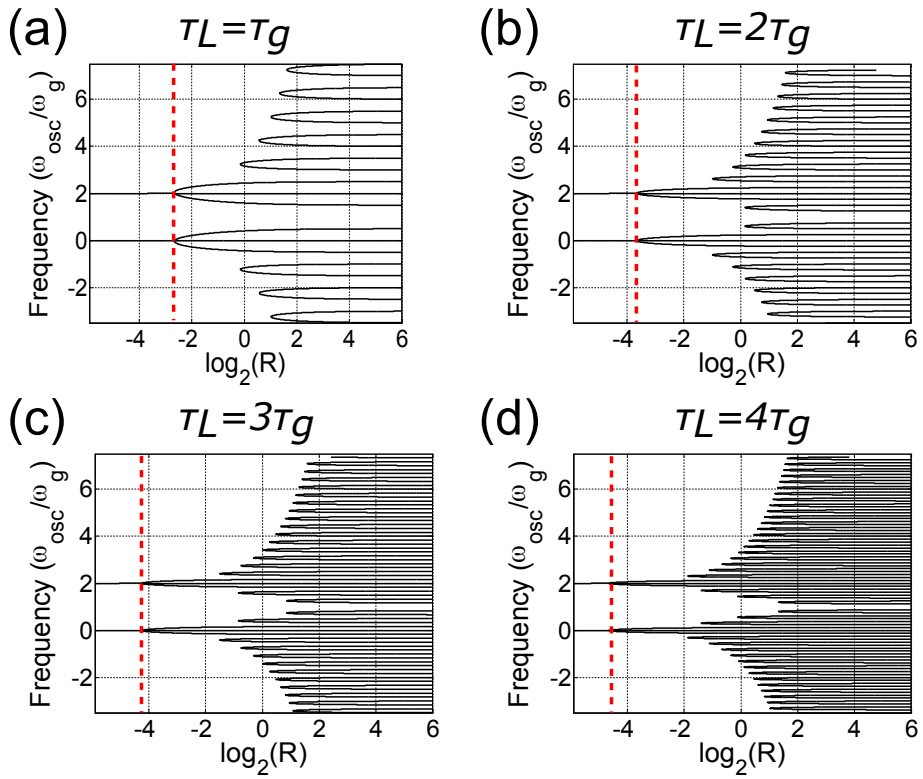

Figure 3.14: The oscillating frequency ω_{osc} of the probability $|c_c(t)|^2$ as function of the multiple of τ_g.

state $\bar{\Psi}(t)$ in Eq. (3.18) $\sim$ (3.20). We perturb the MC photon state *amplitudes* at $t=0$ $\bar{c}_c(0)$ in the vicinity of our candidate stable state with changing the delayed time $\tau_L = \tau_g, 2\tau_g, 3\tau_g$ and $4\tau_g$ ($n = 1, 2, 3$ and 4) at $R = 16$ ($\log_2(R) = 4$). The peaks at frequency of each ω_{osc}/n indicate the consistency of our prediction.

In conclusion, we find a stationary solution where the state probabilities are conserved for a system consisted of a single photon emitter coupled to a EC. Specifically, we give the analytical expression for the stationary solution for such system in one- and two-excitation state. We focus on the case with one excitation and find it is stable by performing stability analysis on the Jacobian of state amplitudes. The stable solutions, obtaining from the eigenvalues of Jocobian, indicate excessive solutions with experimental parameters such as cavity damping rate, the cavity coupling strength, the feedback phase, and the external cavity length. A numerical simulation is used to verify this results, showing inter-

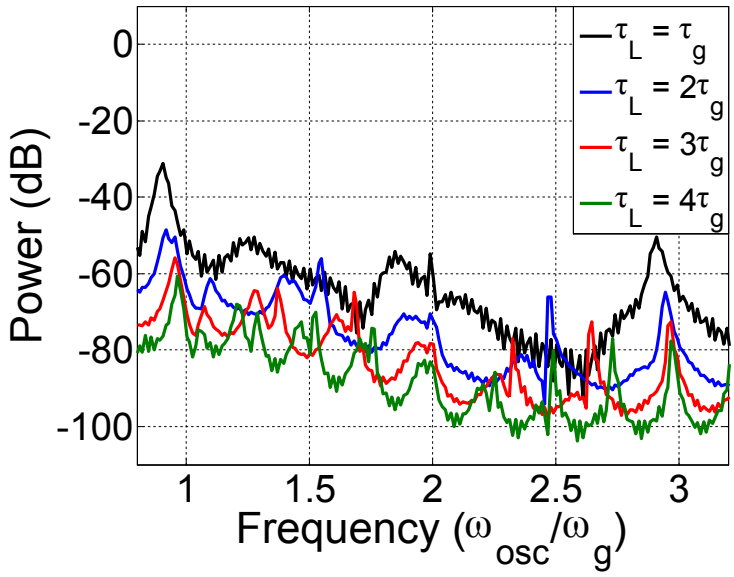

Figure 3.15: The power spectrum of the probability of $c_c(t)$ with different delayed time, $\tau_L = \tau_g, 2\tau_g, 3\tau_g$ and $4\tau_g$ at $R = 16$ ($\ln_2(R) = 4$).

esting dynamics appear in the vicinity of the stationary states. In addition, we calculated the energy eigenvalues (of stationary one- and two- excitation states) analytically and extend our calculation for the stationary state solution to arbitrary integer excitation number. We expect the finding serve as the bridge between classical model and quantum model dealing with photonic structure subjected to optical feedback.

CHAPTER 4
CONCLUSION

This thesis focuses on the effects of time-delayed feedback on solid-state photonic devices. For a laser diode with time-delayed feedback, an external cavity semiconductor laser (ECSL) setup is built. The experimental ECSL setup serves as test-bed for theoretical models; namely, the delay embedding and Pyragas-type feedback are verified in this study. The non-linear effects generated in a ECSL setup provide many potential applications, such as optoelectronic oscillator and random number generation. Given the success of the time-delayed feedback on ECSL, the effects are investigated in the quantum optics regime. Particularly, this thesis investigates the time-delayed feedback in the few-photon regime, and focuses on the Pyragas-type feedback and the stability analysis of finite delayed time.

For an ECSL setup, we investigated the dynamics of ECSL by directly extracting two parameters, voltage vs. intensity, of an ECSL. In the work presented here, we observed a quasi-periodic route to chaos interrupted by two types of limit cycles, *viz.* a simple-harmonic regime and a coexisting periodic-doubling before entering the edge of coherence collapse. Given the rich dynamical behaviors exhibit in both signals, the experimental phase portraits are drown by projecting the trajectories in the parameter space and phase portraits of rich dynamics are hence shown to compare with the reconstructed attractors by embedded-delay. We compare them with theoretical prediction of reconstructed phase portraits based on optical intensity vs. delayed intensity. This comparison of experimental phase portraits and reconstructed phase portraits reveals good qualitative agreement, thus validating the dynamics extracted from the voltage measurements. Indeed, a delayed phase space may share some invariant properties with the actual one (e.g. dimension of attractor, Lyapunov exponents); however, as our results rely on two degrees of freedom, they show promise to more thoroughly test the LK model than can be provided by a single dynamical

variable [46, 102].

In view of the complex dynamics of the ECSL, we have shown by using $V(t)$ (upon which we concentrate here) directly, we can entirely eliminate the need for O/E conversion, which is of interest for some applications. The voltage $V(t)$ across the LD allows for the robust generation of periodic, quasi-periodic, and chaotic oscillations, of various complexities, that have similar characteristics to those obtained from the optical intensity. We demonstrate an ECSL-based OEO that entirely circumvents the need for O/E conversion. The use of an ECSL as a **periodic** OEO is tunable across the entire X-band, from 6.79 to 11.48 GHz. Both the optical $I(t)$ and electrical $V(t)$ signal can be employed for microwave applications. The typical value of Q is 3.4 $\times 10^5$. In addition, we have characterized both amplitude and timing jitters, the amplitude jitters,σ_{amp}, ranges from 0.40 mV to 0.92 mV. We have also characterized the spectral purity via the time jitter is 0.13 ps (in the range $\sigma \approx$ -0.79 to 0.88) and the $\sigma_{tj}/T_{per}(J) = 1.1 \times 10^{-3}$. In an different dynamical regime, namely, the coherence collapse, we implemented an ECSL as a **chaotic** OEO. The chaotic OEOs based on ECSL setup is a potential candidate for straightforward and inexpensive sources of high-dimensional chaos [50], the simple setup is of interest for applications such as chaos radar [51] and ultrahigh rate random-bit generation [8, 52, 9]. In the other dynamical regime, we have demonstrated the use of an ECSL as a novel OEO tunable across the entire X-band, from 6.79 to 11.48 GHz. Both the optical $I(t)$ and electrical $V(t)$ signal can be employed for microwave applications. Specifically, $V(t)$ is obtained by monitoring the voltage across the LD injection terminals under constant-current operation. The quality factor Q is greater than 2×10^5.

Alternatively, a Pyragas-like feedback can be applied to control unwanted chaos and stabilize unstable orbits [3]. This type of feedback is achieved by applying a continuous feedback term which is proportional to the difference of signal at t and $t - \tau$ to the system. We demonstrated that by applying the Pyragas type feedback [3], we can be reduced unstable orbits, *i.e.*, as a novel method in improving the performance of periodic OEO. To

be more specific, we utilize self-modulation of the system by setting the f_{ROF} to be an integer multiple of f_τ in the periodic OEO and, as a result, demonstrate a magnitude reduction of the timing jitter. Such feedback scheme can also be implemented by modulating the injection current $I(t)$ with optoelectronic feedback as shown in [133] or with impulsive delayed feedback [134]. The combination of tunability and low phase-noise figures of merit indicates that the OEOs based on ECSLs may be competitive with the state of the art. Future efforts will be geared towards stabilizing the device and determining the intrinsic performance before amplification.

Turning to quantum systems such as single photon emitters, the optical feedback can be achieved with few photons at delayed time, τ_L from an external mirror. The coherent feedback, as described in this thesis, holds a close similarity as an ECSL setup. As a result, one might expect nonlinear behavior in the number of photons. Indeed, the nonlinearity involving of states with a small number of photons (~ 100 photons has been observed experimentally [85, 86]. These effects cannot be described with a classical electromagnetic field, *i.e.*, the scaling of the behavior with photon number cannot be accounted for by the corresponding optical intensity. In this thesis, a fully quantum mechanical treatment of such time-delayed systems, including the electromagnetic field has been investigated. The complete study is essential to understand the dynamics of single-photon emitters with coherent time-delayed feedback. In the future, the wavefunction approach of coherent quantum feedback takes account of the few-excitation state could provide further investigation on the nonlinearity effects of few photons.

The time parameter that originates from coherent exchange of the photonic and atomic excitations dominates the interaction of the internal state of a single photon emitter. The interplay of two time parameters, atom-photon transition time, τ_g and τ_L, shows interesting dynamics of probability of different states. In this thesis, we demonstrated the Pyragas-type effect appears in quantum optics regime where stabilization of unstable orbits occurs while the delayed time is tuned to multiple integer of atom-photon transition time,

τ_g. Recently, because the recent interest in stationary states in chiral quantum optics with atomic mirror [98] and V-level atoms [99], this thesis studies the stability of the stationary states with single and two excitation states. Particularly, the stability analysis on the state amplitudes focus on the stability in the vicinity of the stationary states. In addition, we find a stationary solution where the state probabilities are conserved for a system consisted of a single photon emitter coupled to a EC. Specifically, we give the analytical expression for the stationary solution for such system in one- and two-excitation state. We focus on the case with one excitation and find it is stable by performing stability analysis on the Jacobian of state amplitudes. The stable solutions, obtaining from the eigenvalues of Jocobian, indicate excessive solutions with experimental parameters such as cavity damping rate, the cavity coupling strength, the feedback phase, and the external cavity length. A numerical simulation is used to verify this results, showing interesting dynamics appear in the vicinity of the stationary states. In addition, we calculated the energy eigenvalues (of stationary one- and two- excitation states) analytically and extend our calculation for the stationary state solution to arbitrary integer excitation number. We expect the finding serve as the bridge between classical model and quantum model dealing with photonic structure subjected to optical feedback.

Appendices

APPENDIX A

EXPERIMENTAL EQUIPMENT

A schematic of our ECSL setup is shown in Fig. A.1. For our experiments, we employ a single longitudinal-mode edge-emitting InGaAsP distributed feedback (DFB) LD containing seven quantum wells in the active region [10]. The grating is designed and fabricated to achieve a k product of 50 cm^{-1} and the length l of the LD cavity is 600 μm, achieving a kl value of 3. The LD is that of Ref. [100]. The LD emits at 1550 nm with a free-running threshold current $J_{th} = 29.8$ mA.

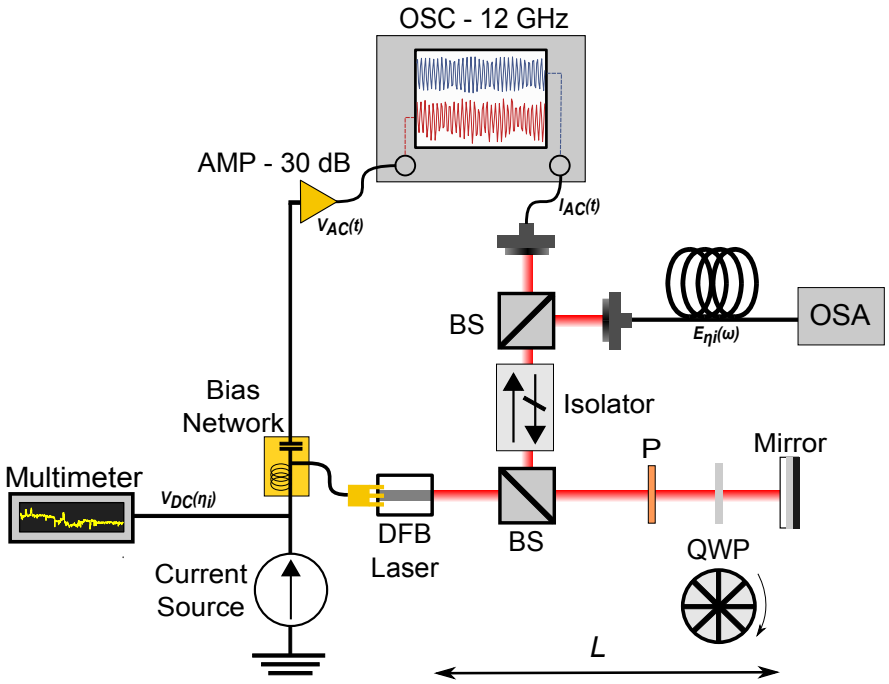

Figure A.1: Experimental setup. OSC: oscilloscope, AMP: radio-frequency (RF) amplifier, OSA: optical spectrum analyzer, BS: beam splitter, P: polarizer, QWP: quarter-wave plate.

During the experiment, the OSA continuously measures the optical spectrum for each η. $V(t)$ is measured across the LD injection terminals utilizing a radio-frequency (RF) probe (Cascade Microtech AE-ACP40-GSG-400) with 40-GHz bandwidth. The DC

and AC components of $V(t) = V_{DC} + V_{AC}(t)$ are separated with a bias tee (Keysight 11612A). The AC component, $V_{AC}(t)$, is amplified (AMP) with an 30-dB amplifier (Microsemi UA030VM) with 30 GHz bandwidth in real-time. In addition, the AC components $I_{AC}(t)$ [of $I(t) = I_{DC} + I_{AC}(t)$] and $V_{AC}(t)$ are simultaneously recorded on a real-time oscilloscope (OSC) (Agilent DSO80804B) with 12 GHz cut-off frequency. The AC signals are small compared with the DC signals leading to the approximate proportionality of these signals to the dynamical relevant degrees of freedom $E(t)$ and $n(t)$ [43].

To tune η, the relative angle between the polarizer (P) and quarter-wave plate (QWP) in Fig. 1 is adjusted in 0.05° increments ($\eta = 1$ corresponds to $\sim$15 % of the optical power coupled back onto the collimating lens). We intentionally reduce the feedback coupling (estimated one-third of the feedback power arrives at the active region of the LD compared to our previous work [10, 11]). This is done by reducing the overlap of the optical mode of the feedback field into the active region of the LD in order to extract a clear BD.

All the synchronization processes are done in CW in the CW regime. We established a temperature controlled environment and we assume the time delays are constant throughout the experiment. The first process is to estimate the optical path and measure the transmission delay in each electrical component (electrical cable, connectors, RF amplifiers). The synchronization is to calculate the time difference between two signals. We estimate the delay time from the free space optical path, i, and measure the transmission delay, v, in each electrical component (electrical cable, connectors, RF amplifiers) with oscilloscope, (except for the delay in the RF probe, which is given by Cascade Microtech to be 32 picoseconds). Second, we apply an external modulation to the laser diode; this allowed us to calculate the time from the tot = i + v, by subtracting tot from two times of time delay we measured in the first step, we obtained the time delay. Lastly, we extracted 30 consecutive time series of both signals and calculated the ACF of two sets of signals while moving the linear positioner (in the same direction of the optical path) underneath the fiber coupler by 0.25 mm. We considered the optimal condition for two signals are fully

synchronized when the intensity signal leads the voltage signal by $\pi/2$ [101]

Noted that the precision of the second step is 25 picoseconds (the sampling time of the oscilloscope) and the last step improves the precision to 0.8 picosecond. We conclude that the precision from both steps are much faster than the relaxation oscillation frequency (10 GHz) at the operating current and other time parameters in ECL, hence should be considered adequately in capturing the phase portrait of intensity and voltage signals.

APPENDIX B

NON-MARKOVIAN AND MARKOVIAN EOM KERNAL

We derive Equation numbers and notation is from Ref. [94]. We begin with Eq, (3.9), which reads

$$\dot{c}_{ck}(t) = iG^*(k,t)c_c(t) \tag{B.1}$$

Consider

$$\int_0^t dt'\ \dot{c}_{ck}(t') = c_{ck}(t) - c_{ck}(0) = c_{ck}(t) \tag{B.2}$$

from the initial conditions. But, from Eq. (3.5), we also have

$$\int_0^t dt'\ \dot{c}_{ck}(t') = i\int_0^t dt'\ G^*(k,t')c_c(t'), \tag{B.3}$$

whence

$$c_{ck}(t) = i\int_0^t dt'\ G^*(k,t')c_c(t'). \tag{B.4}$$

Multiply this expression by $G(k,t)$ and integrate over k (from $-\infty$ to ∞),

$$\begin{aligned}\int dk\ G(k,t)c_{ck}(t) =& i\int_0^t dt'\ c_c(t')R,\\ R =& \int dk\ G(k,t)G^*(k,t').\end{aligned} \tag{B.5}$$

Our task is to evaluate R. To do so, we require the explicit expression for $G(k,t)$ given in Ref. [94]. One finds

$$\begin{aligned}R =& \int dk\ G(k,t)G^*(k,t')\\ =& G_0^2\int dk\ \sin^2 kL\, e^{i\omega_k(t'-t)}e^{-i\omega_0(t'-t)}\\ =& G_0^2 e^{-i\omega_0(t'-t)}\int dk\ \sin^2 kL\, e^{i\omega_k(t'-t)}.\end{aligned} \tag{B.6}$$

Now, $\omega_k = c_0 k$ and

$$\sin^2 kL = -\frac{1}{4}\left(e^{ikL} - e^{-ikL}\right)^2 = -\frac{1}{4}\left(e^{2ikL} + e^{-2ikL} - 2\right). \tag{B.7}$$

Thus,

$$\begin{aligned} R =& -\frac{G_0^2}{4} e^{-i\omega_0(t'-t)} \left\{ \int dk\ e^{ik[c_0(t'-t)+2L]} + \int dk\ e^{ik[c_0(t'-t)-2L]} - 2\int dk\ e^{ikc_0(t'-t)} \right\} \\ =& -\frac{G_0^2}{4c_0} e^{-i\omega_0(t'-t)} \left\{ \int dc_0 k\ e^{ic_0 k[(t'-t)+2L/c_0]} + \int dk\ e^{ic_0 k[(t'-t)-2L/c_0]} - 2\int dk\ e^{ikc_0(t'-t)} \right\} \\ =& -\kappa e^{-i\omega_0(t'-t)} \left\{ \delta(t'-t+\tau) + \delta(t'-t-\tau) - 2\delta(t'-t) \right\}. \end{aligned} \tag{B.8}$$

Therefore we have

$$\int dk\ G(k,t) c_{ck}(t) = i\int_0^t dt'\ c_c(t') R \tag{B.9}$$

$$= -i\kappa \left[e^{i\omega_0\tau} c_c(t-\tau) - \frac{1}{2} 2 c_c(t) \right]. \tag{B.10}$$

We have used $\kappa = \pi G_0^2/(2c_0)$. The term with $\delta(t'-t-\tau)$ does not contribute, as it is out of the range of the t' integral and the factor of $1/2$ in the last term is due to the fact that the corresponding δ function is at one of the limits of integration $t' = t$. Inserting the previous expression into Eq. (4) gives

$$\begin{aligned} \dot{c}_c(t) =& i\gamma c_e(t) + i\int dk\ G(k,t) c_{ck}(t) \\ =& i\gamma c_e(t) - \kappa c_c(t) + \kappa e^{i\omega_0\tau} c_c(t-\tau). \end{aligned} \tag{B.11}$$

Recalling the initial condition that the external cavity is empty of photons for $t \leq 0$, we have the Markovian equation of motion in Eq. (3.10).

$$\dot{c}_c(t) = i\gamma c_e(t) - \kappa c_c(t) + \kappa e^{i\omega_0\tau} \Theta(t-\tau) c_c(t-\tau). \tag{B.12}$$

APPENDIX C

STATIONARY STATE DERIVATION

C.1 single-excitation stationary state

The stationary state satisfying Eqs. (3.7) $\sim$ (3.9) and $\frac{\partial |c_i|}{\partial t} = 0$. In order to find the solution for single excitation case, we replace the states in the phasor expression ($c_i = |c_i(t)|\, e^{i\theta_i(t)}$) and obtain new EOMs ($\frac{\partial c_i}{\partial t} = \frac{|\partial c_i|}{\partial t} \cdot e^{i\theta_i(t)} + i\frac{\theta_i(t)}{\partial t} \cdot |c_i|\, e^{i\theta_i(t)}$, $i = e,\ c$, and k). Hence, the EOMs from Eqs. (C2)-(C4) can be rewritten using the condition for the stationary state,

$$\frac{\partial c_e}{\partial t} = i\frac{\theta_e(t)}{\partial t} \cdot |c_e|\, e^{i\theta_e(t)} = \ i\omega_g\, |c_c|\, e^{i\theta_c(t)}, \tag{C1}$$

$$\frac{\partial c_c}{\partial t} = i\frac{\theta_c(t)}{\partial t} \cdot |c_c|\, e^{i\theta_c(t)} = i\omega_g\, |c_e|\, e^{i\theta_e(t)} + iG_0 e^{i\omega_0 t} \int |c_k|\ \sin(kL) e^{i[\theta_k(t) - \omega_k t]}\, \mathrm{d}k \tag{C2}$$

$$\frac{\partial c_k}{\partial t} = i\frac{\theta_k(t)}{\partial t} \cdot |c_k(k)|\, e^{i\theta_k(t)} = \ iG_0 e^{i\theta_c(t) - i\omega_g t}\, |c_c| \sin(kL) e^{i\omega_k t} \tag{C3}$$

From Eq. (C1), we obtain $\theta_e(t) = \frac{|c_c|}{|c_e|}\omega_g t + \phi$ where $\phi = \theta_e(t) - \theta_c(t)$. Taking this relationship to Eq. (C2) and we have a simple solution $|c_c| = |c_e|$. These two conditions combine with Eq. (C3) yield $\theta_k(t) = (\omega_g - \omega_0 + \omega_k)\ t$ and $|c_k(k)| = G_0\, |c_c|\, \frac{\sin(kL)}{\omega_g - \omega_0 + \omega_k}$. Next, the normalization constant, α_I, single excitation case can be found from the normalization condition

$$\begin{aligned} 1 &= |c_e|^2 + |c_c|^2 + \int_{-\infty}^{\infty} |c_k|^2\, \mathrm{d}k \\ &= \alpha_I^2 [\ 2 + \frac{G_0^2 L\pi}{c_0^2}\ ] = \ \alpha_I^2 [\ 2 + \kappa\tau_L\ ] \end{aligned} \tag{C4}$$

such that $\alpha_I = (2 + \kappa\tau_L)^{-1}$.

C.2 Two-excitation stationary state

In the two-excitation state, the dipole-dipole interaction lowers energy of biexciton state ($|\{e,\ e\},0,0\rangle$) from $2\omega_{cv}$ by the binding energy. As a result, the optical field defined by the micropillar cavity suppresses the population in the biexciton state. The wavefunction of two-excitation case is hence the superposition of two states with additional three sets of state dealing with the external cavity photons. The wavefunction is written as

$$\begin{aligned}|\Psi_{II}(t)\rangle = c_{ec}(t)\,|e,1,0\rangle + c_{cc}(t)\,|g,2,0\rangle \\ + \int c_{ek}(t)\,|e,0,k\rangle\,\mathrm{d}k + \int c_{ck}(t)\,|g,1,k\rangle\,\mathrm{d}k \\ + \int\int c_{kk'}(t)\,|g,0,\{k,k'\}\rangle\,\mathrm{d}k\mathrm{d}k'\end{aligned} \tag{C5}$$

Where the state coefficients are: c_{ec} stands for QD in excited state and one microcavity photon and no external cavity photon; c_{cc} stands for two photons in the microcavity and the external cavity being in vacuum and the two-level system as well as the radiation field in the waveguide being in the ground state; c_{ck}: one microcavity photon and one external cavity photon with wave vector k; c_{ek} stands for the excited state of the QD and one photon in the external cavity of mode k; $c_{kk'}$: two EC-photon state with wavevectors, k and k', with the QD as well as microcavity being in the ground state.

Next, we derive the EOMs in the two excitation limit by substituting the interaction Hamiltonian, $H_{int,RWA}$ in Eq. (3) and the two-excitation wavefunction Eq. (7). The EOMs of the two excitation

$$\frac{\partial c_{ec}}{\partial t} = i\omega_g c_{cc} + i\int_{-\infty}^{\infty} c_{ek}G(k,t)\mathrm{d}k, \tag{C6}$$

$$\frac{\partial c_{ek}}{\partial t} = i\omega_g c_{ck} + ic_{ec}G^*(k,t), \tag{C7}$$

$$\frac{\partial c_{cc}}{\partial t} = i\omega_g c_{ec} + i\int_{-\infty}^{\infty} c_{ck}G(k,t)\mathrm{d}k, \tag{C8}$$

$$\frac{\partial c_{ck}}{\partial t} = i\omega_g c_{ek} + i\int_{-\infty}^{\infty} c_{kk'}G(k',t)\mathrm{d}k' + ic_{cc}G^*(k,t), \tag{C9}$$

$$\frac{\partial c_{kk'}}{\partial t} = ic_{ck'}G^*(k,t) + ic_{ck}G^*(k',t). \tag{C10}$$

Following the same argument described in single excitation state. We looks for the stationary state solution satisfing Eq. (C2) $\sim$ (C10). The solution for the phase function for each state can be found from the same argument in section B; one finds the $\theta_{ec} = \theta_{cc} = \omega_g t$ and $\theta_{ek} = \theta_{ck} = (\omega_k - \omega_0 + \omega_g)t$ and lastly, $\theta_{kk'} = (\omega_k + \omega_{k'} - 2\omega_0 + \omega_g)t$.

The magnitudes for each state can be solved using the following equations Eq. (C7) $\sim$ (C1) and as well as the normalization relationship Eq. (C12)

$$\frac{\partial \theta_{ec}}{\partial t} = \omega_g \frac{|c_{cc}|}{|c_{ec}|}e^{i(\theta_{cc}-\theta_{ec})} + \frac{G_0}{|c_{ec}|}e^{i(\omega_g t-\theta_{ec})}\int_{-\infty}^{\infty}|c_{ek}|\sin(kL)e^{i(\theta_{ek}-\omega_k t)}\mathrm{d}k \tag{C11}$$

$$\frac{\partial \theta_{ek}}{\partial t} = \omega_g \frac{|c_{ck}|}{|c_{ek}|}e^{i(\theta_{ck}-\theta_{ek})} + G_0\,|c_{ec}|\,e^{i(\theta_{ec}-\omega_g t)}\frac{\sin(kL)}{|c_{ek}|}e^{i(\omega_k t-\theta_{ek})} \tag{C12}$$

$$\frac{\partial \theta_{cc}}{\partial t} = \omega_g \frac{|c_{ec}|}{|c_{cc}|}e^{i(\theta_{ec}-\theta_{cc})} + \frac{G_0}{|c_{cc}|}e^{i(\omega_g t-\theta_{cc})}\int_{-\infty}^{\infty}|c_{ck}|\sin(kL)e^{i(\theta_{ck}-\omega_k t)}\mathrm{d}k \tag{C13}$$

$$\begin{aligned}\frac{\partial \theta_{ck}}{\partial t} &= \omega_g \frac{|c_{ek}|}{|c_{ck}|}e^{i(\theta_{ek}-\theta_{ck})} + G_0\,|c_{cc}|\,e^{i(\theta_{cc}-\omega_g t)}\frac{\sin(kL)}{|c_{ck}|}e^{i(\omega_k t-\theta_{ck})} \\ &\quad + \frac{G_0}{|c_{ck}|}e^{i(\omega_g t-\theta_{ck})}\int_{-\infty}^{\infty}|c_{kk'}|\sin(k'L)e^{i(\theta_{kk'}-\omega_{k'}t)}\mathrm{d}k'\end{aligned} \tag{C14}$$

$$\frac{\partial \theta_{kk'}}{\partial t} = G_0\,|c_{ck}|\,e^{i\omega_g t}\frac{\sin(k'L)}{|c_{kk'}|}e^{i(\omega_k t+\theta_{ck}-\theta_{kk'})} + G_0\,|c_{ck'}|\,e^{i\omega_g t}\frac{\sin(kL)}{|c_{kk'}|}e^{i(\omega_{k'}t+\theta_{ck'}-\theta_{kk'})}. \tag{C15}$$

We have $|c_{ec}| = |c_{cc}|$; $|c_{ek}| = |c_{ck}| = G_0|c_{ec}|\frac{\sin(kL)}{\omega_k - \omega_0}$ for all k; and

$$|c_{kk'}| = G_0|c_{ck}|\frac{\sin(kL)}{\omega_k + \omega_{k'} - 2\omega_0 + \omega_g} = G_0^2|c_{ec}|\frac{\sin(kL)}{\omega_k - \omega_0}\frac{\sin(k'L)}{\omega_k + \omega_{k'} - 2\omega_0 + \omega_g} \quad \text{(C.1)}$$

We define a new parameter,α_{II}, in two-excitation space $|c_{ec}| = |c_{cc}| = \alpha_{II}$. It can be solved by normalization condition

$$\begin{aligned} 1 &= |c_{ec}|^2 + |c_{cc}|^2 + \int_{-\infty}^{\infty} |c_{ck}(k)|^2 \, \mathrm{d}k + \int_{-\infty}^{\infty} |c_{ek}(k)|^2 \, \mathrm{d}k + \int_{-\infty}^{\infty}\int_{-\infty}^{\infty} |c_{kk'}(k,k')|^2 \, \mathrm{d}k\mathrm{d}k' \\ &= 2\,|c_{ec}|^2 + 2G_0^2\,|c_{ec}|^2 \int_{-\infty}^{\infty} \left|\frac{\sin(kL)}{\bar{k} - \bar{k_g}}\right|^2 \, \mathrm{d}k + \int_{-\infty}^{\infty}\int_{-\infty}^{\infty} |c_{kk'}(k,k')|^2 \, \mathrm{d}k\mathrm{d}k' \\ &= |c_{ec}|^2\,[2 + \frac{2G_0^2 L}{c^2} \int_{-\infty}^{\infty} \left|\frac{\sin(\bar{k})}{\bar{k} - \bar{k_g}}\right|^2 \, \mathrm{d}\bar{k} + R_{II}\,]; \end{aligned} \quad \text{(C16)}$$

$$\begin{aligned} R_{II} &= G_0^2 \int_{-\infty}^{\infty}\int_{-\infty}^{\infty} [\frac{\sin(kL)}{\omega_k - \omega_0}\frac{\sin(k'L)}{\omega_k + \omega_{k'} - 2\omega_0 + \omega_g}]^2 \, \mathrm{d}k\mathrm{d}k' \\ &= \frac{G_0^2 L^2}{c^4} \int_{-\infty}^{\infty}\int_{-\infty}^{\infty} [\frac{\sin(\bar{k})\sin(\bar{k'})}{\bar{k} + \bar{k'} - 2\bar{k_0} + \bar{k_g}} \frac{1}{\bar{k} - \bar{k_0}}]^2 \, \mathrm{d}\bar{k}\mathrm{d}\bar{k'} = \frac{G_0^2 L^2 \pi^2}{c^4} = \kappa^2 \tau_L^2. \end{aligned} \quad \text{(C17)}$$

Where $\bar{k} = kL$, $\bar{k'} = k'L$ and $\bar{k_g} = \frac{\omega_g L}{c}$. Finally, we find a different parameter, α_{II}, from the normalization conditions in Eq. (C13) such that $\alpha_{II} = |c_{ec}| = (2 + \frac{2\pi G_0^2 L}{c_0^2} + \frac{G_0^4 L^2 \pi^2}{c_0^4})^{-1/2} = (2 + 2\tau_L\kappa + \tau_L^2\kappa^2)^{-1/2}$.

C.3 Time step discretization

The numerical simulation was performed using discrete time step Δ_t much smaller than the other time scales associate to the system.

$$\Delta_t \ll \omega_g^{-1},\ \kappa^{-1} \quad \text{(C18)}$$

On the other hand, the frequency resolution, Δ_f, and the frequency ranges, R_f, are determined by the required limits of discrete Fourier transform. In all simulation cases for single excitation state above, they are determined by with the following relationship

$\Delta_f = \frac{\omega_g}{4\pi t_0}$, and $R_f = \frac{\Delta_t}{2\pi}$. Where the length of the time, (in our case, $t_0 = 4\tau_g$) and the time step, $\Delta_t = 10^{-5} \times 2\pi/\omega_g$.

REFERENCES

[1] J. C. Doyle, B. A. Francis, and A. R. Tannenbaum, *Feedback control theory*. Courier Corporation, 2013.

[2] N. S. Bergano, F. W. Kerfoot, and C. R. Davidsion, "Margin measurements in optical amplifier system," *IEEE Photonics Technology Letters*, vol. 5, no. 3, pp. 304–306, 1993.

[3] K. Pyragas, "Continuous control of chaos by self-controlling feedback," *Physics Letters A*, vol. 170, no. 6, pp. 421 –428, 1992.

[4] S. Bielawski, D. Derozier, and P. Glorieux, "Experimental characterization of unstable periodic orbits by controlling chaos," *Phys. Rev. A*, vol. 47, R2492–R2495, 4 1993.

[5] J. E. S. Socolar, D. W. Sukow, and D. J. Gauthier, "Stabilizing unstable periodic orbits in fast dynamical systems," *Phys. Rev. E*, vol. 50, pp. 3245–3248, 4 1994.

[6] L. A. Sanchez, "Existence of periodic orbits for high-dimensional autonomous systems," *Journal of Mathematical Analysis and Applications*, vol. 363, no. 2, pp. 409 –418, 2010.

[7] F.-Y. Lin and J.-M. Liu, "Chaotic radar using nonlinear laser dynamics," *IEEE Journal of Quantum Electronics*, vol. 40, no. 6, pp. 815–820, 2004.

[8] A. Uchida, K. Amano, M. Inoue, K. Hirano, S. Naito, H. Someya, I. Oowada, T. Kurashige, M. Shiki, S. Yoshimori, *et al.*, "Fast physical random bit generation with chaotic semiconductor lasers," *Nature Photonics*, vol. 2, no. 12, pp. 728–732, 2008.

[9] N. Li, B. Kim, V. N. Chizhevsky, A. Locquet, M. Bloch, D. S. Citrin, and W. Pan, "Two approaches for ultrafast random bit generation based on the chaotic dynamics of a semiconductor laser," *Opt. Express*, vol. 22, no. 6, pp. 6634–6646, 2014.

[10] C. Chang, D. Choi, A Locquet, M. J. Wishon, K Merghem, A. Ramdane, F. Lelarge, A Martinez, and D. Citrin, "A multi-ghz chaotic optoelectronic oscillator based on laser terminal voltage," *Applied Physics Letters*, vol. 108, no. 19, p. 191 109, 2016.

[11] C. Y. Chang, M. J. Wishon, D. Choi, J. Dong, K. Merghem, A. Ramdane, F. Lelarge, A. Martinez, A. Locquet, and D. S. Citrin, "Tunable x-band optoelectronic oscil-

lators based on external-cavity semiconductor lasers," *IEEE Journal of Quantum Electronics*, vol. 53, no. 3, pp. 1–6, 2017.

[12] A. Argyris, D. Syvridis, L. Larger, V. Annovazzi-Lodi, P. Colet, I. Fischer, J. Garcia-Ojalvo, C. R. Mirasso, L. Pesquera, and K. A. Shore, "Chaos-based communications at high bit rates using commercial fibre-optic links," *Nature*, vol. 438, no. 7066, pp. 343–346, 2005.

[13] D. Rontani, M. Sciamanna, A. Locquet, and D. S. Citrin, "Multiplexed encryption using chaotic systems with multiple stochastic-delayed feedbacks," *Phys. Rev. E*, vol. 80, p. 066 209, 6 2009.

[14] W. L. Zhang, W. Pan, B. Luo, X. H. Zou, M. Y. Wang, and Z. Zhou, "Chaos synchronization communication using extremely unsymmetrical bidirectional injections," *Opt. Lett.*, vol. 33, no. 3, pp. 237–239, 2008.

[15] D Rontani, D Choi, C.-Y. Chang, A Locquet, and D. Citrin, "Compressive sensing with optical chaos," *Scientific reports*, vol. 6, 2016.

[16] L. Larger, A. Baylón-Fuentes, R. Martinenghi, V. S. Udaltsov, Y. K. Chembo, and M. Jacquot, "High-speed photonic reservoir computing using a time-delay-based architecture: Million words per second classification," *Phys. Rev. X*, vol. 7, p. 011 015, 1 2017.

[17] J. Bueno, D. Brunner, M. C. Soriano, and I. Fischer, "Conditions for reservoir computing performance using semiconductor lasers with delayed optical feedback," *Opt. Express*, vol. 25, no. 3, pp. 2401–2412, 2017.

[18] M. C. Soriano, J. García-Ojalvo, C. R. Mirasso, and I. Fischer, "Complex photonics: Dynamics and applications of delay-coupled semiconductors lasers," *Rev. Mod. Phys.*, vol. 85, pp. 421–470, 1 2013.

[19] C. Masoller and N. B. Abraham, "Stability and dynamical properties of the coexisting attractors of an external-cavity semiconductor laser," *Phys. Rev. A*, vol. 57, pp. 1313–1322, 2 1998.

[20] J. Mørk, J. Mark, and B. Tromborg, "Route to chaos and competition between relaxation oscillations for a semiconductor laser with optical feedback," *Phys. Rev. Lett.*, vol. 65, pp. 1999–2002, 16 1990.

[21] A. Cerjan and A. D. Stone, "Why the laser linewidth is so narrow: A modern perspective," *Physica Scripta*, vol. 91, no. 1, p. 013 003, 2016.

[22] D. Brunner, X. Porte, M. C. Soriano, and I. Fischer, "Real-time frequency dynamics and high-resolution spectra of a semiconductor laser with delayed feedback," *Scientific reports*, vol. 2, p. 732, 2012.

[23] B Krauskopf, "Bifurcation analysis of laser systems," in *Fundamental Issues of Nonlinear Laser Dynamics*, B Krauskopf and D Lenstra, Eds. American Institute of Physics, 2000, pp. 1 –30, Other: AIP Conference Proceedings, 548, ISBN: 1563969777.

[24] N. Li, L. Zunino, A. Locquet, B. Kim, D. Choi, W. Pan, and D. S. Citrin, "Multiscale ordinal symbolic analysis of the lang-kobayashi model for external-cavity semiconductor lasers: A test of theory," *IEEE Journal of Quantum Electronics*, vol. 51, no. 8, pp. 1–6, 2015.

[25] R. Lang and K. Kobayashi, "External optical feedback effects on semiconductor injection laser properties," *IEEE Journal of Quantum Electronics*, vol. 16, no. 3, pp. 347–355, 1980.

[26] W.-S. Lam, P. N. Guzdar, and R. Roy, "Hilbert phase analysis of the dynamics of a semiconductor laser with optical feedback," *Phys. Rev. E*, vol. 67, p. 025 604, 2 2003.

[27] B. Tromborg and J. Mork, "Stability analysis and the route to chaos for laser diodes with optical feedback," *IEEE Photonics Technology Letters*, vol. 2, no. 8, pp. 549–552, 1990.

[28] Y. H. Kao, N. M. Wang, and H. M. Chen, "Mode description of routes to chaos in external-cavity coupled semiconductor lasers," *IEEE Journal of Quantum Electronics*, vol. 30, no. 8, pp. 1732–1739, 1994.

[29] M. Ahmed, M. Yamada, and S. Abdulrhmann, "Numerical modeling of the route-to-chaos of semiconductor lasers under optical feedback and its dependence on the external-cavity length," *International Journal of Numerical Modelling: Electronic Networks, Devices and Fields*, vol. 22, no. 6, pp. 434–445, 2009.

[30] T. Mukai and K. Otsuka, "New route to optical chaos: Successive-subharmonic-oscil- lation cascade in a semiconductor laser coupled to an external cavity," *Phys. Rev. Lett.*, vol. 55, pp. 1711–1714, 17 1985.

[31] J. Mork, B. Tromborg, and J. Mark, "Chaos in semiconductor lasers with optical feedback: Theory and experiment," *IEEE Journal of Quantum Electronics*, vol. 28, no. 1, pp. 93–108, 1992.

[32] B. Kim, A. Locquet, N. Li, D. Choi, and D. S. Citrin, "Bifurcation-cascade diagrams of an external-cavity semiconductor laser: Experiment and theory," *IEEE Journal of Quantum Electronics*, vol. 50, no. 12, pp. 965–972, 2014.

[33] B. Krauskopf, "Bifurcation analysis of laser systems," in *AIP Conference Proceedings*, AIP, vol. 548, 2000, pp. 1–30.

[34] A. Hohl and A. Gavrielides, "Bifurcation cascade in a semiconductor laser subject to optical feedback," *Phys. Rev. Lett.*, vol. 82, pp. 1148–1151, 6 1999.

[35] B. Kim, A. Locquet, N. Li, D. Choi, and D. S. Citrin, "Bifurcation-cascade diagrams of an external-cavity semiconductor laser: Experiment and theory," *IEEE Journal of Quantum Electronics*, vol. 50, no. 12, pp. 965–972, 2014.

[36] B. Kim, N. Li, A. Locquet, and D. S. Citrin, "Experimental bifurcation-cascade diagram of an external-cavity semiconductor laser," *Opt. Express*, vol. 22, no. 3, pp. 2348–2357, 2014.

[37] B. Kim, A. Locquet, D. Choi, and D. S. Citrin, "Experimental route to chaos of an external-cavity semiconductor laser," *Phys. Rev. A*, vol. 91, p. 061 802, 6 2015.

[38] D. Brunner, M. C. Soriano, X. Porte, and I. Fischer, "Experimental phase-space tomography of semiconductor laser dynamics," *Phys. Rev. Lett.*, vol. 115, p. 053 901, 5 2015.

[39] J. Mørk, J. Mark, and B. Tromborg, "Route to chaos and competition between relaxation oscillations for a semiconductor laser with optical feedback," *Phys. Rev. Lett.*, vol. 65, pp. 1999–2002, 16 1990.

[40] A. Hohl and A. Gavrielides, "Bifurcation cascade in a semiconductor laser subject to optical feedback," *Phys. Rev. Lett.*, vol. 82, pp. 1148–1151, 6 1999.

[41] H. Li, J. Ye, and J. G. McInerney, "Detailed analysis of coherence collapse in semiconductor lasers," *IEEE Journal of Quantum Electronics*, vol. 29, no. 9, pp. 2421–2432, 1993.

[42] B. Kim, A. Locquet, D. Choi, and D. S. Citrin, "Experimental route to chaos of an external-cavity semiconductor laser," *Phys. Rev. A*, vol. 91, p. 061 802, 6 2015.

[43] R. Kazarinov and R. Suris, "Heterodyne reception of light by an injection laser," *Zhurnal Eksperimental'noi i Teoreticheskoi Fiziki*, vol. 66, pp. 1067–1078, 1974.

[44] W. Ray, W.-S. Lam, P. N. Guzdar, and R. Roy, "Observation of chaotic itinerancy in the light and carrier dynamics of a semiconductor laser with optical feedback," *Phys. Rev. E*, vol. 73, p. 026 219, 2 2006.

[45] A. A. Sahai, B. Kim, D. Choi, A. Locquet, and D. S. Citrin, "Mapping the nonlinear dynamics of a laser diode via its terminal voltage," *Opt. Lett.*, vol. 39, no. 19, pp. 5630–5633, 2014.

[46] S. Wieczorek, B. Krauskopf, T. B. Simpson, and D. Lenstra, "The dynamical complexity of optically injected semiconductor lasers," *Physics Reports*, vol. 416, no. 1, pp. 1–128, 2005.

[47] T. Sauer, J. A. Yorke, and M. Casdagli, "Embedology," *Journal of statistical Physics*, vol. 65, no. 3, pp. 579–616, 1991.

[48] F. Takens *et al.*, "Detecting strange attractors in turbulence," *Lecture notes in mathematics*, vol. 898, no. 1, pp. 366–381, 1981.

[49] H. Whitney, "Differentiable manifolds," *Annals of Mathematics*, pp. 645–680, 1936.

[50] I. Fischer, O. Hess, W. Elsäβer, and E. Göbel, "High-dimensional chaotic dynamics of an external cavity semiconductor laser," *Phys. Rev. Lett.*, vol. 73, pp. 2188–2191, 16 1994.

[51] F.-Y. Lin and J.-M. Liu, "Chaotic radar using nonlinear laser dynamics," *IEEE Journal of Quantum Electronics*, vol. 40, no. 6, pp. 815–820, 2004.

[52] K. Hirano, T. Yamazaki, S. Morikatsu, H. Okumura, H. Aida, A. Uchida, S. Yoshimori, K. Yoshimura, T. Harayama, and P. Davis, "Fast random bit generation with bandwidth-enhanced chaos in semiconductor lasers," *Opt. Express*, vol. 18, no. 6, pp. 5512–5524, 2010.

[53] D. Rontani, M. Sciamanna, A. Locquet, and D. S. Citrin, "Multiplexed encryption using chaotic systems with multiple stochastic-delayed feedbacks," *Phys. Rev. E*, vol. 80, p. 066 209, 6 2009.

[54] L. Maleki, "Sources: The optoelectronic oscillator," *Nature Photonics*, vol. 5, no. 12, pp. 728–730, 2011.

[55] X. S. Yao and L. Maleki, "Converting light into spectrally pure microwave oscillation," *Opt. Lett.*, vol. 21, no. 7, pp. 483–485, 1996.

[56] J. Yao, "Microwave photonics: Photonic generation of microwave and millimeter-wave signals," *International Journal Of Microwave And Optical Technology*, vol. 5, no. 1, pp. 16–21, 2010.

[57] ——, "Photonic generation of microwave arbitrary waveforms," *Optics Communications*, vol. 284, no. 15, pp. 3723 –3736, 2011.

[58] Y. Paquot, F. Duport, A. Smerieri, J. Dambre, B. Schrauwen, M. Haelterman, and S. Massar, "Optoelectronic reservoir computing," *Scientific reports*, vol. 2, 2012.

[59] S. Sunada, T. Harayama, K. Arai, J. Muramatsu, K. Yoshimura, K. Tsuzuki, P. Davis, and A. Uchida, "Theory and experiments of fast non-deterministic random bit generation using on-chip chaos lasers," *Procedia IUTAM*, vol. 5, pp. 190 –194, 2012.

[60] A. D.B.J.R.B.H.J. K. J. McKeever A. Boca, "Experimental realization of a one-atom laser in the regime of strong coupling," *Nature*, vol. 425, no. 1, pp. 268–271, 1997.

[61] P. Lodahl, S. Mahmoodian, and S. Stobbe, "Interfacing single photons and single quantum dots with photonic nanostructures," *Reviews of Modern Physics*, vol. 87, no. 2, p. 347, 2015.

[62] A. Reiserer and G. Rempe, "Cavity-based quantum networks with single atoms and optical photons," *Reviews of Modern Physics*, vol. 87, no. 4, p. 1379, 2015.

[63] P. Lodahl, A. F. Van Driel, I. S. Nikolaev, A. Irman, *et al.*, "Controlling the dynamics of spontaneous emission from quantum dots by photonic crystals," *Nature*, vol. 430, no. 7000, p. 654, 2004.

[64] I. Söllner, S. Mahmoodian, S. L. Hansen, L. Midolo, A. Javadi, G. Kiršanskė, T. Pregnolato, H. El-Ella, E. H. Lee, J. D. Song, *et al.*, "Deterministic photon–emitter coupling in chiral photonic circuits," *Nature nanotechnology*, vol. 10, no. 9, pp. 775–778, 2015.

[65] M. Nomura, N. Kumagai, S. Iwamoto, Y. Ota, and Y. Arakawa, "Laser oscillation in a strongly coupled single quantum dot-nanocavity system," *arXiv preprint arXiv:0905.3063*, 2009.

[66] C Böckler, S Reitzenstein, C Kistner, R Debusmann, A Löffler, T Kida, S Höfling, A Forchel, L Grenouillet, J Claudon, *et al.*, "Electrically driven high-q quantum dot-micropillar cavities," *Applied Physics Letters*, vol. 92, no. 9, p. 091 107, 2008.

[67] O Gazzano, S. M. de Vasconcellos, C Arnold, A Nowak, E Galopin, I Sagnes, L Lanco, A Lemaître, and P Senellart, "Bright solid-state sources of indistinguishable single photons," *Nature communications*, vol. 4, p. 1425, 2013.

[68] D. Bouwmeester, J.-W. Pan, K. Mattle, M. Eibl, H. Weinfurter, and A. Zeilinger, "Experimental quantum teleportation," *Nature*, vol. 390, no. 6660, pp. 575–579, 1997.

[69] V Giesz, N Somaschi, G Hornecker, T Grange, B Reznychenko, L De Santis, J Demory, C Gomez, I Sagnes, A Lemaître, *et al.*, "Coherent manipulation of a solid-state artificial atom with few photons," *Nature communications*, vol. 7, 2016.

[70] D. Dong and I. R. Petersen, "Quantum control theory and applications: A survey," *IET Control Theory & Applications*, vol. 4, no. 12, pp. 2651–2671, 2010.

[71] A. C. Doherty, S. Habib, K. Jacobs, H. Mabuchi, and S. M. Tan, "Quantum feedback control and classical control theory," *Physical Review A*, vol. 62, no. 1, p. 012 105, 2000.

[72] A. Serafini, "Feedback control in quantum optics: An overview of experimental breakthroughs and areas of application," *ISRN Optics*, vol. 2012, 2012.

[73] H. M. Wiseman and G. J. Milburn, *Quantum measurement and control*. Cambridge university press, 2009.

[74] H. M. Wiseman and G. J. Milburn, "Quantum theory of optical feedback via homodyne detection," *Phys. Rev. Lett.*, vol. 70, pp. 548–551, 5 1993.

[75] S. M. Hein, F. Schulze, A. Carmele, and A. Knorr, "Entanglement control in quantum networks by quantum-coherent time-delayed feedback," *Phys. Rev. A*, vol. 91, p. 052 321, 5 2015.

[76] M. Kraft, S. M. Hein, J. Lehnert, E. Schöll, S. Hughes, and A. Knorr, "Time-delayed quantum coherent pyragas feedback control of photon squeezing in a degenerate parametric oscillator," *Phys. Rev. A*, vol. 94, p. 023 806, 2 2016.

[77] S. Lloyd, "Coherent quantum feedback," *Phys. Rev. A*, vol. 62, p. 022 108, 2 2000.

[78] H. M. Wiseman and G. J. Milburn, "All-optical versus electro-optical quantum-limited feedback," *Phys. Rev. A*, vol. 49, pp. 4110–4125, 5 1994.

[79] N. Roch, M. E. Schwartz, F. Motzoi, C. Macklin, R. Vijay, A. W. Eddins, A. N. Korotkov, K. B. Whaley, M. Sarovar, and I. Siddiqi, "Observation of measurement-induced entanglement and quantum trajectories of remote superconducting qubits," *Phys. Rev. Lett.*, vol. 112, p. 170 501, 17 2014.

[80] A Goban, C.-L. Hung, S.-P. Yu, J. Hood, J. Muniz, J. Lee, M. Martin, A. McClung, K. Choi, D. Chang, *et al.*, "Atom–light interactions in photonic crystals," *Nature communications*, vol. 5, 2014.

[81] A. F. Van Loo, A. Fedorov, K. Lalumière, B. C. Sanders, A. Blais, and A. Wallraff, "Photon-mediated interactions between distant artificial atoms," *Science*, vol. 342, no. 6165, pp. 1494–1496, 2013.

[82] M. Wolfrum and S. Yanchuk, "Eckhaus instability in systems with large delay," *Physical review letters*, vol. 96, no. 22, p. 220 201, 2006.

[83] K Green, "Bifurcation analysis of delay-induced periodic oscillations," *Journal of Computational and Applied Mathematics*, vol. 233, no. 9, pp. 2405–2412, 2010.

[84] W ECKHAUS, "Studies in non-linear stability theory(book on nonlinear stability theory of physical systems discussing behavior of solutions, asymptotic method, periodic solutions and poiseuille flow)," *NEW YORK, SPRINGER-VERLAG, INC., 1965. 117 P*, 1965.

[85] C Hopfmann, F Albert, C Schneider, S. Höfling, M Kamp, A Forchel, I Kanter, and S Reitzenstein, "Nonlinear emission characteristics of quantum dot–micropillar lasers in the presence of polarized optical feedback," *New Journal of Physics*, vol. 15, no. 2, p. 025 030, 2013.

[86] F. Albert, C. Hopfmann, S. Reitzenstein, C. Schneider, S. Höfling, L. Worschech, M. Kamp, W. Kinzel, A. Forchel, and I. Kanter, "Observing chaos for quantum-dot microlasers with external feedback," *Nature communications*, vol. 2, p. 366, 2011.

[87] R. J. Cook and P. W. Milonni, "Quantum theory of an atom near partially reflecting walls," *Phys. Rev. A*, vol. 35, pp. 5081–5087, 12 1987.

[88] U. Dorner and P. Zoller, "Laser-driven atoms in half-cavities," *Phys. Rev. A*, vol. 66, p. 023 816, 2 2002.

[89] A. Beige, J. Pachos, and H. Walther, "Spontaneous emission of an atom in front of a mirror," *Phys. Rev. A*, vol. 66, p. 063 801, 6 2002.

[90] A. L. Grimsmo, "Time-delayed quantum feedback control," *Physical review letters*, vol. 115, no. 6, p. 060 402, 2015.

[91] Y.-L. L. Fang, H. U. Baranger, *et al.*, "Waveguide qed: Power spectra and correlations of two photons scattered off multiple distant qubits and a mirror," *Physical Review A*, vol. 91, no. 5, p. 053 845, 2015.

[92] P.-O. Guimond, M. Pletyukhov, H. Pichler, and P. Zoller, "Delayed coherent quantum feedback from a scattering theory and a matrix product state perspective," *Quantum Science and Technology*, 2017.

[93] A. Carmele, J. Kabuss, F. Schulze, S. Reitzenstein, and A. Knorr, "Single photon delayed feedback: A way to stabilize intrinsic quantum cavity electrodynamics," *Phys. Rev. Lett.*, vol. 110, p. 013 601, 1 2013.

[94] J. Kabuss, D. O. Krimer, S. Rotter, K. Stannigel, A. Knorr, and A. Carmele, "Analytical study of quantum feedback enhanced rabi oscillations," *Phys. Rev. A*, vol. 92, p. 053 801, 2015.

[95] H. Pichler and P. Zoller, "Photonic circuits with time delays and quantum feedback," *Physical review letters*, vol. 116, no. 9, p. 093 601, 2016.

[96] A. L. Grimsmo, A. Parkins, and B. Skagerstam, "Rapid steady-state convergence for quantum systems using time-delayed feedback control," *New Journal of Physics*, vol. 16, no. 6, p. 065 004, 2014.

[97] S. M. Hein, F. Schulze, A. Carmele, and A. Knorr, "Optical feedback-enhanced photon entanglement from a biexciton cascade," *Phys. Rev. Lett.*, vol. 113, p. 027 401, 2 2014.

[98] D. E. Chang, L Jiang, A. Gorshkov, and H. Kimble, "Cavity qed with atomic mirrors," *New Journal of Physics*, vol. 14, no. 6, p. 063 003, 2012.

[99] P.-O. Guimond, H. Pichler, A. Rauschenbeutel, and P. Zoller, "Chiral quantum optics with v-level atoms and coherent quantum feedback," *Phys. Rev. A*, vol. 94, p. 033 829, 3 2016.

[100] Q Zou, K Merghem, S Azouigui, A Martinez, A Accard, N Chimot, F Lelarge, and A Ramdane, "Feedback-resistant p-type doped inas/inp quantum-dash distributed feedback lasers for isolator-free 10 gb/s transmission at 1.55 μm," *Applied Physics Letters*, vol. 97, no. 23, p. 231 115, 2010.

[101] A. Yariv and P. Yeh, *Photonics: optical electronics in modern communications*. Oxford University Press New York, 2007, vol. 6.

[102] S. Wieczorek, T. B. Simpson, B. Krauskopf, and D. Lenstra, "Bifurcation transitions in an optically injected diode laser: Theory and experiment," *Optics communications*, vol. 215, no. 1, pp. 125–134, 2003.

[103] B. Tromborg, J. Osmundsen, and H. Olesen, "Stability analysis for a semiconductor laser in an external cavity," *IEEE Journal of Quantum Electronics*, vol. 20, no. 9, pp. 1023–1032, 1984.

[104] J. S. Cohen, R. R. Drenten, and B. H. Verbeeck, "The effect of optical feedback on the relaxation oscillation in semiconductor lasers," *IEEE Journal of Quantum Electronics*, vol. 24, no. 10, pp. 1989–1995, 1988.

[105] N. Schunk and K. Petermann, "Numerical analysis of the feedback regimes for a single-mode semiconductor laser with external feedback," *IEEE Journal of Quantum Electronics*, vol. 24, no. 7, pp. 1242–1247, 1988.

[106] J. Helms and K. Petermann, "A simple analytic expression for the stable operation range of laser diodes with optical feedback," *IEEE Journal of Quantum Electronics*, vol. 26, no. 5, pp. 833–836, 1990.

[107] A. Ritter and H. Haug, "Theory of laser diodes with weak optical feedback. ii. limit-cycle behavior, quasi-periodicity, frequency locking, and route to chaos," *J. Opt. Soc. Am. B*, vol. 10, no. 1, pp. 145–154, 1993.

[108] G. H. M. van Tartwijk and D. Lenstra, "Nonlocal potential for class-b lasers with external optical feedback," *Phys. Rev. A*, vol. 50, R2837–R2840, 4 1994.

[109] A. E. Hramov, A. A. Koronovskii, O. I. Moskalenko, M. O. Zhuravlev, R. Jaimes-Reategui, and A. N. Pisarchik, "Separation of coexisting dynamical regimes in multistate intermittency based on wavelet spectrum energies in an erbium-doped fiber laser," *Phys. Rev. E*, vol. 93, p. 052 218, 5 2016.

[110] R. C. Williamson and R. D. Esman, "Rf photonics," *Journal of Lightwave Technology*, vol. 26, no. 9, pp. 1145–1153, 2008.

[111] J.-P. Zhuang and S.-C. Chan, "Phase noise characteristics of microwave signals generated by semiconductor laser dynamics," *Optics express*, vol. 23, no. 3, pp. 2777–2797, 2015.

[112] K. Volyanskiy, P. Salzenstein, H. Tavernier, M. Pogurmirskiy, Y. K. Chembo, and L. Larger, "Compact optoelectronic microwave oscillators using ultra-high q whispering gallery mode disk-resonators and phase modulation," *Optics Express*, vol. 18, no. 21, pp. 22 358–22 363, 2010.

[113] W. Ray, W.-S. Lam, P. N. Guzdar, and R. Roy, "Observation of chaotic itinerancy in the light and carrier dynamics of a semiconductor laser with optical feedback," *Phys. Rev. E*, vol. 73, p. 026 219, 2 2006.

[114] R. Hegger, H. Kantz, and T. Schreiber, "Practical implementation of nonlinear time series methods: The tisean package," *Chaos: An Interdisciplinary Journal of Nonlinear Science*, vol. 9, no. 2, pp. 413–435, 1999.

[115] H. Kantz, "A robust method to estimate the maximal lyapunov exponent of a time series," *Physics letters A*, vol. 185, no. 1, pp. 77–87, 1994.

[116] H. Kantz and T. Schreiber, *Nonlinear time series analysis*. Cambridge university press, 2004, vol. 7.

[117] J.-P. Zhuang and S.-C. Chan, "Phase noise characteristics of microwave signals generated by semiconductor laser dynamics," *Opt. Express*, vol. 23, no. 3, pp. 2777–2797, 2015.

[118] K. Volyanskiy, P. Salzenstein, H. Tavernier, M. Pogurmirskiy, Y. K. Chembo, and L. Larger, "Compact optoelectronic microwave oscillators using ultra-high q whispering gallery mode disk-resonators and phase modulation," *Opt. Express*, vol. 18, no. 21, pp. 22 358–22 363, 2010.

[119] W. Ray, W.-S. Lam, P. N. Guzdar, and R. Roy, "Observation of chaotic itinerancy in the light and carrier dynamics of a semiconductor laser with optical feedback," *Phys. Rev. E*, vol. 73, p. 026 219, 2 2006.

[120] G Acket, D. Lenstra, A Den Boef, and B Verbeek, "The influence of feedback intensity on longitudinal mode properties and optical noise in index-guided semiconductor lasers," *IEEE Journal of Quantum Electronics*, vol. 20, no. 10, pp. 1163–1169, 1984.

[121] K. Lüdge, E. Schöll, E. Viktorov, and T. Erneux, "Analytical approach to modulation properties of quantum dot lasers," *Journal of applied physics*, vol. 109, no. 10, p. 103 112, 2011.

[122] L. Jaurigue, A. Pimenov, D. Rachinskii, E. Schöll, K. Lüdge, and A. G. Vladimirov, "Timing jitter of passively-mode-locked semiconductor lasers subject to optical feedback: A semi-analytic approach," *Physical Review A*, vol. 92, no. 5, p. 053 807, 2015.

[123] A. V. Naumenko, N. A. Loiko, S. I. Turovets, P. S. Spencer, and K. A. Shore, "Controlling dynamics in external-cavity laser diodes with electronic impulsive delayed feedback," *J. Opt. Soc. Am. B*, vol. 15, no. 2, pp. 551–561, 1998.

[124] S. Behnia, S. Afrang, A. Akhshani, and K. Mabhouti, "A novel method for controlling chaos in external cavity semiconductor laser," *Optik*, vol. 124, no. 8, pp. 757 –764, 2013.

[125] N. L. Naumann, S. M. Hein, M. Kraft, A. Knorr, and A. Carmele, "Feedback control of photon-statistics," *Proc. SPIE*, vol. 10098, 100980N–100980N–7, 2017.

[126] S. Whalen, A. Grimsmo, and H. Carmichael, "Open quantum systems with delayed coherent feedback," *arXiv preprint arXiv:1702.05776*, 2017.

[127] J. Eschner, C. Raab, F Schmidt-Kaler, and R Blatt, "Light interference from single atoms and their mirror images," *Nature*, vol. 413, no. 6855, pp. 495–498, 2001.

[128] D. F. Walls and G. J. Milburn, *Quantum optics*. Springer Science & Business Media, 2007.

[129] M. A. Wilson, P. Bushev, J. Eschner, F. Schmidt-Kaler, C. Becher, R. Blatt, and U. Dorner, "Vacuum-field level shifts in a single trapped ion mediated by a single distant mirror," *Phys. Rev. Lett.*, vol. 91, p. 213 602, 21 2003.

[130] R. H. Dicke, "Coherence in spontaneous radiation processes," *Phys. Rev.*, vol. 93, pp. 99–110, 1 1954.

[131] J. Dalibard, Y. Castin, and K. Mølmer, "Wave-function approach to dissipative processes in quantum optics," *Physical review letters*, vol. 68, no. 5, p. 580, 1992.

[132] K. Lalumière, B. C. Sanders, A. F. van Loo, A. Fedorov, A. Wallraff, and A. Blais, "Input-output theory for waveguide qed with an ensemble of inhomogeneous atoms," *Phys. Rev. A*, vol. 88, p. 043 806, 4 2013.

[133] S. Turovets, J Dellunde, and K. Shore, "Selective excitation of periodic dynamics in external cavity laser diodes," *Electronics Letters*, vol. 32, no. 1, pp. 42–43, 1996.

[134] A. Naumenko, N. Loiko, S. Turovets, P. Spencer, and K. Shore, "Controlling dynamics in external-cavity laser diodes with electronic impulsive delayed feedback," *JOSA B*, vol. 15, no. 2, pp. 551–561, 1998.